MATERIALS CHARACTERIZATION AND ANALYSIS COLLECTION

Richard Brundle, *Collection Editor*

A Practical Guide to Transmission Electron Microscopy, Volume II

Advanced Microscopy

Zhiping Luo

MOMENTUM PRESS
ENGINEERING

A Practical Guide to Transmission Electron Microscopy, Volume II

A Practical Guide to Transmission Electron Microscopy, Volume II

Advanced Microscopy

Zhiping Luo

MOMENTUM PRESS
ENGINEERING

A Practical Guide to Transmission Electron Microscopy,
Volume II: Advanced Microscopy

First published in 2016 by
Momentum Press, LLC 222
East 46th Street, New York, NY 10017
www.momentumpress.net

ISBN-13: 978-1-60650-917-3 (paperback)
ISBN-13: 978-1-60650-918-0 (e-book)

Momentum Press Materials Characterization and Analysis Collection

DOI: 10.5643/9781606509180

Collection ISSN: 2377-4347 (print)
Collection ISSN: 2377-4355 (electronic)

Cover and interior design by S4Carlisle Publishing Services
Private Ltd., Chennai, India

First edition: 2016

10 9 8 7 6 5 4 3 2 1

Printed in the United States of America.

Dedicated to

My dear parents, who taught me the diligence—no matter what kind of job it is.

Abstract

Transmission electron microscope (TEM) is a very powerful tool for characterizing various types of materials. Using a light microscope, the imaging resolution is at several hundred nanometers, and for a scanning electron microscope, SEM, at several nanometers. The imaging resolution of the TEM, however, can routinely reach several angstroms on a modem instrument. In addition, the TEM can also provide material structural information, since the electrons penetrate through the thin specimens, and chemical compositional information due to the strong electron–specimen atom interactions. Nowadays, TEM is widely applied in diverse areas in both physical sciences (chemistry, engineering, geosciences, materials science, and physics) and life sciences (agriculture, biology, and medicine), playing a key role in research or development for material design, synthesis, processing, or performance.

This book provides a concise practical guide to the TEM user, starting from the beginner level, including upper-division undergraduates, graduates, researchers, and engineers, on how to learn TEM efficiently in a short period of time. It is written primarily for materials science and engineering or related disciplines, while some applications in life sciences are also included. It covers most of the areas using TEM, including the instrumentation, sample preparation, diffraction, imaging, analytical microscopy, and some newly developed advanced microscopy techniques. In each topic, a theoretical background is firstly briefly outlined, followed with step-by-step instructions in experimental operation or computation. Some technical tips are given in order to obtain the best results. The practical procedures to acquire, analyze, and interpret the TEM data are therefore provided. This book may serve as a textbook for a TEM course or workshop, or a reference book for the TEM user to improve their TEM skills.

Keywords

Analytical Electron Microscopy; Ceramics; Chemical Analysis; Chemistry; Composites; Crystallography; Electron Diffraction; Electron Energy-Loss Spectroscopy (EELS); Forensic Science; Geosciences; Imaging; Industry; Life Sciences; Materials Science and Engineering; Metals and

Alloys; Microstructure; Nanomaterials; Nanoscience; Nanotechnology; Physics; Scanning Transmission Electron Microscopy (STEM); Polymer; Structure; Transmission Electron Microscopy (TEM); X-ray Energy-Dispersive Spectroscopy (EDS).

Contents

Preface

To study material structure, we need to use microscopes. With the naked eyes, we can barely see objects beyond 0.1 mm, while by using a light microscope composed of optical lenses, the resolution is improved beyond 1 μm to several hundred nanometers. However, to further improve the resolution, electron microscopy should be applied. Scanning electron microscopy (SEM) extends the resolution to several nanometers, and it can also provide elemental analyses, but it is hard to see objects below the several nanometer range. The transmission electron microscopy (TEM) has great advantages over other microscopy techniques, in that its ultrahigh imaging resolution can routinely reach several angstroms on a modern microscope, and it also has ability to study the structure using electron diffraction, and auxiliary capabilities to identify chemical compositions. Nowadays, TEM is a standard characterization approach in scientific research, academic education, industrial development, and governmental forensic investigations.

For over a decade at Texas A&M University, I held a TEM instrumental scientist position, where I taught TEM courses and trained many TEM users. During the user training, I realized that step-by-step instructions were always very helpful so that the user could work in the right way immediately, instead of learning from many trials. The users should learn the instructions first and then practice on the instrument to improve the working efficiency, rather than practice with minimum instructions.

This book provides a practical guide to the TEM user as a quick reference on how to utilize the various TEM techniques more efficiently to get meaningful results. It starts at the beginner level and introduces the TEM skills concisely, including practical instructions on how to operate the instrument correctly, how to avoid possible problems, how to understand the results, and how to interpret and compute the data. It is separated into two volumes with different levels. Volume 1 is on Fundamentals of TEM, including TEM sample preparation, instrumentation and operation procedures, electron diffraction I (selected-area electron diffraction), and imaging I (mass-thickness imaging and diffraction contrast

imaging). Volume 2 covers Advanced Microscopy, including electron diffraction II (Kikuchi diffraction, convergent-beam electron diffraction, and nano-beam electron diffraction), imaging II (scanning transmission electron microscopy, and high-resolution electron microscopy), analytical electron microscopy for elemental analyses, and some new developments and specific applications.

I hope you enjoy the power of the TEM. May TEM assist your research, provide you with good results, and bring you good luck in your career!

Zhiping Luo
Fayetteville, North Carolina
June 2015

Acknowledgments

First of all, I acknowledge my many collaborators who provided me with wonderful samples for the TEM investigations and made fruitful discussions on what we learned from the TEM. It is really hard to list all of their names on this page, while the following major contributors are apparently among them, alphabetically, Drs. M. Akbulut, S. Bashir, J. Batteas, L. Carson, C.C. Chen, W. Chen, D. Fang, J. Fang, B. Guo, Z. Guo, K.T. Hartwig, A. Holzenburg, X. Hong, X. Jiang, H.E. Karaca, I. Karaman, B. Kockar, J.H. Koo, A. Kronenberg, S. Kundu, D. Lagoudas, G. Liang, Y. Li, J. Liu, J. Ma, A.-J. Miao, D.J. Miller, J.F. Mitchell, O. Ochoa, A. Oki, V. Paredes-García, Z. Quan, P.H. Santschi, R.E. Schaak, L. Shao, D.H. Son, C. Song, Y. Song, L. Sun, X.S. Sun, Y. Tang, Y. Vasquez, H. Wang, W. Wu, J. Zhang, S. Zhang, X. Zhang, Q. Zhai, D. Zhao, H. Zheng, H.-C. Zhou, D. Zhu, J. Zhu, and M. Zhu.

I also thank my previous colleagues (Dr. A. Holzenburg, Mr. R. Littleton, Ms. A. Ellis, Dr. C. Savva, Dr. J. Sun, Dr. S. Vitha, Dr. H. Kim, etc.) at the Microscopy and Imaging Center, Texas A&M University for technical assistance and stimulating discussions on biological samples; Dr. D.J. Miller at the Electron Microscopy Center, Argonne National Laboratory, for advanced TEM skills; and Profs. H. Hashimoto and E. Sukedai at Okayama University of Science, Japan, for HREM.

Grateful appreciations should also be given to those professors who introduced me to the field of electron microscopy in my early career in China, alphabetically, Drs. K.H. Kuo, F.H. Li, and S. Zhang.

Finally, I am grateful to the book Collection Editor Dr. C. Richard Brundle for technical assistance to edit this book, and to those publishers for their permissions to reuse the materials presented in this book as specifically referenced.

About the Book

- This book is a concise practical guide for the TEM users to improve TEM skills in a short period of time.
- It is also a textbook for a short course (semester-long TEM undergraduate or graduate course, or intensive short-term workshop).
- It provides step-by-step instructions how to operate the instrument, how to analyze, and how to compute the data.
- It covers areas primarily for physical sciences (chemistry, engineering, geosciences, materials science, and physics) and some examples in life sciences (agriculture, biology, and medicine).
- It applies to scientific research, academic education, industrial developments, governmental forensic investigations, and others.

Personnel Experiences with TEM

1. Be aware of what you are doing with the microscope!
   - Read sufficient literature to make clear what is new and what has been done previously.
2. See both, the forest and the trees!
   - Information in both high and low magnifications should be known.
3. Good results are obtained out of the microscope room!
   - Post-experiment analyses (data processing, computation, and quantification) and documentation are very important.
4. A good habit is beneficial to your whole career!
   - Organize your samples and data well.

CHAPTER 6

Electron Diffraction II

In a transmission electron microscope (TEM), accelerated electrons can penetrate thin specimens. It is known that the electrons possess a wave nature with a short wavelength, for example, at 200 kV wavelength λ = 0.00251 nm. Because of the interactions of the electron waves with the crystal lattices, electrons are scattered at different angles, forming electron diffraction. The electron diffraction not only provides the specimen structural information, but also assists the imaging. In Chapter 4 about Electron Diffraction I in Volume 1, selected-area electron diffraction (SAED) has been introduced. This chapter on Electron Diffraction II covers more advanced diffraction techniques.

6.1 Kikuchi Diffraction

6.1.1 Formation of Kikuchi Lines

Kikuchi lines appear in the electron diffraction patterns if the sample has high crystallinity, such as Si, ceramics, or undeformed metal, and in thicker areas. Under parallel beam illumination, Kikuchi lines are generated in suitably thick samples by inelastically scattered electrons (halo background) that are subsequently elastically scattered. Elastic scattering by itself produces the Bragg diffraction maxima (spots). If the sample is too thin or with high density of structural defects, Kikuchi lines may not be visible. This diffraction phenomenon was discovered and explained by Dr. Seishi Kikuchi [1].

Two examples of SAED patterns from a ceramic B_4C phase with Kikuchi patterns are shown in Fig. 6.1. The Kikuchi lines appear as pairs, one is bright line, which is farther away from the center beam, and the other is dark line, which is closer to the center beam.

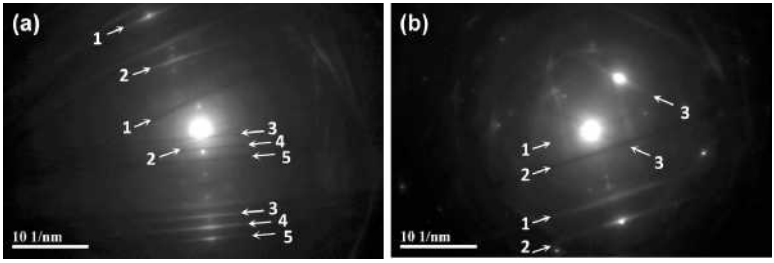

Fig. 6.1 (a, b) Two examples of Kikuchi lines, which appear as pairs, as indicated by numbers.

The formation of Kikuchi diffraction is illustrated in Fig. 6.2. In a thin crystal, as shown in Fig. 6.2(a), the incident electrons are parallel to the optical axis so that they are diffracted only by the (*hkl*) planes, and their diffracted rays with the same angle θ are parallel to form Bragg diffraction maxima (by the objective lens) that appear on the TEM screen. However, if the sample is thick, inelastic scattering happens, which causes the electrons scatter to different angles, although primarily forward, as shown in Fig. 6.2(b). Now the incident electrons are no longer parallel to the optical axis. Considering the 3D space, the diffracted rays would form a cone filled with excess electrons on its surface (nothing inside the cone), and each ray on the cone is still formed by Bragg diffraction at an angle of θ with respect to the (*hkl*) plane. Since more electrons are diffracted on this cone, on the opposite side of the (*hkl*) plane, a cone is formed with deficient electrons on the cone surface. These cones are called as Kossel cones. When they intersect with the Ewald sphere, a pair of curved lines are formed. One is a bright line (with access electrons) across the Bragg spot **g**, and another one is a dark line (with deficient electrons) across the center beam O. Since the radius of the Ewald sphere is very large, the curve lines appear as approximately straight lines on the screen with short lengths.

If the sample slightly tilts, as shown in Fig. 6.2(c), the incident electrons still impregnate the sample in the same way, no matter it is tilted or not. As will be demonstrated in the next section, the Bragg diffraction maxima still remain at the same position for a small sample tilt, at the angle of 2θ with respect to the incident beam. However, the Kossel cones are formed by the (*hkl*) of the sample crystal, and thus the Kossel cones tilt simultaneously with the crystal tilt (in a similar manner with light

reflection that the reflected light tilts simultaneously with the mirror tilt). An enlarged illustration is shown in Fig. 6.2(d). Therefore on the TEM screen, the diffraction spots remain at the same positions, but the Kikuchi lines move for a small crystal tilt. These pairs move simultaneously while keeping the same spacing. Therefore, the Kikuchi lines are very useful to determine the crystallographic orientations.

Shown in Fig. 6.3 are simulated Kikuchi patterns along [001], [011], and [111] zone axes. It is seen that Kikuchi bands link with major poles. Fig. 6.3(a–c) are computed for indices up to 2, whereas Fig. 6.3(d) for indices up to 4 to display many Kikuchi lines. Such Kikuchi bands are very useful to the TEM operator to tilt the crystal from one zone axis to another one along such bands. For a cubic crystal, the operator should be able to tilt [001]–[011]–[111] zone axes using a double-tilt specimen holder, forming a triangle on the Kikuchi pattern.

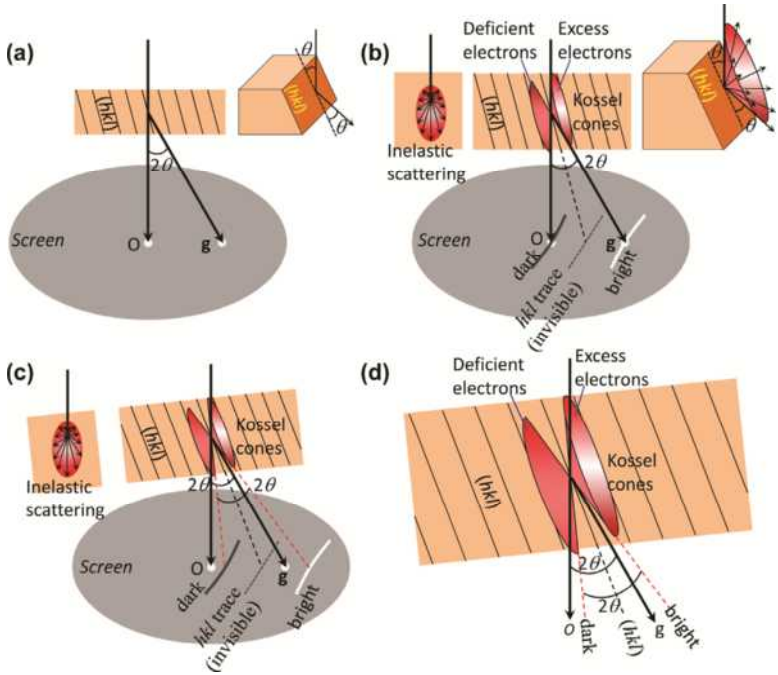

Fig. 6.2 Formation of Kikuchi lines. (a) Bragg diffraction only in a thin crystal; (b) Kikuchi lines by a thicker crystal; (c) the sample is slightly tilted; (d) enlargement from (c) showing the geometrical details.

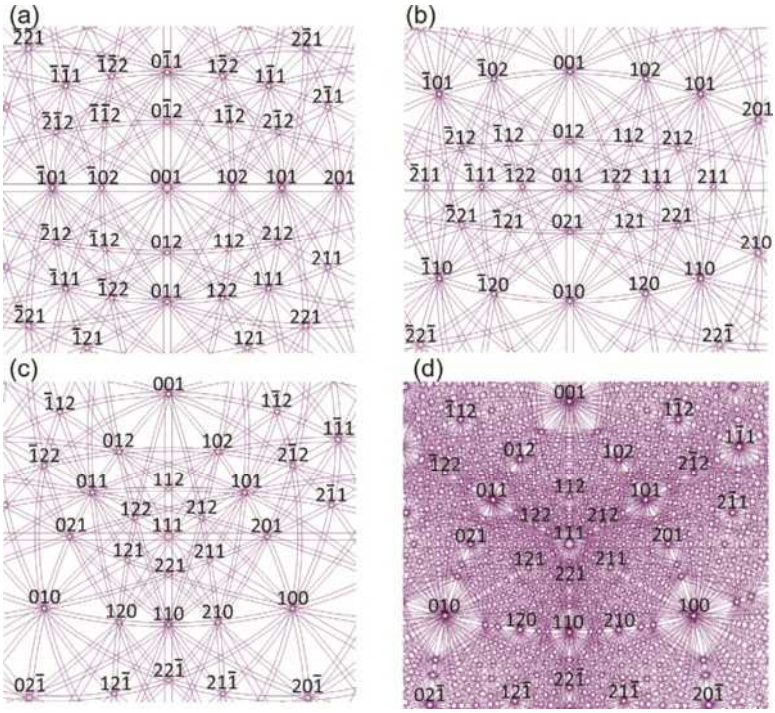

Fig. 6.3 Simulated Kikuchi patterns along [001] (a), [011] (b), and [111] (c, d) orientations. (a–c) are computed up to index of 2, while (d) is up to index of 4.

6.1.2 *Kikuchi Diffraction and Crystal Tilt*

The SAED pattern is not sensitive to a small crystal tilt, while the Kikuchi diffraction pattern is sensitive to it. In Fig. 6.4(a), the sample is at the Bragg diffraction condition, so that the Kikuchi lines are across the diffraction **g** and the center beam O. If θ_1 is the angle of incident ray with the (*hkl*) plane and θ_2 is the angle of the diffracted ray with the (*hkl*) plane, $\theta_1 = \theta_2 = \theta$, and the difference of travel distance of two adjacent rays is $2d\sin\theta$,

$$2d\sin\theta = n\lambda \tag{6.1}$$

where d is the lattice spacing of the (*hkl*) planes, λ is the wavelength, and n is an integer number (1, 2, 3, …). If the sample is slightly tilted, as shown in Fig. 6.4(b), $\theta_1 > \theta_2$. Compared with Eq. 4.1 (Chapter 4 in

Volume 1), the difference of travel distance between two adjacent rays is $d\sin\theta_1 + d\sin\theta_2$, and thus

$$d\sin\theta_1 + d\sin\theta_2 = n\lambda \tag{6.2}$$

Since the angles are very small, $\sin\theta = \theta$ and thus according to Eqs. 6.1 and 6.2, we have $\theta_1 + \theta_2 = 2\theta$, that is, the diffracted beam is at the same angle with respect to the incident beam, as shown in Fig. 6.4(a), although the sample is slightly tilted. As demonstrated in Fig. 6.2, the Kikuchi lines move outward, and we define the deviation parameter $s > 0$ for this case. Here, the deviation parameter s is used to measure the deviation from the Bragg diffraction (s is defined by Eq. 5.5 in Volume 1). If the reciprocal point is on the Ewald sphere, then $s = 0$; if the reciprocal point moves above the Ewald sphere by sample tilt, then $s > 0$; otherwise, $s < 0$.

If the sample is tilted to an opposite way, $\theta_1 < \theta_2$, as shown in Fig. 6.4(c), again we still have $\theta_1 + \theta_2 = 2\theta$. Hence, the diffracted ray is along the same direction, but the Kikuchi lines move inward. Here, $s < 0$.

If the sample is tilted to an exact zone axis, that is, the diffraction intensities are symmetrical to the center beam, the Kikuchi lines are located at the center between (000) and $\pm\mathbf{g}$, as shown in Fig. 6.4(d). Now these two lines have the same intensity (rather than bright and dark), but they form a bright Kikuchi band across the center beam (outside the band, the background is therefore darker). In this case, only (000) is on the Ewald sphere, while others are slightly below the sphere since the sphere is curved upward, and thus $s < 0$.

The sample tilt can also be understood using the reciprocal space. As shown in Fig. 6.5(a), the sample is aligned along its $[U_1V_1W_1]$ zone axis, with symmetrical intensities to its center $\mathbf{g}_0$ spot. Only (000) is on the Ewald sphere, while all others are below it since the sphere is curved upward, and thus $s < 0$. When the crystal is slight tilted, as shown in Fig. 6.5(b), the intersections of any reflection $\mathbf{g}$ with its counterpart $-\mathbf{g}$ are no longer symmetrical, so different intensities are resulted. Although the $[U_1V_1W_1]$ zone axis is slightly off the optical axis, the spot geometry still remains the same, only intensities vary. If only (000) and $(h_1k_1l_1)$ are aligned on the Ewald sphere, only these two beams are strong and others are weak (Fig. 6.5c). This is the two-beam condition, which is very useful for diffraction-contrast imaging, as discussed in Chapter 5 in Volume 1. Here, $s = 0$ for $\mathbf{g}_1$. However, if the sample is grossly tilted to reach

another intersection with the Ewald sphere to form a different geometry, a different zone axis $[U_2V_2W_2]$ pattern is obtained, as shown in Fig. 6.5(d).

Note that in the reciprocal space, the lattice spots are elongated along the vertical direction, because of the shape effect, as the sample is very thin.

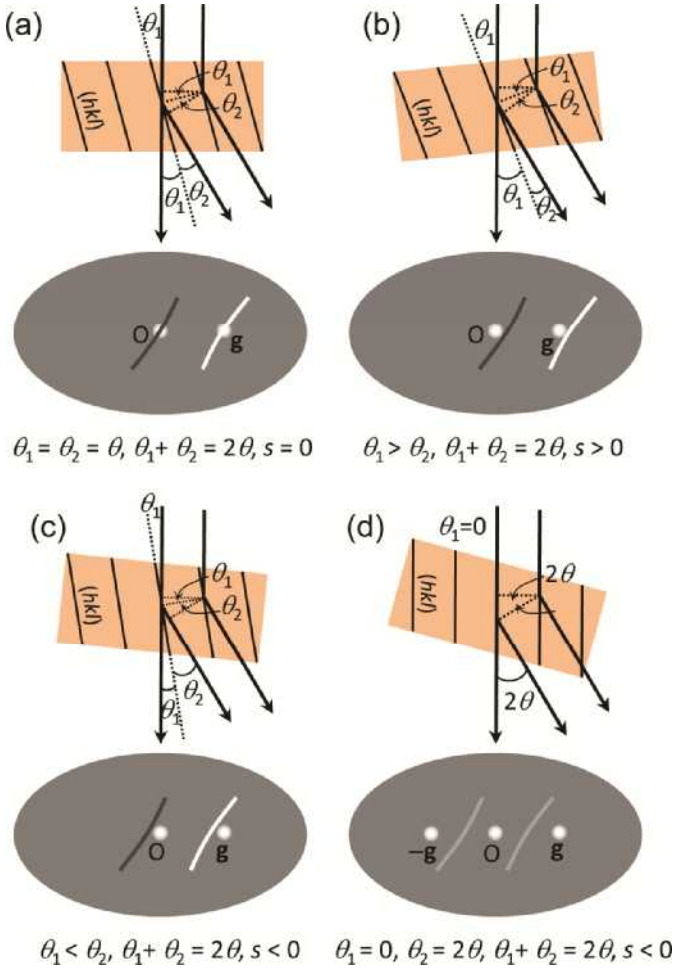

***Fig. 6.4** Kikuchi diffraction during sample tilt. (a) Exact Bragg diffraction condition; (b) sample is slightly tilted from (a); (c) sample is slightly tilted in an opposite way from (a); (d) sample is aligned along exact zone axis condition (symmetrical g and –g).*

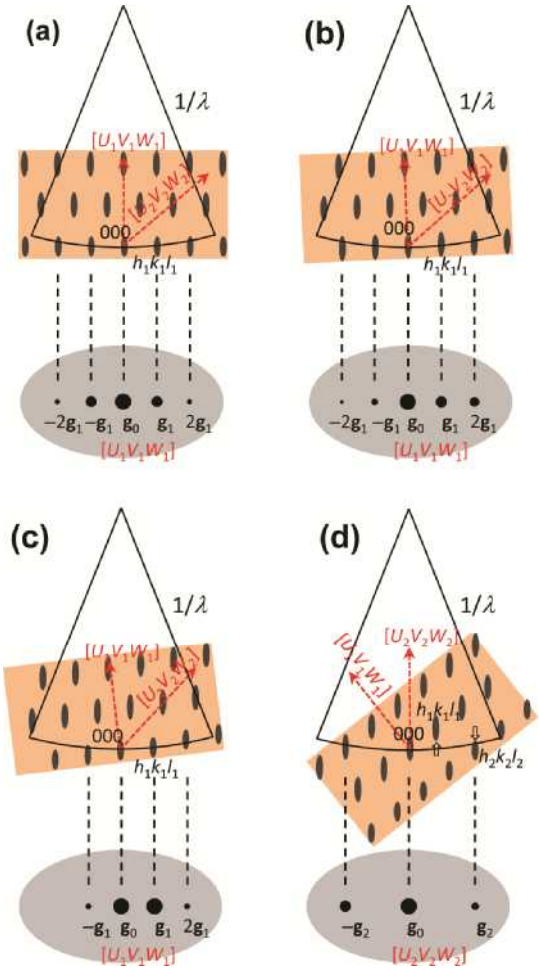

***Fig. 6.5** Bragg diffraction during sample tilt. (a) [$U_1V_1W_1$] zone axis; (b) slightly tilted from (a); (c) two-beam condition; (d) another zone axis [$U_2V_2W_2$] after large tilting.*

6.2 Convergent-Beam Electron Diffraction

6.2.1 *Formation of Convergent-Beam Diffraction*

The SAED is formed by using parallel illumination, as shown in Fig. 6.6(a), and these transmitted and diffracted rays are then refracted by the objective lens to form spots. If the incident electrons are nonparallel but at an angle, as shown in Fig. 6.6(b), the transmitted and diffracted beams do not merge

as spots but as disks [2–4]. This diffraction mode is convergent-beam electron diffraction (CBED) or convergent-beam diffraction (CBD).

CBED should be done in CBED mode, or Nano Probe mode on some TEMs. A comparison of electron optics of conventional TEM, X-ray energy-dispersive spectroscopy (EDS), nano-beam electron diffraction (NBED) or nano-beam diffraction (NBD), and CBED is shown in Fig. 6.7 [5]. In the TEM mode, a condenser mini-lens is activated so that parallel illumination is provided on the sample, and the illuminated area is large. However, in the EDS mode, this mini-lens is deactivated so that the electrons impregnate the sample at a point with a large angle (the semiangle is denoted as α_1 in the figure). In the NBED mode, the mini-lens is activated to deflect the beam to a small angle, so that the electrons impregnate the sample at a point but with smaller angle compared with EDS (the semiangle is denoted as α_2 in the figure). In the CBED mode, the α angle varies largely, which covers both EDS (α_1) and NBED (α_2) ranges, $\alpha_2 \le \alpha \le \alpha_1$.

The α angle is controlled by α-selector knob on the TEM panel. On the JEOL 2010 TEM, the available selections are listed in Table 6.1. These numbers are the only possible selections on the instrument. Numbers in the same column indicate that their settings are the same. For example, NBED #1–5 and corresponding CBED #1–5 have the same settings, and EDS #1, NBED #5, and CBED #5 have the same settings. It is seen that the EDS mode covers large α angles, NBED covers smaller α angles, and CBED covers entire ranges of EDS and NBED.

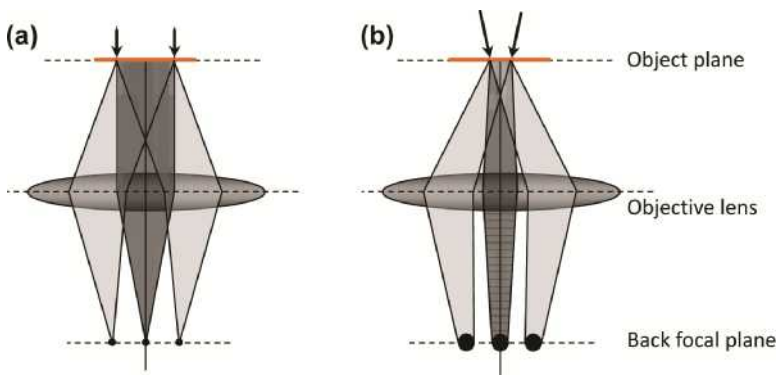

***Fig. 6.6** Comparison of SAED and CBED modes. (a) SAED; (b) CBED.*

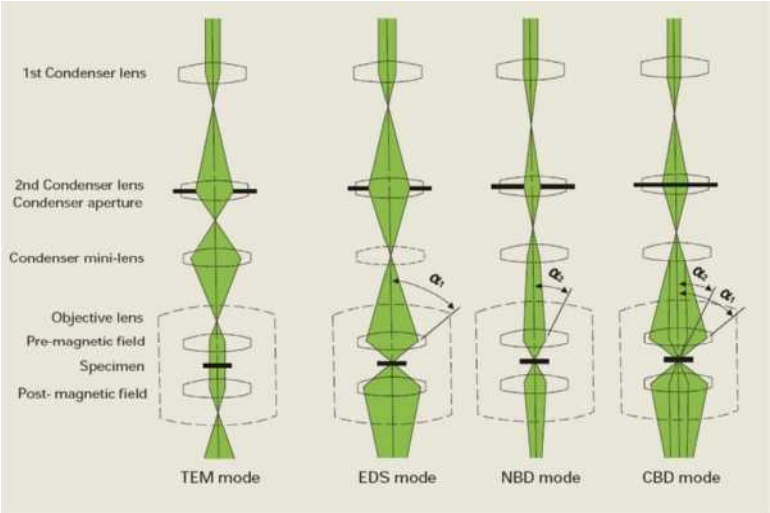

Fig. 6.7 Electron optics of TEM, EDS, NBED and CBED modes (courtesy of JEOL [5]).

Table 6.1 Selection of α angles in EDS, NBED, and CBED modes.

EDS					1	2	3	4	5
NBED	1	2	3	4	5				
CBED	1	2	3	4	5	6	7	8	9

On some TEMs, all EDS, NBED, and CBED are done in a Nano Probe mode.

6.2.2 *High-Order Laue Zone*

An SAED pattern is formed by the intersection of Ewald sphere with the reciprocal lattice. If the crystal structure has a long repeating distance at Z direction, in the reciprocal space, the layer spacing is shorter. Hence, the upper level (higher-order) reciprocal lattice may intersect with the Ewald sphere, forming a high-order Laue zone (HOLZ) pattern. Such HOLZ reflections normally appear only at high angles far away from the center beam.

However, in the CBED mode, it is easy to get HOLZ diffraction. As shown in Fig. 6.8, since the incident beam is inclined, the optical axis rotates in a shape of a cone with semiangle of α. Therefore, the Ewald sphere also rotates, and the ones at the most end side would have more

chances to intersect with the high-order spots. The layer with the original (000) spot is zero-order Laue zone (ZOLZ), and on the upper levels, first-order Laue zone (FOLZ), second-order Laue zone (SOLZ), and so on. Considering the 3D space, the HOLZ spots form rings far away from the center, as shown in Fig. 6.8(b).

For HOLZ diffraction (*hkl*) along [*UVW*] zone axis, compared with Eq. 4.15 (Chapter 4 in Volume 1), we have

$$hU + kV + lW = n \tag{6.3}$$

Here n is the order of the HOLZ diffraction.

More details about the HOLZ diffraction is illustrated in Fig. 6.9. For a primitive cubic (PC) structure, its reciprocal is still PC, as shown in Fig. 6.9(a), and thus its HOLZ diffraction spots have the same geometry as ZOLZ. The zero-order and all high-order diffraction spots coincide in the pattern. However for a face-centered cubic (FCC) structure, its reciprocal space is body-centered cubic (BCC), as shown in Fig. 6.9(d). The zero- and second-order diffraction patterns have the same geometry, while first- and third-order pattern spots are translated to the square centers of the ZOLZ pattern. Similarly, a BCC structure possesses an FCC reciprocal lattice (Fig. 6.9h). Its zero- and second-order diffraction patterns have the same geometry, while FOLZ pattern is translated as shown in Fig. 6.9(j). Using the reciprocal space, it is possible to index the ZOLZ (regular SAED pattern) and HOLZ spots on a diffraction pattern.

In SAED mode, the Kikuchi lines are formed by inelastic scattering in thicker samples. The inelastic scattering changes the ray directions, causing the Kikuchi diffraction. However, in the CBED mode, the incident beams are already nonparallel and at angles, the elastic scattering also contributes to the Kikuchi diffraction [6]. Note that the diffraction is from a small volume, so high crystallinity may be obtained; hence, in CBED mode, it is much easy to obtain Kikuchi lines.

When the Kikuchi diffraction happens in the CBED pattern, Kikuchi lines still appear as pairs. In the center (000) disk, they appear as dark (deficient intensity), while in HOLZ disks, they appear as bright (excess intensity) lines, that is, HOLZ lines. Many of such HOLZ lines on the HOLZ disks form rings, as shown in Fig. 6.10(a).

Since HOLZ lines contain 3D information, they can be used to determine a crystal symmetry of point groups and space groups. They can also be used to determine the unit cell height H.

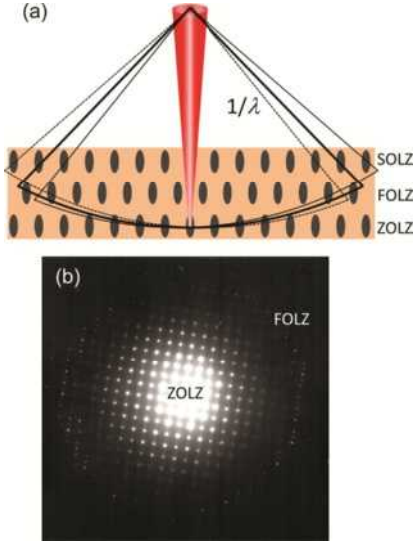

***Fig. 6.8** (a) Formation of HOLZ in CBED; (b) Example of HOLZ diffraction spots.*

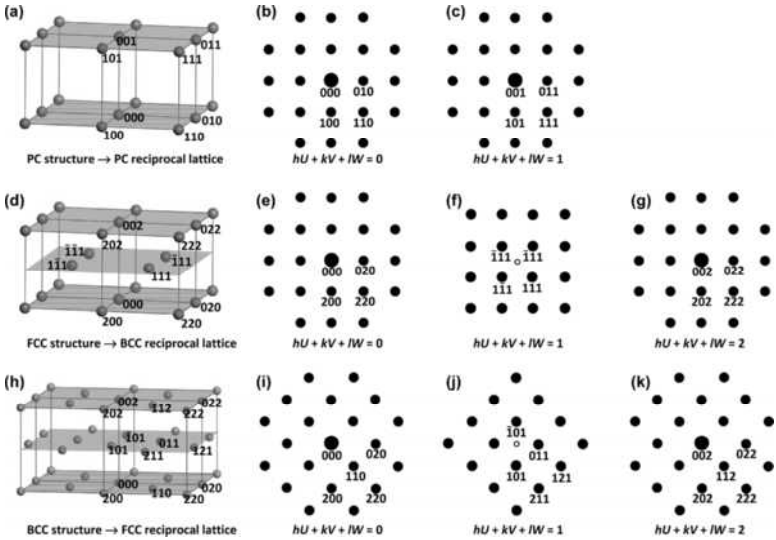

***Fig. 6.9** HOLZ diffraction. (a–c) PC crystal along [001]; (d–g) FCC crystal along [001]; (h–k) BCC crystal along [001].*

Suppose the radius of the FOLZ ring is r, which corresponds to the vector G in the reciprocal space (with a spacing of d) in Fig. 6.10(b). In the right triangle OAB, $AB^2 = OA^2 - OB^2$, and $OB = OC - H$; thus,

$$G^2 = (\frac{1}{\lambda})^2 - (\frac{1}{\lambda} - H)^2$$

Here, $AB = OC = 1/\lambda$. If H^2 is ignored,

$$\frac{1}{H} = \frac{2}{\lambda G^2} = \left(\frac{2}{\lambda}\right) d^2 \tag{6.4}$$

Here, $G = 1/d$. Therefore, from the radius r and camera length $L\lambda$, the spacing $d = L\lambda/r$ is obtained (it can also be measured directly using CCD camera software), and thus the unit cell height H can be determined from Eq. 6.4, although it is from a single CBED pattern. If it is done by the SAED method, it is required to get at least one other zone axis pattern containing the information of H, either by tilting or by selecting a different area.

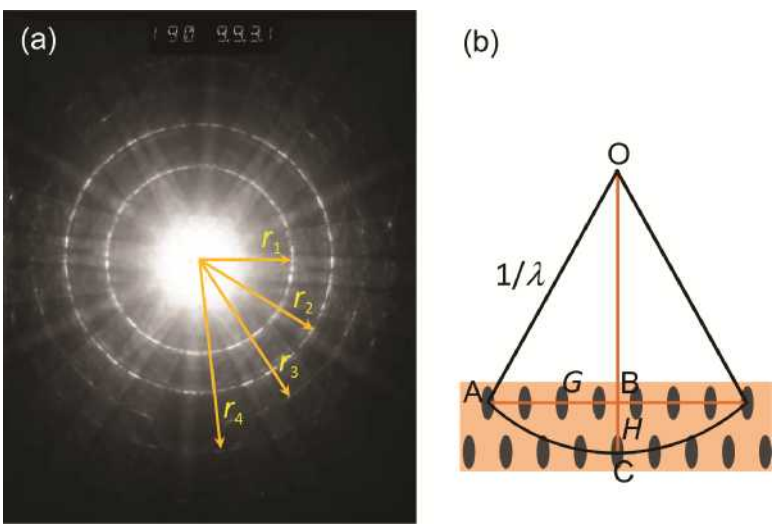

Fig. 6.10 (a) CBED pattern showing HOLZ rings; (b) geometric relationship.

6.2.3 *Experimental Procedures*

CBED is normally done in the following ways:

1. In the BF image mode, select a large (largest or the second largest) condenser aperture for CBED.
2. Select an area for CBED, and focus the image.
3. Switch to SAED mode and focus the spots and correct any astigmatism as needed (this step can be skipped, if the diffraction mode is already well aligned).
4. Switch to CBED or Nano Probe beam (the beam may become darker now), move the interested area to the center of screen, focus the beam to a point (crossover) on the sample using Brightness knob, and then press Diffraction button to switch to the diffraction mode. A CBED pattern is obtained.
5. Select different camera length L to see details in the (000) disk (bright-field symmetry) using a longer L, or whole-pattern symmetry using a shorter L.

Fig. 6.11(a) shows an SAED pattern of Mg–Zn–Y quasi-crystal (QC) [7] along a fivefold axis, displaying a 10-fold symmetry. From such a single SAED pattern, it is impossible to tell whether it is from icosahedral QC with fivefold symmetry [8], or a decagonal QC with 10-fold symmetry [9]. The CBED patterns using a larger or a smaller condenser aperture are shown in Fig. 6.11(b) and (c), respectively. In Fig. 6.11(b), multiple Kikuchi lines weave a symmetrical pentagon pattern; in Fig. 6.11(c) using a smaller condenser aperture, the FOLZ spots also exhibit a fivefold symmetry. Therefore, the QC belongs to the icosahedral type.

Fig. 6.12(a) is a CBED pattern from a crystalline FCC phase along [111], recorded with a shorter L to show the whole-pattern $3m$ symmetry from the FOLZ ring. If the mirror symmetry is not very clear in the whole pattern, one may tilt the sample off the zone axis to check, as shown in Fig. 6.12(b) which displays the m symmetry clearly.

In order to get a high-quality CBED whole pattern, the sample should be tilted to its exact zone axis. However, by a double-tilt holder it may not be easy to do so. As mentioned in Section 4.4 in Volume 1, one may use beam tilt to easily align the pattern slightly to get a well-aligned symmetrical pattern.

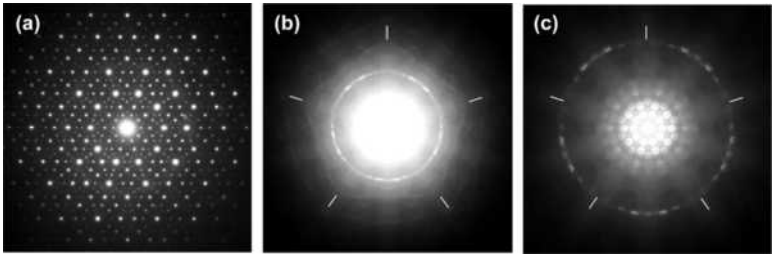

Fig. 6.11 Electron diffraction from icosahedral quasicrystals. (a) SAED from 5-fold direction; (b) CBED with a larger condenser aperture; (c) CBED with a smaller condenser aperture.

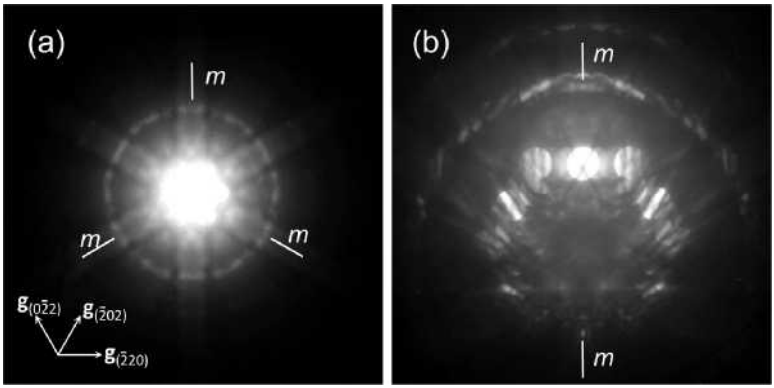

Fig. 6.12 (a) CBED whole pattern along [111] zone axis; (b) CBED pattern after tilting from (a) to show the mirror symmetry as indicated.

The CBED can be done as often as SAED. In fact, experienced TEM users often use it to replace SAED, since it does not need the diffraction aperture. However, in the CBED mode, since the entire beam is focused on one point, sample may be damaged if it is sensitive to the electron beam. Therefore, only stable samples are suitable for CBED.

6.3 Nano-Beam Electron Diffraction

6.3.1 Formation of Nano-beam Electron Diffraction

NBED can produce electron diffraction from nanoscale areas. With the dramatic development of nanoscience and nanotechnology, this diffraction technique has been especially useful in the characterization of nanomaterials.

The electron optics is shown in Fig. 6.7. A small condenser aperture, normally the smallest or the second smallest, should be chosen so that the incident electrons are restricted to a small angle range on the specimen.

Examples of Au_3Fe, Au_3Ni and Au_3Co nanoparticles (NPs) are shown in Fig. 6.13 [10]. The Au_3Fe and Au_3Ni nanocrystals are in spherical shape with an average particle size of around 20 nm, and the Au_3Co nanocrystals are slightly larger with more irregular shapes. The HRTEM images reveal lattice fringes of 0.23 nm, which is the {111} plane spacing of the FCC structure. However, the SAED patterns, even obtained using the smallest diffraction aperture, only exhibit polycrystalline ring patterns. Although $L1_2$ ordering reflections can be identified from the polycrystalline SAED patterns (bottom row of Fig. 6.13), it is unclear whether they are fully ordered, or only part of these NPs are ordered. Therefore, NBED experiment is needed to identify the structure of these single NPs.

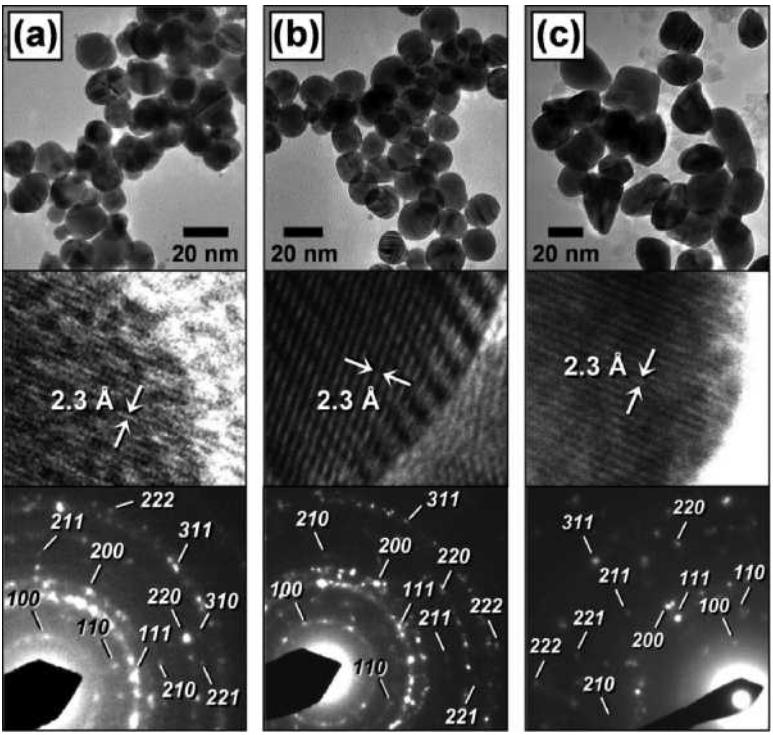

Fig. 6.13 TEM images (top), high-resolution TEM images (middle), and SAED patterns (bottom) for $L1_2$-type (a) Au_3Fe, (b) Au_3Ni, and (c) Au_3Co nanocrystals.

The NBED patterns from the Au_3Ni NPs are shown in Fig. 6.14. By selecting single NPs for diffraction, clear NBED patterns from three major zone axes are obtained, all with $L1_2$ ordering (Fig. 6.14b–d). Note that these patterns are taken from different NPs, since it is rather difficult to tilt such small objects from one zone axis to another one. All NPs examined by NBED showed such $L1_2$ ordering.

If the particle is larger, such as the particle with 100 nm in Fig. 6.15(a), regular SAED may be used to get a diffraction pattern (Fig. 6.15b).

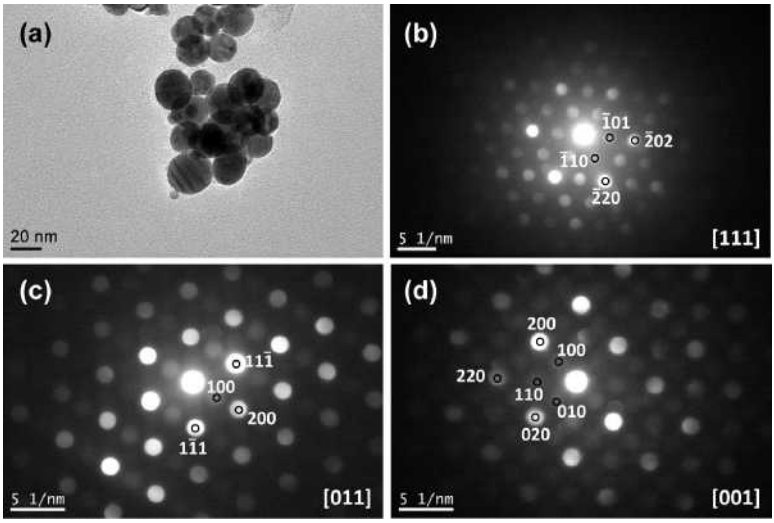

***Fig. 6.14** (a) Au_3Ni NPs with $L1_2$-type ordered structure; (b) NBED along [111]; (c) NBED along [011]; (d) NBED along [001].*

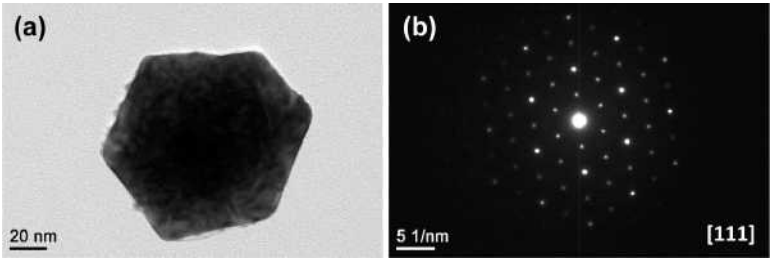

***Fig. 6.15** (a) A larger NP; (b) SAED pattern from the NP.*

6.3.2 *Experimental Procedures*

NBED is conducted in the following procedures:

1. In the BF mode, move an interested area to the screen center and focus the image.
2. Conduct SAED and focus the diffraction pattern and correct any astigmatism (this step may be skipped if the diffraction mode is already well aligned).
3. Select the smallest or second smallest condenser aperture, and switch to NBED or Nano Probe mode (now the beam becomes very dark).
4. Focus the beam to a crossover point on the sample using Brightness knob and ensure the interested area is still in the center and the beam is focused on it (at a crossover), then press Diffraction button to switch to the diffraction mode. An NBED pattern is therefore obtained.

Although the operations of NBED and CBED are similar by focusing the beam to get a crossover on the sample without using the diffraction aperture, it is more difficult to work with NBED, just because the beam becomes very dark, and the image is visible only when the beam almost forms a crossover.

To get information similar to SAED pattern, the smallest condenser aperture is preferred. Fig. 6.16(a) is a NBED pattern formed by the second smallest condenser aperture. Although it is along [011] zone axis of the $L1_2$ ordered structure, the weak ordering spots are invisible since they are buried by overlapped large fundamental spots (disks). However, as shown previously in Fig. 6.14(c), the [011] NBED pattern taken by the smallest condenser aperture could clearly exhibit the $L1_2$ ordering. Therefore, normally the smallest condenser aperture should be used for NBED.

In the NBED mode, in most case it is very difficult to tilt the sample, since the electron beam is so weak and the interested area is so small. To get better quality patterns, beam tilt should be used which is more efficient than the sample mechanical rotating. Fig. 6.16(b) is from

a single NP near [111] but it is slightly off this zone axis. Using beam tilt, a better pattern is obtained, as shown in Fig. 6.16(c). Further beam tilting yields Fig. 6.16(d). Although it is still slightly off, it already revealed the $L1_2$ ordering that is much better than the original pattern in Fig. 6.16(b). The user should search for more areas until a satisfactory pattern at or near a major zone axis is obtained, then take NBED patterns.

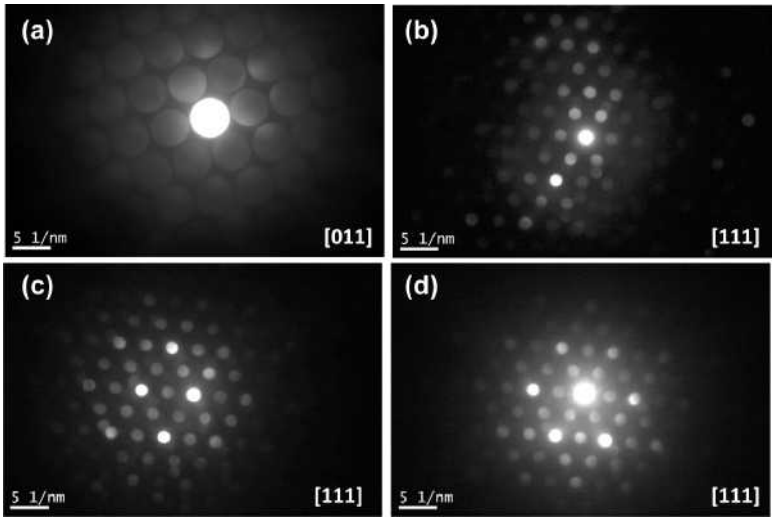

Fig. 6.16 (a) NBED along [011] Au_3Ni using the second smallest condenser aperture; (b–d) NBED patterns using the smallest condenser aperture, taken from a same Au_3Ni NP along [111] but aligned using beam tilts.

References

[1] S. Kikuchi. Diffraction of cathode rays by mica. *Jpn. J. Phys.* **5**, 83–96 (1928).

[2] J.W. Steeds. Convergent beam electron diffraction. In: Introduction to Analytical Electron Microscopy, edited by John J. Hren, Joseph I. Goldstein, David C. Joy. Plenum Press, New York, pp. 387–422 (1979).

[3] J.C.H. Spence, J.M. Zuo. Electron Microdiffraction. Plenum Press, New York, 1992.

[4] M. De Graef. Introduction to Conventional Transmission Electron Microscopy. Cambridge University Press, Cambridge, UK, 2003.

[5] JEOL. JEM–2100F Field Emission Electron Microscope. JEOL Ltd., Akishima, Tokyo.

[6] D.B. Williams, C.B. Carter. Transmission Electron Microscopy: A Textbook for Materials Science. Springer, New York, 2009.

[7] Z. Luo, S. Zhang, Y. Tang, D. Zhao. Quasicrystals in as-cast Mg-Zn-RE alloys. *Scripta Metall. Mater.* **28**, 1513–1518 (1993).

[8] D. Shechtman, I. Blech, D. Gratias, J. Cahn. Metallic phase with long-range orientational order and no translational symmetry. *Phys. Rev. Lett.* **53**, 1951–1953 (1984).

[9] L. Bendersky. Quasicrystal with one-dimensional translational symmetry and a tenfold rotation axis. *Phys. Rev. Lett.* **55**, 1461–1463 (1985).

[10] Y. Vasquez, Z. Luo, R.E. Schaak. Low-temperature solution synthesis of the non-equilibrium ordered intermetallic compounds Au_3Fe, Au_3Co, and Au_3Ni as nanocrystals. *J. Am. Chem. Soc.* **130**, 11866–11867 (2008).

CHAPTER 7

Imaging II

Imaging is the most intuitive way to characterize materials structures using the transmission electron microscope (TEM). The conventional imaging methods using mass-thickness contrast and diffraction contrast have been introduced in Imaging I (Chapter 5 in Volume 1). In this Chapter of Imaging II, scanning TEM (STEM) imaging and high-resolution TEM (HRTEM) imaging methods are presented.

7.1 STEM Imaging

7.1.1 Formation of STEM Images and Optics

To image the sample in STEM mode, a STEM attachment must be equipped on the TEM, which can be used for either LaB_6 or field-emission gun (FEG) sources.

In the STEM mode, the electron beam is confined to a very fine spot, which scans over the sample area, while signals transmitted through the sample are collected under the specimen. This beam raster manner for imaging is similar to the image in a scanning electron microscope (SEM). The STEM imaging ray diagram is shown in Fig. 7.1. By the double deflection scan coils, the electron beam is deflected away from the optical axis, whereas after the objective prefield (or condenser lens C3), the beam is aligned back straightly parallel to the optical axis. Therefore, the electron beam is controlled to be parallel to the optical axis during scanning over the specimen.

The signals below the specimen can be collected by different detectors: bright-field (BF), annular dark-field (ADF), and high-angle annular dark-field (HAADF) detectors, as shown in Fig. 7.2. The BF detector collects signals with very small scattering angles, with semiangle $\theta_1 < 10\ \text{mrad}$. The ADF detector collects signals at larger semiangles, with semiangle θ_2

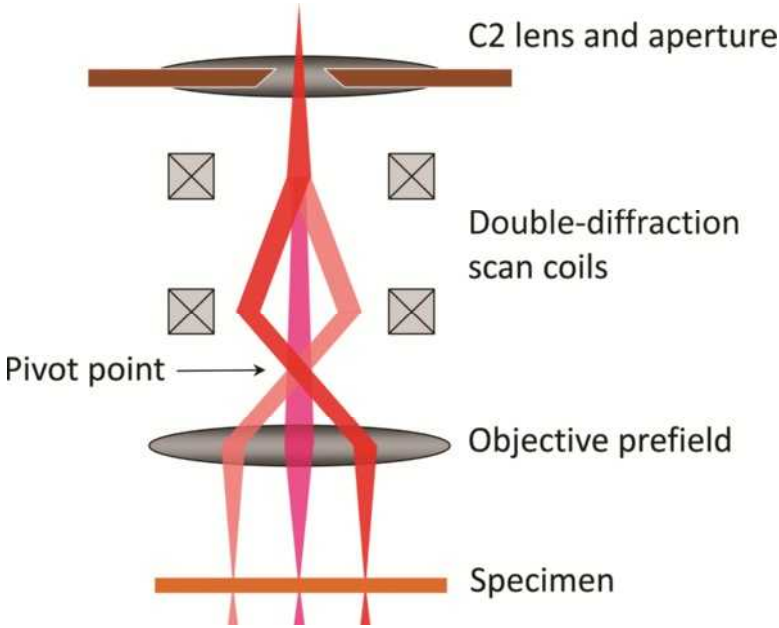

Fig. 7.1 Ray diagram showing STEM imaging.

in the range of $10\,\text{mrad} < \theta_2 < 50\,\text{mrad}$, which excludes the direct beam and thus the image is a dark-field image. The HAADF detector collects signals at high semiangles, with $\theta_3 > 50\,\text{mrad}$. Because of the limited applications of BF and ADF detectors, on most TEMs with STEM, only HAADF detectors are installed. The image collected using HAADF detector is called Z contrast image, since the contrast is related to the atomic number Z or thickness t.

In the electron–nucleus interaction, the Rutherford cross section σ between scattering angle θ_1 and θ_2 is expressed as [1]

$$\sigma = \left(\frac{m}{m_0}\right)^2 \frac{Z^2\lambda^4}{4\pi^3 a_0^2}\left(\frac{1}{\theta_1^2+\theta_0^2} - \frac{1}{\theta_2^2+\theta_0^2}\right) \tag{7.1}$$

where m is the electron mass; m_0, the electron rest mass; Z, atomic number; a_0, Bohr radius; and θ_0, Born screening angle which is given by

$$\theta_0 = 1.13\frac{m}{m_0}\frac{\lambda Z^{1/3}}{2\pi a_0} = \frac{1.13 Z^{1/3}}{137\beta} \tag{7.2}$$

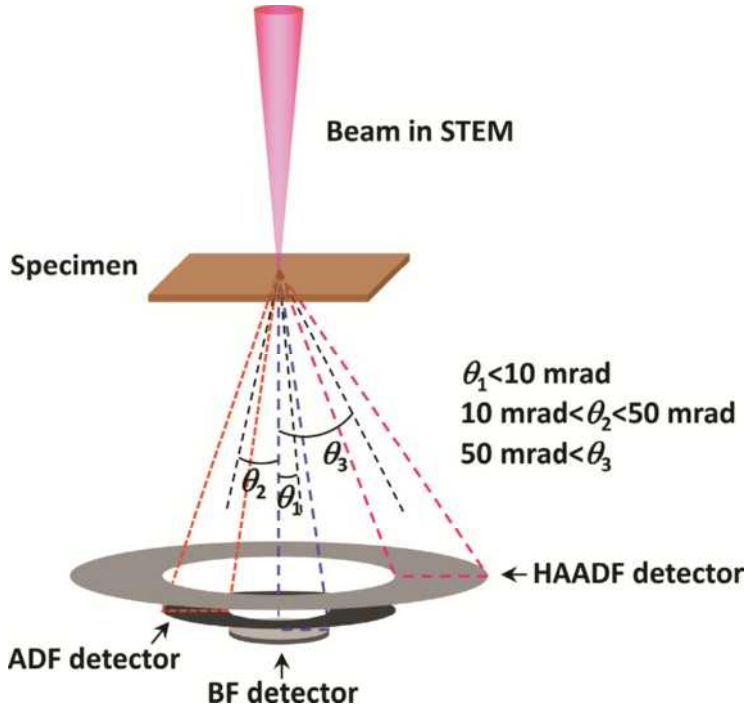

Fig. 7.2 Detection of STEM signals.

where $\beta = v/c$, the ratio of the electron velocity v to the velocity of light c. The intensity I_A of an element A in the specimen is given by

$$I_A = \sigma_A \cdot I \cdot t \cdot N \tag{7.3}$$

where I is the beam intensity, t is the specimen thickness, and N is the number of atoms per unit volume.

From the above equations, the contrast in STEM is proportional to Z^n or thickness t. For ideal Rutherford scattering, the power exponent $n = 2$ [2]. Hartel *et al.* [3] pointed out that the exponent n is always less than 2 because the atomic electron cloud screens the coulomb potential of the bare nucleus. For most detectors, n is in the range between 1.6 and 1.9 depending on the angles θ_1 and θ_2. Further, Wang *et al.* [4] showed experimentally that n varies strongly between 1.2 and 1.8, as the collection angle changes from 14 to 103 mrad.

The object with a larger Z or thicker t exhibits brighter contrast. The resolution of the Z contrast image depends on the beam size.

7.1.2 STEM Experimental Procedures

The STEM attachment on the TEM can be routinely used for imaging using the following procedures:

1. Find an area of interest at a low magnification (~10,000×).
2. In the STEM menu, click STEM, and the Diffraction mode will be activated; press the Diffraction button to deactivate it.
3. Conduct alignments of Beam Shift, Beam Tilt, Pivot Points, and Rotation Centering, and correct the Condenser astigmatism.
4. Press the Diffraction button, the HAADF detector is inserted.
5. Choose an appropriate camera length L (~100–150 mm for STEM at a low magnification) and spot size.
6. Select an area with higher contrast and adjust focus using the objective focus knob; correct any astigmatisms using Condenser stigmator.
7. Acquire to obtain a STEM image.

7.1.3 STEM Applications

The STEM imaging in TEM has wide applications in materials characterizations. The following are typical applications:

1. STEM Z contrast imaging to reveal chemical compositional information [1, 5, 6]. The object with higher Z or t shows higher intensity. Since it is possible to reach atomic-resolution STEM imaging, this is particularly important to identify atomic columns in HRTEM images; since phase contrast alone is used, it is difficult to identify atoms with similar lattice parameters (such as Si and Ge) [6].
2. Chemical analysis in conjunction with X-ray energy-dispersive spectroscopy (EDS) and electron energy-loss spectroscopy (EELS) using a fine beam, such as point, line scan, and mapping (refer to Chapter 8).
3. Imaging beam-sensitive samples [7]. The focused beam on a small area in a short time makes less damage compared with the entire area illumination in the TEM mode.

4. Imaging thicker samples. For thick samples, the TEM image becomes blurry since the object cannot be focused because of chromatic aberrations, whereas the chromatic aberration does not affect the STEM imaging contrast.

A comparison of STEM images with TEM images is presented in Fig. 7.3. The sample is a Ni-base superalloy [8], containing cuboidal γ' particles enriched in Ni, Al, W, and Ti. Located between γ' particles is the γ matrix, which is enriched in Cr, Co, and Mo. The width of the γ matrix is about 10–60 nm. The sample was deformed until fracture, containing high-density structural defects of dislocations and stacking faults.

Fig. 7.3(a) is a STEM image taken at a low magnification showing a large view area. Even though the sample is thick, the STEM image is well focused, whereas in the TEM image the upper region of Fig. 7.3(a) becomes very dark (not shown here). The framed area is magnified in Fig. 7.3(b), and the letters A–D are used to track the positions of four γ' particles. It is seen that γ phase exhibits higher intensity over the γ' phase, and such a contrast comes from the compositional difference between γ and γ'. However, in the TEM image in Fig. 7.3(c) taken by a small objective aperture, the high-density dislocations exhibit strong diffraction contrast, which almost conceals the mass contrast between γ and γ'. Using a larger objective aperture, the image in Fig. 7.3(d) exhibits less diffraction contrast effect to reveal the γ/γ' phases. The central dark-field (CDF) image in Fig. 7.3(e) shows the γ' phase only, and the weak-beam dark-field (WBDF) image in Fig. 7.3(f) shows dislocations only. In the STEM imaging mode, if the camera length is sufficiently short, the HAADF detector collects signals only from large angles (even excluding HOLZ diffraction), and thus the diffraction effect can be excluded in STEM images.

The STEM imaging can reach atomic resolution. Fig. 7.4 shows aberration-corrected STEM HAADF images of $Bi(Fe, Mn)O_3$ (BFMO) films grown on $SrTiO_3$ (STO) (Fig. 7.4a) and $LaAlO_3$ (LAO) (Fig. 7.4b) substrates, respectively, both along the substrate $[100]_p$ zone axis (the subscript p stands for perovskite) [9]. Although the films were grown under the same deposition conditions, distinctly different atomic structures are found. An enlarged image at the interface is shown in the

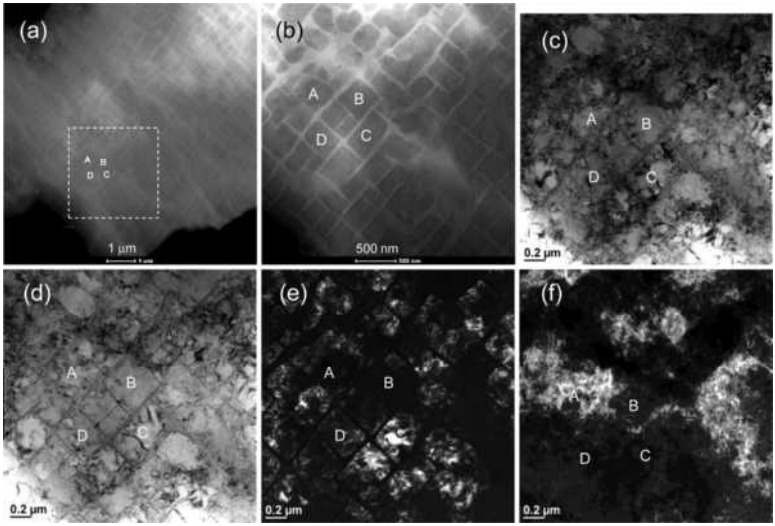

Fig. 7.3 STEM and TEM images of a Ni-base superalloy containing γ′ cubes with γphase between them. (a) STEM at a lower magnification; (b) STEM at a higher magnification from the framed area in (a); (c) TEM image using a small objective aperture showing strong diffraction contrast of dislocations; (d) TEM image using a large objective aperture showing less diffraction contrast; (e) CDF image showing γ′ phase; (f) WBDF image showing dislocations.

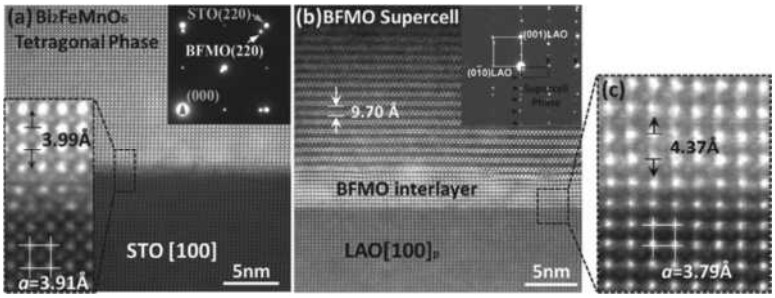

Fig. 7.4 Aberration-corrected atomic-resolution STEM images of BFMO films on STO (a) and LAO (b) substrates. A magnified image from the framed area in (a) is shown in the left inset, and from (b) is shown in (c). SAED patterns are inserted.

left-hand inset of Fig. 7.4(a). The STO substrate along the $[100]_p$ axis presents a typical perovskite lattice, where Sr columns show as bright spots (marked with a square), while Ti–O columns are located in the centers of the Sr square lattice in lower intensities. The BFMO on the

LAO substrate, however, shows a supercell (SC) structure along the *c*-axis with a thin interlayer between them, as shown in the enlarged image in Fig. 7.4(c).

The HAADF images of the SC structure along three major zone axes of $[100]_p$, $[110]_p$, and $[010]_p$, respectively, are shown in Fig. 7.5(a)–(c), along with structure model of the SC phase along these three directions in Fig. 7.5(d)–(f). The large bright image spots with highest intensities are the positions of Bi, while between them are Mn/Fe atoms with lower intensities. In Fig. 7.5(a) along $[100]_p$, the neighboring double Bi_2O_2 sheets, as marked with dots, are aligned vertically along the horizontal direction. However, along the $[110]_p$ and $[010]_p$ zones, as shown in Fig. 7.5(b) and (c), respectively, the neighboring double Bi_2O_2 sheets are offset by half a period along the horizontal direction. Between the neighboring double Bi_2O_2 sheets are two layers of Fe–O/Mn–O, which have a similar triangle-stripe feature (consisting of weak dots) matching the Bi_2O_2 lattice 1:1 along the $[100]_p$ zone axis (Fig. 7.5a) but 4:3 under the $[010]_P$ zone axis (Fig. 7.5c). A structural model of the SC was proposed,

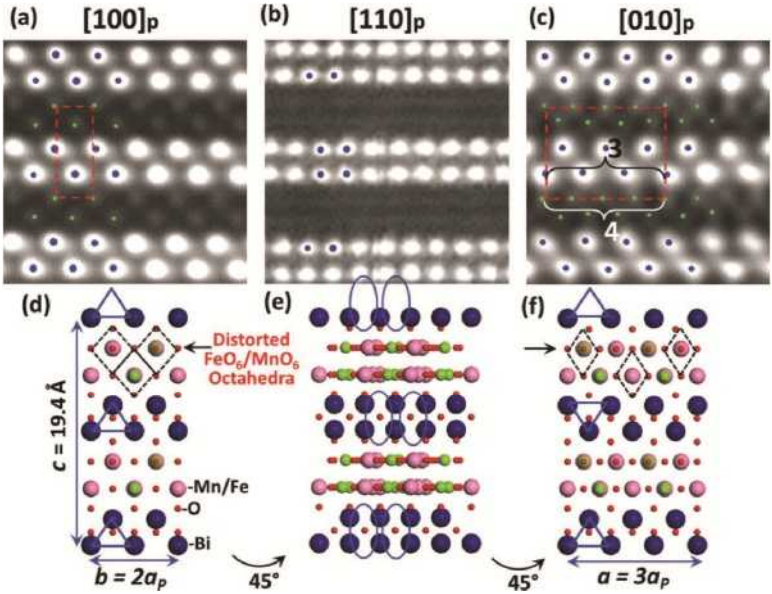

Fig. 7.5 STEM images along the $[100]_p$ (a), $[110]_p$ (b), and $[010]_p$ (c) zone axes. The image features are compared with three projections of a structural model (d–f).

which has $a = 3a_p$ (a_p stands for the lattice parameter of the pseudo-perovskite BFMO phase), $b = 2a_p$ ($a_p \approx 3.99$ Å), and $c \approx 19.40$ Å. The structure projections shown in Fig. 7.5(d)–(f) are consistent with the STEM HAADF images.

7.2 High-Resolution Transmission Electron Microscopy

7.2.1 *Principles of HRTEM*

The HRTEM image is formed based on phase contrast [6, 10, 11]. The sample should be thin enough, typically less than 10 nm, to get HRTEM images. The image resolution depends on the instrument specifications. A modem TEM with LaB_6 or FEG at 200 kV or higher can routinely reach the atomic resolution of several angstroms. The HRTEM image formation process is illustrated in Fig. 7.6, which is described below in detail.

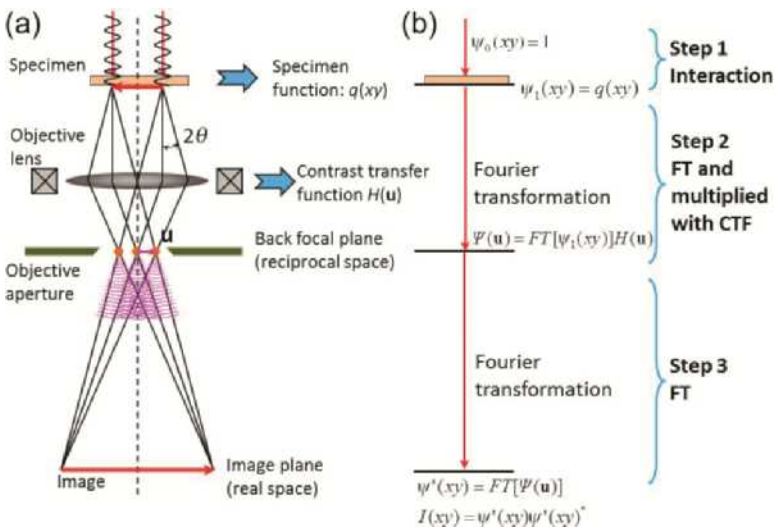

Fig. 7.6 Formation of HRTEM image. (a) Schematic imaging process in TEM; (b) mathematical processing.

7.2.1.1 Interaction with Specimen

The electron wavelength is simply expressed as

$$\lambda = \frac{h}{\sqrt{2meE}} \tag{7.4}$$

where h is Planck's constant, m is mass, e is the electron charge, and E is the energy of electrons. After passing through the specimen, due to the interaction with the specimen atoms, the wavelength becomes

$$\lambda' = \frac{h}{\sqrt{2me\left(E + \phi(xyz)\right)}} \tag{7.5}$$

where $\phi(xyz)$ is the specimen potential. This means that when the electrons travel inside the specimen, the wavelength is shortened, whereas when they leave the specimen, the wavelength recovers to the original length; however, the phase of the electron wave is changed, as shown in Fig. 7.7. The phase change after passing through a slice with thickness dz is:

$$\begin{aligned} d\gamma &= 2\pi\left(\frac{dz}{\lambda'}\right) - 2\pi\left(\frac{dz}{\lambda}\right) \\ &= 2\pi\frac{dz}{\lambda}\left[\frac{\sqrt{E + \phi(xyz)}}{\sqrt{E}} - 1\right] \\ &= 2\pi\frac{dz}{\lambda}\left[\left(1 + \frac{\phi(xyz)}{E}\right)^{\frac{1}{2}} - 1\right] \\ &\approx \frac{\pi}{\lambda E}\phi(xyz)\,dz \\ &= \sigma\phi(xyz)dz \end{aligned} \tag{7.6}$$

where $\sigma = \pi/(\lambda E)$, which is an interaction constant that depends only on the electron source. Thus, the phase shift over a thickness t is

$$\begin{aligned} \int_0^t \sigma\,\phi(xyz)\,dz &= \sigma\int_0^t \phi(xyz)\,dz \\ &= \sigma\phi(xy) \end{aligned} \tag{7.7}$$

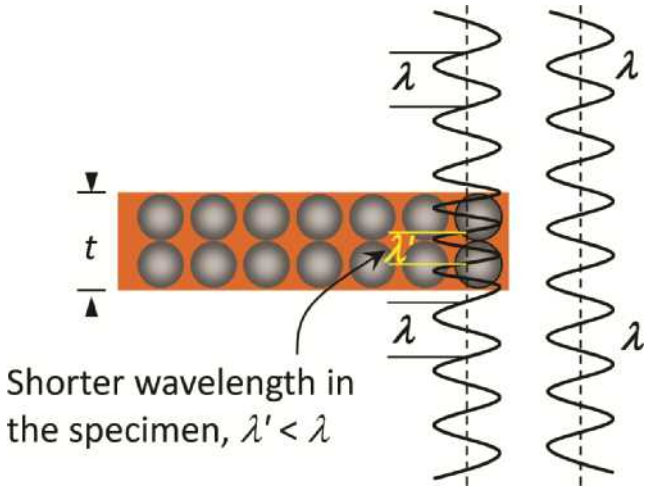

Fig. 7.7 Interaction of electron waves with specimen atoms. Note that the wavelength is shortened when the electron wave travels inside the specimen causing a phase shift at the exit.

where $\phi(xy)$ is the potential projection on the (xy) plane along the z-direction. Specimen transmission function (or phase grating function) without absorption is expressed as

$$q(xy) = \exp\left[-i\sigma\phi(xy)\right] \tag{7.8}$$

For very thin crystals, $\sigma\phi(xy) \ll 1$ (much less than 1), we obtain weak-phase object approximation (WPOA) as follows

$$q(xy) = 1 - i\sigma\phi(xy) \tag{7.9}$$

As shown in Fig. 7.6, at the sample exit, the wave function becomes

$$\psi_1 = q(xy) \tag{7.10}$$

7.2.1.2 Influence of Contrast Transfer Function

The first image is formed after the electrons pass through the objective lens. As shown in Fig. 7.6(b), the wave function on the back focal plane is mathematically a Fourier transformation (FT) of the wave function $\psi_1(xy)$ but multiplied by a contrast transfer function (CTF), $H(\mathbf{u})$, as follows:

$$\psi(\mathbf{u}) = FT[\psi_1(xy)]H(\mathbf{u}) \tag{7.11}$$

where **u** is a reciprocal vector with a length of u. Here, $H(\mathbf{u})$ includes the following components:

$$H(\mathbf{u}) = A(\mathbf{u}) \cdot E(\mathbf{u}) \cdot B(\mathbf{u}) \tag{7.12}$$

where $A(\mathbf{u})$, $E(\mathbf{u})$, and $B(\mathbf{u})$ are aperture function, envelope function, and aberration function, respectively.

(a) Aperture Function A(u): Suppose the objective aperture used for imaging has a radius r (Fig. 7.8), the aperture function is

$$A(\mathrm{u}) = \begin{cases} 1, & u < r \\ 0, & u \geq r \end{cases} \tag{7.13}$$

(b) Envelope Function *E*(u): The envelop function $E(\mathbf{u})$ includes chromatic aberration envelope function $E_c(\mathbf{u})$ and spatial coherence envelope function $E_s(\mathbf{u})$

$$E(\mathbf{u}) = E_c(\mathbf{u}) \cdot E_s(\mathbf{u}) \tag{7.14}$$

The chromatic aberration envelope function $E_c(\mathbf{u})$ is related to the temporal coherence (Fig. 7.9a), which is expressed as

$$E_c(\mathbf{u}) = \exp\left[-\frac{1}{2}(\pi\lambda\delta)^2 u^4\right] \tag{7.15}$$

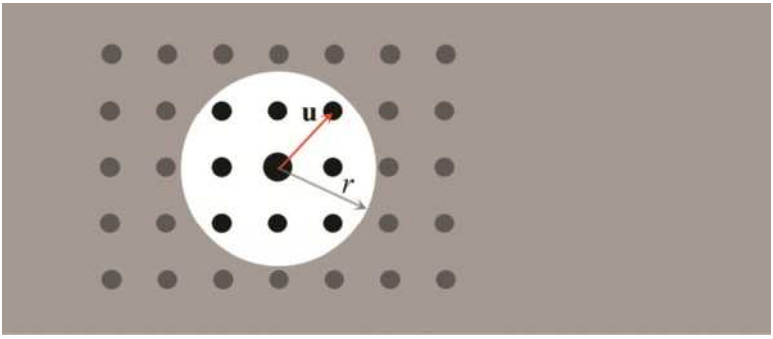

Fig. 7.8 Objective aperture used for HRTEM imaging with a radius r.

where δ is the defocus spread due to the chromatic aberration (Fig. 7.9a),

$$\delta = C_c \left[4\left(\frac{\Delta I_{obj}}{I_{obj}}\right)^2 + \left(\frac{\Delta E}{V_{acc}}\right)^2 + \left(\frac{\Delta V_{acc}}{V_{acc}}\right)^2 \right]^{1/2} \tag{7.16}$$

where C_c is the chromatic aberration coefficient, I_{obj} is the objective lens current, and V_{acc} is the accelerating voltage. The terms of $\Delta I_{obj}/I_{obj}$ and $\Delta V_{acc}/V_{acc}$ represent the instabilities in the objective lens current and high-voltage supply, respectively; and $\Delta E/V_{acc}$, the intrinsic energy spread in the electron gun. The spatial coherence envelope function $E_s(\mathbf{u})$ is related to the spatial coherence (Fig. 7.9b), which is expressed as

$$E_s(\mathbf{u}) = \exp\left[-\left(\frac{\pi\alpha}{\lambda}\right)^2 \left(C_s\lambda^3 u^3 + \Delta f \lambda u\right)^2 \right] \tag{7.17}$$

where α is the beam divergence semiangle (Fig. 7.9b), C_s is the coefficient of spherical aberration, and Δf is the defocus value (underfocus is defined as negative, overfocus as positive, and in-focus as $\Delta f = 0$).

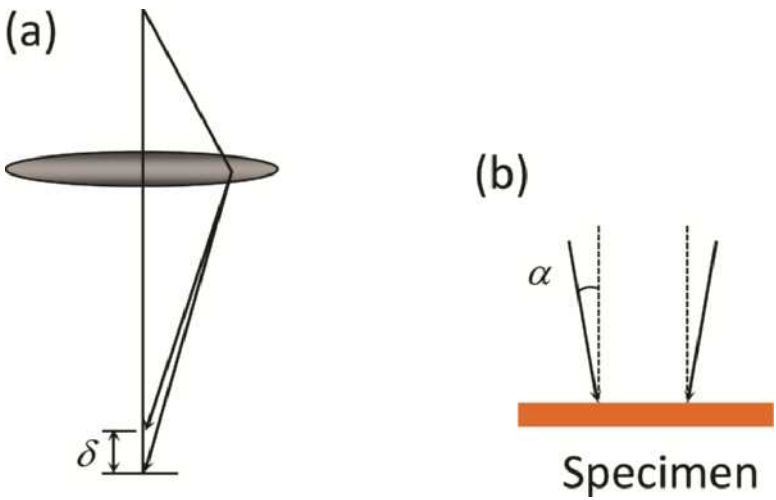

***Fig. 7.9** (a) Temporal coherence; (b) spatial coherence.*

(c) Aberration Function *B*(u): Since the objective lens is impacted by the spherical aberration (refer to Section 3.2.2 in Volume 1), a phase shift is induced by the spherical aberration, which is

$$\chi(\mathbf{u}) = \frac{\pi}{2} C_s \lambda^3 u^4 \tag{7.18}$$

Defocus Δf also produces a phase shift with

$$\chi(\mathbf{u}) = \pi \Delta f \lambda u^2 \tag{7.19}$$

The total phase shift is thus

$$\chi(\mathbf{u}) = \frac{\pi}{2} C_s \lambda^3 u^4 + \pi \Delta f \lambda u^2 \tag{7.20}$$

Scherzer [12] deduced that the optimum defocus can be obtained when

$$\frac{d\chi}{du} = 0 \text{ and } \chi = -\frac{2}{3}\pi \tag{7.21}$$

From Eq. 7.20,

$$\frac{d\chi}{du} = 2\pi C_s \lambda^3 u^3 + 2\pi \Delta f \lambda u = 0 \tag{7.22}$$

Thus,

$$\Delta f = -C_s \lambda^2 u^2 \tag{7.23}$$

Substitute Eq. 7.23 into Eq. 7.20 and let $= -\frac{2}{3}\pi$, a relationship $C_s \lambda^3 u^4 = \frac{4}{3}$ is obtained. Combining this relationship with Eq. 7.23 defines the Scherzer defocus as

$$\Delta f_{\text{Sch}} = -\sqrt{\frac{4}{3} C_S \lambda} \approx -1.2\sqrt{C_S \lambda} \tag{7.24}$$

Take a 200 kV (λ = 0.00251 nm) TEM with C_S = 0.8 mm as an example. According to Eq. 7.24, Δf_{Sch} = −51.74 nm. Therefore, from Eq. 7.20, it is possible to plot χ, sinχ, and cosχ as a function of u, as shown in Fig. 7.10(a). Eq. 7.21 corresponds to the minimum point of the χ curve, which satisfies $d\chi/du$ =0. Under the Scherzer defocus condition,

the sinχ curve, exhibits a wide flat range with the valley value of −1. This range can transfer the contrast with the same sign (all negative) and with the highest contrast (at or near −1, far away from zero). Therefore, this condition is the optimum condition for HRTEM phase-contrast imaging with the highest contrast. The first zero point, as marked with u_{Sch}, is the limit to reveal details that is the resolution of the microscope r_{Sch}, as shown in Fig. 7.10(a). The sinχ curve only is plotted in Fig. 7.10(b) for details. Substitute Eq. 7.24 in Eq. 7.20 and let $\chi(\mathbf{u}) = 0$,

$$\frac{\pi}{2} C_s \lambda^3 u^4 + \pi \left(-\sqrt{\frac{4}{3} C_S \lambda} \right) \lambda u^2 = 0$$

Thus,

$$u_{\mathrm{Sch}} = \sqrt[4]{\frac{16}{3} \frac{1}{C_s \lambda^3}} \approx 1.52 C_s^{-\frac{1}{4}} \lambda^{-\frac{3}{4}} \tag{7.25}$$

$$r_{\mathrm{Sch}} = \frac{1}{u_{\mathrm{Sch}}} = \sqrt[4]{\frac{3}{16} C_s \lambda^3} \approx 0.66 C_s^{\frac{1}{4}} \lambda^{\frac{3}{4}} \tag{7.26}$$

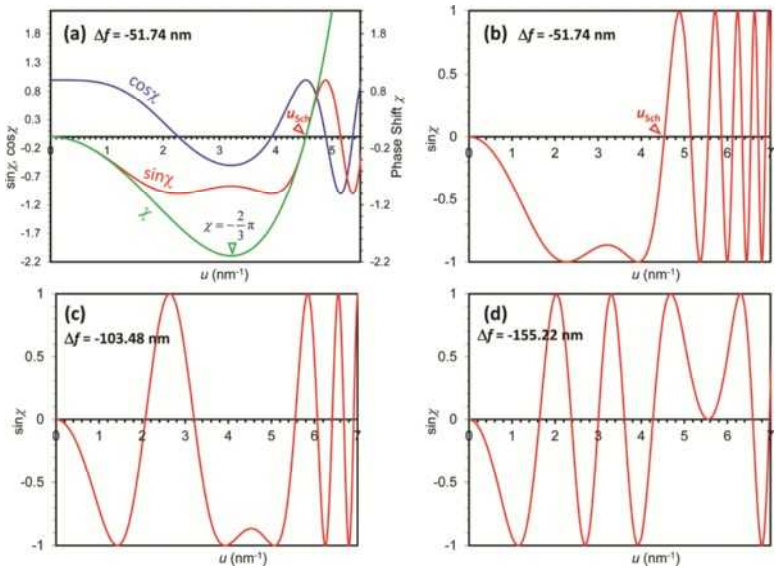

Fig. 7.10 (a) Plots of χ, sinχ, and cosχ as a function of u, under Scherzer defocus of Δf_{Sch} = −51.74 nm; (b) sinχ only (Δf_{Sch} = −51.74 nm); (c) defocus Δf = −103.48 nm; (d) defocus Δf = −155.22 nm. Computation parameters: wavelength λ = 0.00251 nm for 200 kV, and C_s = 0.8 mm.

In the example of Fig. 7.10(a) or (b), u_{Sch} = 4.53 nm^{-1}, and resolution $r_{\mathrm{Sch}} = 1/u_{\mathrm{Sch}}$ = 0.22 nm.

Fig. 7.10(c) and (d) shows two curves with two larger defocus values than the Scherzer defocus. It is seen that as the u moves to the higher frequency, the $\sin\chi$ curve changes signs (+ or −), indicating its phase reversals. Note that in Fig. 7.10(c), a passband is present with higher resolution when it reaches zero, which mean more details may be resolved using the defocus, whereas proper image interpretation is required due to the phase signs.

Now we consider the effects of envelop function $E(\mathbf{u}) = E_{\mathrm{c}}(\mathbf{u}) \cdot E_{\mathrm{s}}(\mathbf{u})$ on $H(\mathbf{u})$. These two $E_{\mathrm{c}}(\mathbf{u})$ and $E_{\mathrm{s}}(\mathbf{u})$ functions are plotted in Fig. 7.11(a) and (b), respectively, and their product is the envelop function $E(\mathbf{u})$, as plotted in Fig. 7.11(c). Multiplying $E(\mathbf{u})$ on $\sin\chi$ (Fig. 7.10b) yields the CTF, $H(\mathbf{u})$, as shown in Fig. 7.11(d). Note that in order to guide the eye to see $H(\mathbf{u})$, an additional curve with $-E(\mathbf{u})$ is also imposed which is symmetrical to $E(\mathbf{u})$ along the horizontal axis. It is seen that the amplitude quickly attenuates at higher frequencies, reducing the information limit.

7.2.1.3 Formation of Image in the Image Plane

The last process is the formation of image in the image plane, which is just a simple mathematical Fourier transformation of the wave function $\Psi(\mathbf{u})$ from the reciprocal space to the real space, that is, the wave function on the image plane is

$$\psi'(xy) = FT[\Psi(\mathbf{u})] \tag{7.27}$$

Thus, the image intensity is

$$I(xy) = \psi'(xy)\psi'(xy)^* \tag{7.28}$$

where $\psi'(xy)^*$ is a conjugate function of $\psi'(xy)$.

Let's consider a simple case when the sample is very thin as a WPOA. From Eq. 7.9, $q(xy) = 1 - i\sigma\phi(xy)$. Thus, in the back focal plane,

$$\begin{aligned}\Psi(\mathbf{u}) &= FT\left[q(xy)\right]\exp\left[i\chi(\mathbf{u})\right] \\ &= \delta(\mathbf{u}) + \sigma\Phi(\mathbf{u})\sin\chi(\mathbf{u}) - i\sigma\Phi(\mathbf{u})\cos\chi(\mathbf{u})\end{aligned} \tag{7.29}$$

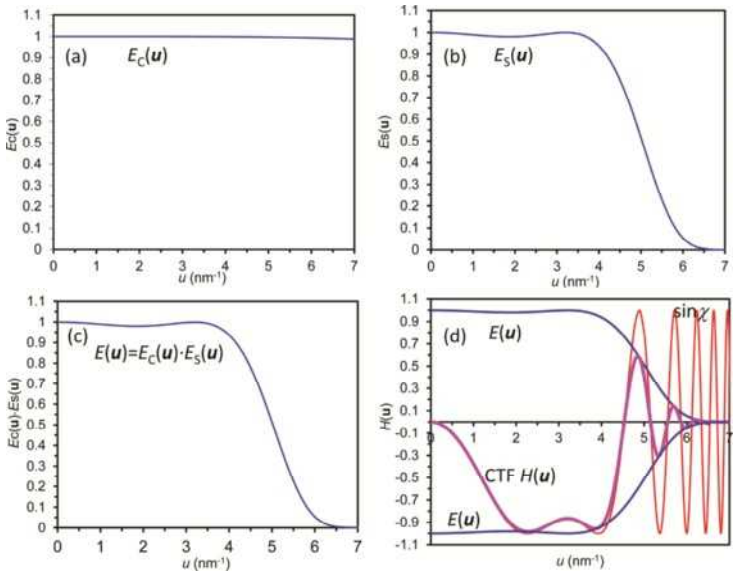

Fig. 7.11 *(a) Chromatic aberration envelope function $E_c(u)$; (b) spatial coherence envelope function $E_s(u)$; (c) envelop function $E(\mathbf{u}) = E_c(\mathbf{u}) \cdot E_s(\mathbf{u})$; (d) contrast transfer function $H(u)$. Computation parameters: wavelength $\lambda = 0.00251$ nm for 200 kV, $C_s = 0.8$ mm, $C_c = 8$ mm, $\Delta E = 10$ kV, $\alpha = 0.7$ mrad, and $\Delta f_{Sch} = -51.74$ nm.*

In the image plane, the wave function is obtained by the FT of Eq. 7.29,

$$\begin{aligned}\psi(xy) &= FT\left[\delta(\mathbf{u}) + \sigma\Phi(\mathbf{u})\sin\chi(\mathbf{u}) - i\sigma\Phi(\mathbf{u})\cos\chi(\mathbf{u})\right] \\ &= 1 + FT\left[\sigma\Phi(\mathbf{u})\sin\chi(\mathbf{u})\right] - iFT\left[\sigma\Phi(\mathbf{u})\cos\chi(\mathbf{u})\right] \\ &= 1 + \sigma\Phi(xy) \otimes FT\sin\chi(\mathbf{u}) - i\sigma\phi(xy) \otimes FT\cos\chi(\mathbf{u}) \qquad (7.30)\end{aligned}$$

Here, the symbol $\otimes$ stands for a convolution operation. Therefore, the intensity of the image is

$$\begin{aligned}I(xy) = \psi'(xy)\psi'(xy)^* &= \left[1 + \sigma\phi(xy) \otimes FT\sin\chi(\mathbf{u})\right]^2 \\ &\quad + \left[\sigma\phi(xy) \otimes FT\cos\chi(\mathbf{u})\right]^2 \\ &\approx 1 + 2\sigma\phi(xy) \otimes FT\sin\chi(\mathbf{u}) \qquad (7.31)\end{aligned}$$

where we ignore the σ^2 terms for the thin specimen. Under optimum phase-contrast imaging condition, $\sin\chi(\mathbf{u}) = -1$, and thus

$$I(xy) = 1 - 2\sigma\phi(xy) \qquad (7.32)$$

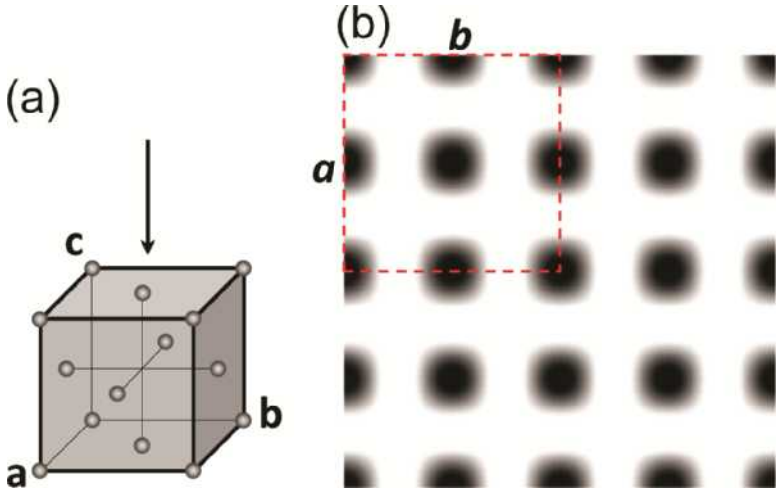

Fig. 7.12 (a) Structure model of FCC; (b) image under WPOA (a unit cell is outlined).

This means at atomic positions, $I(xy) < 1$, and the atoms show black contrast. An example is shown in Fig. 7.12 for an FCC crystal (Fig. 7.12a). Along the [001] zone axis direction, atoms appear as dark spots in a square pattern, and a unit cell is outlined in Fig. 7.12(b).

7.2.2 *Experimental Operations*

Since the HRTEM images are taken at high magnifications, normally at least 100,000×, instrumental alignments are crucial to get good images. The alignments include eucentric height adjustment, gun alignment, condenser lens astigmatism correction, voltage centering, and objective lens astigmatism correction (refer to Chapter 3 in Volume 1 for the alignments). The voltage centering should be done at higher magnifications, and the selected object for the voltage centering alignment should be nearby the sample object, that is, they are at about the same height; hence, the objective lens current does not change much while focusing. The objective lens astigmatism also greatly affects the image quality. Select an amorphous area nearby for the astigmatism correction, such as amorphous carbon film or near a hole edge of ion-milled sample, which is sometimes a damaged amorphous area. The correction should be done

at the highest magnification which is the same one used for imaging. If it is aligned at a higher magnification, imaging at a lower magnification does not require repeated alignments.

Below are several special precautions to get good HRTEM images:

1. Use the highest accelerating voltage on the instrument to get the highest resolution on the instrument (refer to Eq. 7.26).
2. Use newly prepared fresh sample. If the thin sample is exposed in air for long time, the surface may be oxidized or contaminated and noises will be introduced. For powder samples deposited on carbon support film, prepare samples and immediately work in TEM.
3. To achieve good image stability, install sample to the TEM and wait for sufficiently long time before starting HRTEM.
4. Select very thin areas. If it is a bulk sample prepared by ion milling or electropolishing, select thin area before the first thickness fringe appears. For powder samples on support film, look for wedge-shaped transparent samples, which may contain thin areas. In the image mode with an objective aperture inserted, grains or particles appearing as slightly darker than others may be already at or near a major zone axis orientation.
5. The support film must be conductive, such as pure carbon film, and ideally with holes so that the observation can be done on the sample hung on the holes to eliminate the background noise from the support film.
6. At high magnification, the sample may be damaged because of the increased electron dose on the small area at high magnification. Fill the liquid nitrogen in the anti-contamination device to reduce the sample damage. Use objective aperture, which may increase the sample stability (refer to Section 3.1.4 in Volume 1). Reduce the beam intensity and gradually increase the magnification. Perform alignment in a nearby area and then move to the sample area to take image quickly. Prolonged exposure at high magnification may cause sample damage.
7. If it is a bulk sample, align the sample orientation to get a zone axis pattern as symmetrical as possible (do not use beam tilt here).

Check the diffraction pattern using the smallest diffraction aperture to ensure the pattern is from the small image area.

8. Insert and center the objective aperture. Normally the largest aperture (or even no aperture) is used, which is aligned to the optical axis for axial illumination (Fig. 7.13a). However, different imaging approaches have been proposed, such as using a small objective aperture to get a lower-resolution image [13, 14] as shown in Fig. 7.13(b), beam-tilted dark-field imaging (the aperture still remains centered) [15, 16] as shown in Fig. 7.13(c), and imaging when the crystal is tilted [17] as shown in Fig. 7.13(d). However, the beam tilt or crystal tilt may introduce artifacts to the HRTEM images, as discussed in reference [18].
9. Appropriately underfocus the image. At the sample edge, adjust the focusing knob when the fringes (the Fresnel fringes) disappear, or look at the image when minimum contrast is obtained, and set the defocus

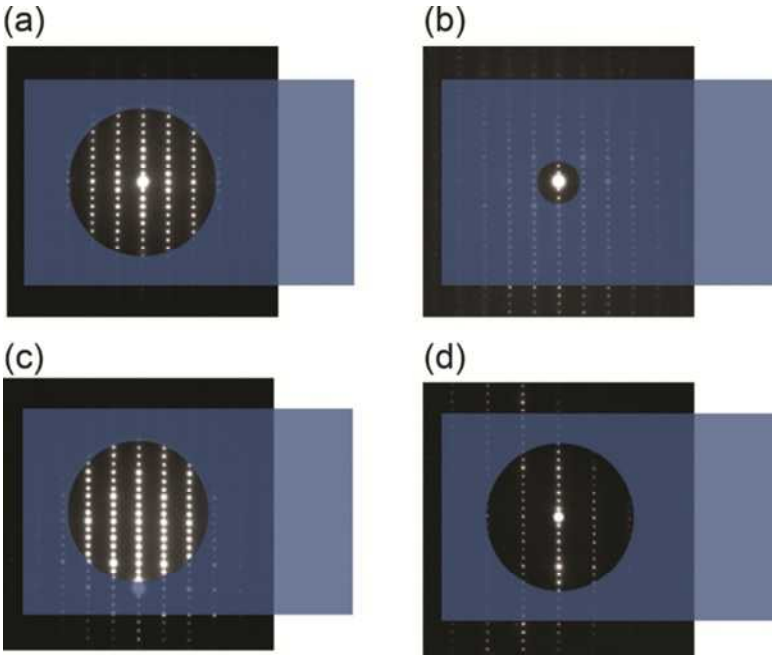

Fig. 7.13 Imaging methods using the objective aperture. (a) Normal axial illumination; (b) small objective aperture is used; (c) beam-tilted dark-field imaging; (d) crystal is tilted.

value as $\Delta f = 0$. Afterward, use focusing knob to get the Scherzer defocus (the focusing values can be found on the instrument screen), which is the ideal defocus value for imaging. If the sample is very thin, under the Scherzer defocus the metal atoms should appear as dark image spots. Take a series of images with varied defocus values as needed and record the experimental defocus Δf.

10. When HRTEM is done, take images at lower magnifications as well to get an overview; take SAED patterns from the same area for structural information, and any other analytical work (refer to Chapter 8) if needed.

Fig. 7.14(a) is an HRTEM image printed at a lower magnification to show a large view. It shows a modulated $HgBa_2Ca_3Cu_4O_{10+\delta}$ (Hg-1234) structure projected along its **a**-axis from a specimen crystal with a wedge-shaped edge [19]. The image was taken near Scherzer defocus value (–40 nm) according to the Fresnel fringes at the edge, which implies that in the thinnest parts the heavy cations are imaged as dark spots. A magnified image from an area marked by white dotted lines is shown in Fig. 7.14(b). In Fig. 7.14(b), the positions of the constituent cations in the thin area are identified by comparing with the simulation insert at top-right of the figure. Referring to the straight line at the top of Fig. 7.14(b), it is found that the mercury is not located exactly on a plane but with slight sinusoidal displacement along **c** as schematically indicated by upward and downward arrows. This effect is clearer in the thicker region in Fig. 7.14(b), where slight sinusoidal displacements are also observed at BaO, CuO_2, and Ca layers along **c**-axis, as indicated by upward and downward arrows at the bottom of Fig. 7.14(b). In the two BaO layers adjacent to the HgO_δ layer, the white spots of the upper layer are brighter than in the lower one, as pointed out by two arrowheads on the right side of Fig. 7.14(b). In the thicker area where the anomalous contrast is enhanced, it is found that the upper two Ca layers appear abnormally bright while the lower Ca layer is darker. For the CuO_2 layers, the upper layer is brighter than the lower one, especially the lowest CuO_2 layer appears to be in abnormally dark contrast. Such asymmetrically distributed anomalous contrast proves that the (001)

mirror symmetry of the basic structure is not present in these regions. A similar absence of (001) mirror symmetry was also observed in $Tl_2Ba_2CaCu_2O_y$ thin films in reference [20].

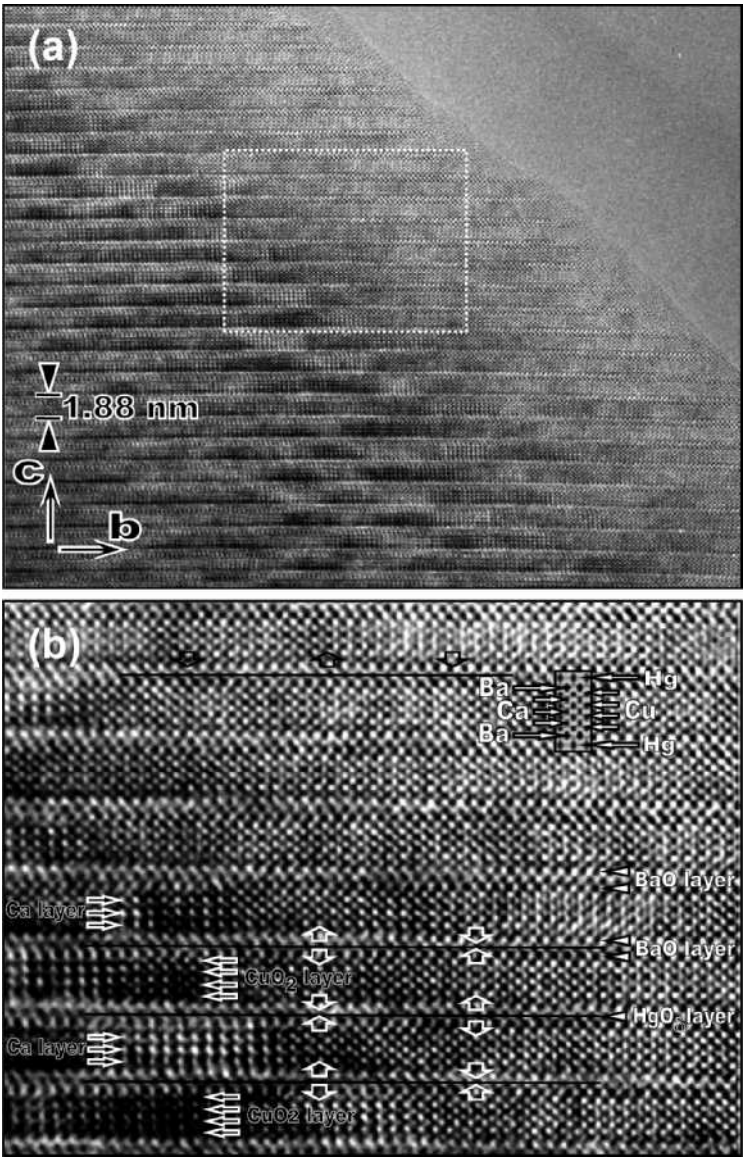

Fig. 7.14 HRTEM image of modulated Hg-1234 crystals projected along the a-axis (a), and (b) is a magnified image from the area with dotted lines in (a). Inserted in (b) is a simulated image.

7.2.3 *Image Interpretation and Simulation*

Since HRTEM images are based on phase contrast, the images should be interpreted with image simulations. The simulation can be done using a multislice method [21–24], and several programs have been available. The following data are needed to input:

1. Sample crystallographic data, including unit cell lattice parameters, space group, atom positions, Debye–Waller factor (usually ignored), and atomic occupations. Normally the atoms are assigned with atomic scattering factors of neutrons, while the user may change the scattering factors for ions, especially for small scattering angles [13, 14, 25].
2. Microscope parameters, including voltage (in kV), C_s (in mm), δ (in Å or nm), and α (in mrad).
3. Imaging conditions, including zone axis [*UVW*], thickness *t* (a single thickness or a series of thicknesses), defocus (negative for underfocus as convention, but some program may define a position values for underfocus; a single defocus or a series of defocus values), objective lens aperture size (Å^{-1} or nm^{-1}) and center position (*x*, *y*) (in the units of *h* and *k*, respectively), crystal tilt, which is expressed as the center of the Laue circle (*x*, *y*) (in the units of *h* and *k*, respectively), beam tilt, which is expressed as the center of optical axis (*x*, *y*) (in the units of *h* and *k*, respectively), and mechanical vibration (in Å or nm).

An example of image simulation is shown in Fig. 7.15. The crystal is $YBa_2Cu_3O_{7-x}$ (YBCO) projected along [100] direction, as shown in the structural model in Fig. 7.15(a). Simulations are done using the following parameters:

1. Lattice parameters a = 3.82 Å, b = 3.89 Å, c = 11.68 Å, space group #47 (*Pmmm*), atom positions, Debye–Waller factor, and atomic occupations of all atoms (Y, Ba, Cu, and O).
2. Voltage = 400 kV, C_s = 1 mm, δ = 80 Å, and α = 0.55 mrad.
3. [*UVW*] = [100], *t* starts from 20 and ends at 100 Å with a step of 20 Å, defocus starts from –200 and ends at –500 Å with a step of

−100 Å, objective lens aperture size = 0.68 $Å^{-1}$ and its center position = (0, 0), center of Laue circle = (0, 0), center of optical axis = (0, 0), and mechanical vibration = 0 Å.

A montage of simulated images is shown in Fig. 7.15(b) with variations of defocus Δf and thickness t. Unit cells are outlined, and each image contains 2×4 cells. According to Eq. 7.24, the Scherzer defocus $\Delta f_{Sch} = -46.76$ nm. When the sample is very thin (2 nm), the image appears as white spots under $\Delta f = -20$ nm; when it is close to the Scherzer defocus with $\Delta f = -40$ nm, the atomic positions appear as dark spots. As the thickness increases, the contrast varies considerably, and when $t \geq 8$ nm, the images do not show the atomic rows compared with the structural model in Fig. 7.15(a). Therefore, it is essential to use very thin samples for HRTEM.

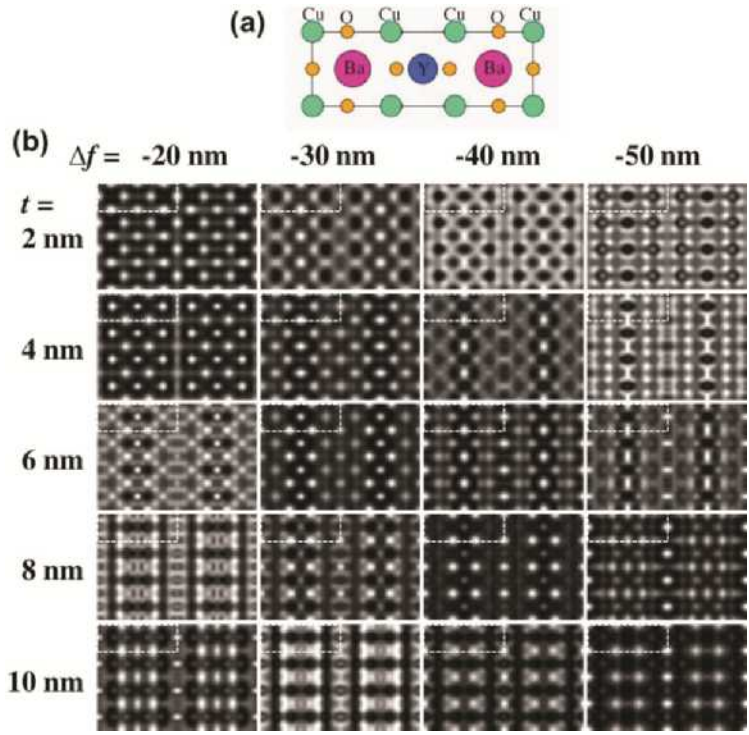

***Fig. 7.15** (a) Structural model of YBCO; (b) simulated image montage of YBCO under different defocus Δf (horizontal) at different thickness t (vertical).*

Fig. 7.16 shows a real HRTEM image of YBCO along [100] taken by a 400-kV TEM. The image was taken near the Scherzer defocus $\Delta f = -45$ nm as justified by the Fresnel fringes at the edge. The simulated image matches with the experimental image, and the atomic positions of metals are well identified, with 1 row of Y atoms, 2 rows of Ba atoms, and 3 rows of Cu atoms.

Only when the sample is very thin and the image is taken under Scherzer defocus, can the HRTEM image be interpreted as the atomic positions. Under other conditions, even though the image spots look like the correct atomic positions compared with the structure model, they may not be at the exact correct positions due to the phase problem. A typical example is Si projected along <110> direction, with dumbbell spacing of 1.36 Å [26, 27]. If it is not correctly resolved, the dumbbell spacing is different.

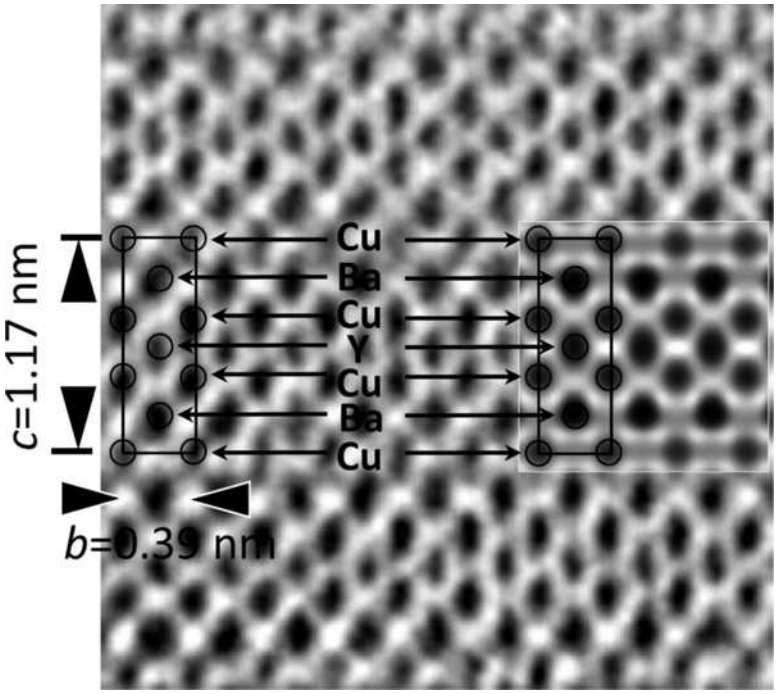

***Fig. 7.16** Experimental HRTEM image of YBCO compared with an inserted image simulation.*

7.2.4 *Image Processing*

Imaging processing of the HRTEM images can provide more information [28]. The image processing is based on the concept that an image is composed of pixels, with an intensity value at each pixel. As shown in Fig. 7.17(a), the image is composed of 16×16 pixels, and the intensity data are listed in Fig. 7.17(b).

A commonly used image processing is the noise elimination by Fourier peak filtering. As shown in Fig. 7.18(a), the experimental HRTEM image contains noises, possibly from surface oxidation layers. Fig. 7.18(b) shows its FT pattern, with reflection peaks clearly presented. On all of these peak positions, masks are applied, as shown in Fig. 7.18(c). The inverse FT (IFT) results a filtered image, which shows structures clearly as shown in Fig. 7.18(d).

To understand this Fourier transformation, Fig. 7.19(a) and (d) are two images with reversed contrast of bright dots and dark dots, respectively. Their FT patterns look the same, as shown in Fig. 7.19(b) and (e), respectively. However, if one continues the IFT operation based on the FT patterns, the images appear as bright and dark dots again, as shown in Fig. 7.19(c) and (f), respectively. To identify the reason, it is needed

(a)

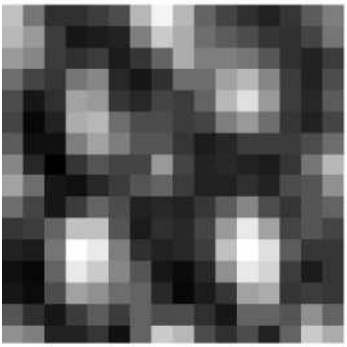

16×16 pixels

(b)

206	140	66	66	82	99	198	247	198	123	90	66	49	74	115	148
198	173	82	33	41	49	148	214	189	132	115	99	74	66	90	140
173	156	82	66	82	41	74	123	189	148	148	140	107	66	49	82
132	90	74	140	156	57	33	66	132	132	181	198	156	82	49	99
99	33	66	181	173	74	57	90	82	123	198	231	173	82	57	115
90	8	49	189	198	132	99	99	82	90	148	173	132	74	49	90
115	24	24	148	181	148	107	107	74	41	57	82	82	82	99	132
156	57	0	74	107	90	90	173	90	49	57	49	41	74	140	198
181	132	33	24	57	82	107	123	82	49	49	66	49	99	107	165
132	90	33	82	123	99	49	57	49	74	115	156	99	74	107	123
74	82	123	206	206	107	41	66	57	90	173	239	181	90	107	90
49	41	140	255	239	148	66	49	57	82	206	255	231	115	74	74
24	8	123	239	214	156	107	33	16	57	165	239	222	82	41	74
33	16	99	181	165	132	123	57	8	41	74	181	189	74	82	74
107	66	33	82	115	82	123	99	99	66	33	123	123	107	165	123
165	148	49	49	74	24	123	214	198	99	66	99	49	123	214	189

16×16 data

Fig. 7.17 (a) An image with 16 × 16 pixels; (b) intensity data of the image at each pixel.

to inspect the the complex data of the FT patterns. The complex number is expressed as $a + bi$ (Fig. 7.20), and its modulus (or absolute value) r and argument φ are

$$r = \sqrt{a^2 + b^2} \tag{7.33}$$

$$\varphi = \begin{cases} \arctan(b/a) & \text{if } a > 0 \\ \arctan(b/a) + \pi & \text{if } a < 0 \; and \; b \quad 0 \\ \arctan(b/a) - \pi & \text{if } a < 0 \; and \; b < 0 \\ \pi/2 & \text{if } a = 0 \; and \; b > 0 \\ -\pi/2 & \text{if } a = 0 \; and \; b < 0 \end{cases} \tag{7.34}$$

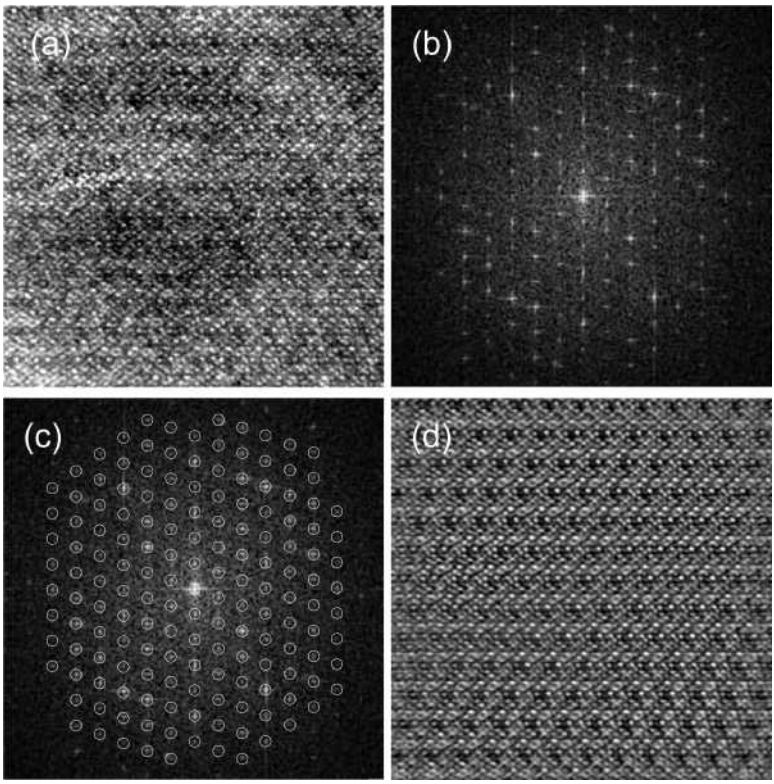

Fig. 7.18 Noise elimination by Fourier peak filtering. (a) HRTEM image; (b) FT pattern; (c) selection of spots for filtering; (d) IFT image.

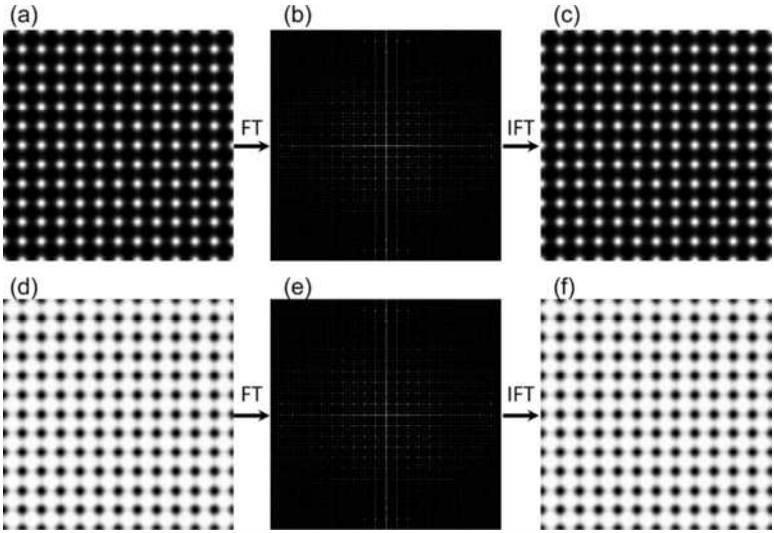

Fig. 7.19 White and dark spot images (a, d), their FT patterns (b, e), and their IFT images (c, f).

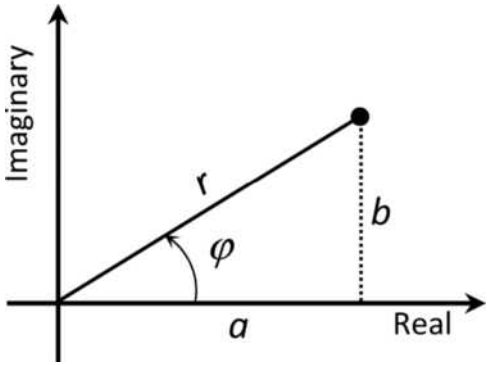

Fig. 7.20 A complex number a + bi.

The complex data of the FT patterns of the bright-dot and dark-dot images are shown in Fig. 7.21(a) and (b), respectively. It is found that their real and imaginary parts *a* and *b* have the same numbers but their signs are just reversed. Therefore, they have the same absolute values, but their arguments have a difference of π. Since the FT patterns in Fig. 7.19(b) and (e) display only the absolute values, or amplitude, they look

like the same, while their argument components, or phases, are reversed, which are not displayed on the pattern. The phase obtained from the FT can be used for the image processing [29].

(a)

C:\FFT of Image_bright

	C0	C1	C2	C3	C4	C5	C6
R0	258 + 0 i	-29.919657 0.70956111 i	-29.679585 1.4059963 i	-29.282578 2.0763078 i	-11.651421 -75.64006 i	-28.038155 3.2891016 i	-27.205229 3.8084946 i
R1	-29.865173 3.1380615 i	1.9942741 + -0.66209519	2.0106113 + -0.83515817	2.0303764 + -1.0111928	15.450909 + -42.003952	2.0762708 + -1.3779485	2.0996959 + -1.5710775
R2	-29.462105 6.255127 i	1.9504408 + -1.1488171	1.977065 + -1.3206915	2.007138 + -1.4952672	15.354254 + -39.637966	2.0734961 + -1.8582962	2.1069708 + -2.0491514
R3	-28.794916 9.3307495 i	1.87093 + -1.629498 i	1.9078226 + -1.7996759	1.9482728 + -1.9722962	15.326784 + -37.252495	2.0354869 + -2.3306603	2.0793324 + -2.5188096
R4	157.36328 + -321.41772	-22.550842 -16.00713 i	-23.290064 -16.984493	-24.058058 -17.791435	54.838516 + 145.80013 i	-25.61586 + -18.905788	-26.37491 + -19.223473
R5	-26.69817 + 15.277527 i	1.6075661 + -2.5619714	1.6646492 + -2.7272458	1.7257609 + -2.8944814	15.527924 + -32.468842	1.8552707 + -3.2407372	1.9205267 + -3.4222009
R6	-25.289852 18.111877 i	1.4257141 + -3.0085626	1.4925737 + -3.1706383	1.5638223 + -3.3344543	15.778488 + -30.09684 i	1.7144697 + -3.6732881	1.790615 + -3.8507838

(b)

D:\FFT of Image_dark

	C0	C1	C2	C3	C4	C5	C6
R0	-258 + 0 i	29.919657 + -0.70956111	29.679585 + -1.4059963	29.282578 + -2.0763078	11.651421 + 75.64006 i	28.038155 + -3.2891016	27.205229 + -3.8084946
R1	29.865173 + -3.1380615	-1.9942741 0.66209519	-2.0106113 0.83515817	-2.0303764 1.0111928 i	-15.450909 42.003952 i	-2.0762708 1.3779485 i	-2.0996959 1.5710775 i
R2	29.462105 + -6.255127 i	-1.9504408 1.1488171 i	-1.977065 + 1.3206915 i	-2.007138 + 1.4952672 i	-15.354254 39.637966 i	-2.0734961 1.8582962 i	-2.1069708 2.0491514 i
R3	28.794916 + -9.3307495	-1.87093 + 1.629498 i	-1.9078226 1.7996759 i	-1.9482728 1.9722962 i	-15.326784 37.252495 i	-2.0354869 2.3306603 i	-2.0793324 2.5188096 i
R4	-157.36328 321.41772 i	22.550842 + 16.00713 i	23.290064 + 16.984493 i	24.058058 + 17.791435 i	-54.838516 -145.80013	25.61586 + 18.905788 i	26.37491 + 19.223473 i
R5	26.69817 + -15.277527	-1.6075661 2.5619714 i	-1.6646492 2.7272458 i	-1.7257609 2.8944814 i	-15.527924 32.468842 i	-1.8552707 3.2407372 i	-1.9205267 3.4222009 i
R6	25.289852 + -18.111877	-1.4257141 3.0085626 i	-1.4925737 3.1706383 i	-1.5638223 3.3344543 i	-15.778488 30.09684 i	-1.7144697 3.6732881 i	-1.790615 + 3.8507838 i

Fig. 7.21 (a) FFT data of the bright-dot image in Fig. 7.19(b); (b) FFT data of the dark-dot image in Fig. 7.19(e).

References

[1]. S.J. Pennycook, S.D. Berger and R.J. Culbertson. Elemental mapping with elastically scattered electrons. *J. Microsc.* **144**, 229–249 (1986).

[2]. D.S. He, Z.Y. Li, J. Yuan. Kinematic HAADF-STEM image simulation of small nanoparticles. *Micron* **74**, 47–53 (2015).

[3]. P. Hartel, H. Rose, C. Dinges. Conditions and reasons for incoherent imaging in STEM. *Ultramicroscopy* **63**, 93–114 (1996).

[4]. Z.W. Wang, Z.Y. Li, S.J. Park, A. Abdela, D. Tang, R.E. Palmer. Quantitative Z-contrast imaging in the scanning transmission electron microscope with size-selected clusters. *Phys. Rev.* **B84**, 073408 (2011).

[5]. S.J. Pennycook. Z-contrast stem for materials science. *Ultramicroscopy* **30**, 58–69 (1998).

[6] D.B. Williams, C.B. Carter. Transmission Electron Microscopy: A Textbook for Materials Science. Springer, New York, 2009.

[7] A.V. Crewe, J. Wall. A scanning microscope with 5 Å resolution. *J. Mol. Biol.* **48**, 375–393 (1970).

[8] Z.P. Luo, Z.T. Wu, D.J. Miller. The dislocation microstructure of a nickel-base single-crystal superalloy after tensile fracture. *Mater. Sci. Eng.* **A354**, 358–368 (2003).

[9] A. Chen, H. Zhou, Z. Bi, Y. Zhu, Z. Luo, A. Bayraktaroglu, J. Phillips, E.-M. Choi, J.L. MacManus-Driscoll, S.J. Pennycook, J. Narayan, Q. Jia, X. Zhang, H. Wang. A new class of room-temperature multiferroic thin films with bismuth-based supercell structure. *Adv. Mater.* **25**, 1028–1032 (2013).

[10] J.C.H. Spence. *High-Resolution Electron Microscopy*. Fourth Edition. Oxford Press, Oxford, UK, 2013.

[11] D. Shindo, K. Hiraga. High-Resolution Electron Microscopy for Materials Science. Springer, Japan, Tokyo (2013).

[12] O. Scherzer. The theoretical resolution limit of the electron microscope. *J. Appl. Phys.* **20**, 20–29 (1949).

[13] Y. Zhu, J. Tafto. Direct imaging of charge modulation. *Phys. Rev. Lett.* **76**, 443–446 (1996).

[14] Y. Zhu, J. Tafto. A cluster description of structural modulation in $Bi_2Sr_2CaCu_2O_{8+\delta}$. *Philos. Mag.* **B75**, 785–791 (1997).

[15] H. Hashimoto, A. Kumao, K. Hino, H. Endoh, H. Yotsumoto, A. Ono. Visualization of single atoms in molecules and crystals by dark field electron microscopy. *J. Electron Microsc.* **22**, 123–134 (1973).

[16] S. Amelinckx, O. Milat1, G. Van Tendeloo. Selective imaging of sublattices in complex structures. *Ultramicroscopy* **51**, 90–108 (1993).

[17] T. Eguchi, Y. Tomokiyo, N. Kuwano. Configuration of anti-phase domains in one-dimensional long period superstructure alloys. *Trans. JIM* **24**, 369–377 (1983).

[18] H.W. Zandbergen, J. Jansen. Imaging of symmetry-forbidden fringes with $La_{1-x}Ca_xMnO_3$ as example. *Ultramicroscopy* **80**, 59–68 (1999).

[19] Z.P. Luo, H. Hashimoto, H. Ihara, A. Iyo, K. Tokiwa. Transmission electron microscopy characterization of the high-T_c superconductor $HgBa_2Ca_3Cu_4O_{10+\delta}$. *Philos. Mag. Lett.* **79**, 429–439 (1999).

[20] X.F. Zhang, Y.S. Sung, D.J. Miller, B.J. Hinds, R.J. McNeely, D.L. Studebaker, T.J. Marks. New structural aspects of $Tl_2Ba_2CaCu_2O_y$ epitaxial thin films grown by MOCVD on $LaAlO_3$. *Physica.* **C275**, 146–154 (1997).

[21] J.M. Cowley, A.F. Moodie. The scattering of electrons by atoms and crystals. I. A new theoretical approach. *Acta Cryst.* **10**, 609–619 (1957).

[22] J.M. Cowley, A.F. Moodie. The scattering of electrons by atoms and crystals. II. The effects of finite source size. *Acta Cryst.* **12**, 353–359 (1959).

[23] J.M. Cowley, A.F. Moodie. The scattering of electrons by atoms and crystals. III. Single-crystal diffraction patterns. *Acta Cryst.* **12**, 360–367 (1959).

[24] J.M. Cowley. *Diffraction Physics*. Third Edition. Elsevier, The Netherlands, 1995.

[25] Z.P. Luo, D.J. Miller, J.F. Mitchell. Electron microscopic evidence of charge-ordered bi-strip structures in the bilayered colossal magnetoresistive manganite $La_{2-2x}Sr_{1+2x}Mn_2O_7$. *Phys. Rev.* **B71**, 014418 (7 pp) (2005).

[26] H. Hashimoto. Physics of electron microscopy for atoms. *Electr. Microsc.* **17**, 41–54 (1982) (in Japanese).

[27] K. Izui, S. Furuno. Comment to the images of silicon in <110> orientation. *Ultramicroscopy* **21**, 399–402 (1987).

[28] F.H. Li. Crystallographic image processing approach to crystal structure determination. *J. Microsc.* **190**, 249–261 (1998).

[29] X.D. Zou, S. Hovmöller. Structure determination from HREM by crystallographic image processing. In: *Electron Crystallography: Novel Approaches for Structure Determination of Nanosized Materials*, edited by T.E. Weirich, J.L. Lábár, X.D. Zou. Springer, Netherlands, pp. 275–300 (2004).

CHAPTER 8

Elemental Analyses

For a complete material characterization using a transmission electron microscope (TEM), the information about the sample morphology, crystalline structure, and chemical composition is all needed. For example, to study particles or polycrystalline alloys, the particle or grain size, crystalline structure, and their component elements should be obtained from a TEM investigation. Unlike light microscopy (LM) or atomic force microscopy (AFM) that can provide only imaging, TEM can provide not only imaging and diffraction, but also chemical compositions. The elemental analyses are based on the interactions of high-energy electrons with core electrons of atoms in the specimen.

In the TEM, the elemental analyses are conducted using X-ray energy-dispersive spectroscopy (EDS) or electron energy-loss spectroscopy (EELS). Both EDS and EELS are based on the same events of the interactions of incident electrons with specimen atomic core electrons. However, the EDS uses only the generated X-ray signals (the signals are collected above the specimen), whereas the EELS uses the energy-loss signals of the transmitted electrons as a consequence of the interactions, and the EELS signals are collected as part of the transmitted electron beam well below the specimen.

A comparison of EDS and EELS is given in Table 8.1 [1–3]. Basically, EDS is more easy to use, especially the operation of EDS on TEM is similar to the EDS on a scanning electron microscope (SEM), whereas the EELS operation involves more procedures. However, EELS offers inherently higher spatial resolution than does EDS, and its collection time is normally shorter than EDS for thin specimens, especially in elemental mapping [3]. More information can be learned from the EELS studies, such as energy-loss near-edge structure (ELNES) and extended energy-loss fine structure (EXELFS), which can provide chemical state information. In addition, energy filtering can provide imaging and diffraction capabilities only by using

Table 8.1 Comparison of EDS and EELS

	EDS	EELS
Operation	Easy	Multiple procedures
Spatial resolution	Beam broadening	Good
Acquisition time	Long (for very thin samples)	Short
Sample requirement	Vary (thin for light elements)	Thin
Contamination sensitivity	No	Yes
Peak overlapping	Can be severe	No
Qualitative analysis	Yes	Yes
Quantitative analysis	Yes	Yes
S/N for light elements	Sufficient but relatively lower than heavy elements	High
S/N for heavy elements	High	Low
Energy resolution	Low (over 100 eV)	High (~1 eV)
Electronic structure information (ELNES, EXELFS)	No	Yes

zero-loss electrons to improve the image and diffraction quality, that is, the inelastically scattered electrons are excluded in the final image or diffraction pattern.

As listed in Table 8.1, the EDS can provide high signal-to-noise (S/N) level for heavy elements, while it is relatively lower for light elements. However, newer EDS systems can still provide sufficiently high signals to study the light elements. EELS, on the other hand, provides high S/N for light elements but lower for heavy elements. Generally, EDS can be used for both light and heavy elements, whereas EELS is mainly used for light elements.

The EELS requires thin specimens, whereas such a requirement is not critical for EDS, especially if no light elements are involved. For elemental analysis, a scanning TEM (STEM) mode is very helpful to provide a fine spot for both EDS and EELS analyses.

8.1 X-ray Energy-Dispersive Spectroscopy

8.1.1 Formation of Characteristic X-Rays

As mentioned in Section 1.2 in Volume 1, the high-energy electron beam strongly interacts with the specimen to generate a number of signals (refer to Fig. 1.2). Such interaction depends on the electron beam

energy, specimen composition, and thickness. Fig. 8.1 shows a comparison of interaction volume for a bulk specimen and a thin TEM specimen. For the bulk specimen in an SEM, electron probe microanalyzer (EPMA), or scanning Auger microscope (SAM), the interaction volume is very large, as shown in Fig. 8.1(a). Auger electrons come only from the specimen surface within few nanometers; secondary electrons, up to ~100 nm; and backscattered electrons, up to 1–2 μm. The characteristic X-rays, along with continuum and fluorescent (secondary) X-rays, come from deeper regions, typically 2–5 μm. Therefore, the spatial resolution of EDS of such bulk specimens is very limited. This is due to the fact that, although the electron beam is focused only on the interested area in the view, the X-rays are indeed from deeper regions underneath it. However, in a TEM thin specimen with thickness normally less than 100 nm, the interaction volume is limited, as shown in Fig. 8.1(b). Therefore, the spatial resolution in TEM is much higher than SEM/EPMA/SAM using the bulk specimens.

An EDS spectrum includes continuum (background) and characteristic X-rays (peaks). When the incident electrons pass nearby the nuclei, they are slowed down by the strong Coulomb field, and therefore X-rays are released. These X-rays have varied energies without specific characteristic peaks, contributing to the background of the EDS spectrum. They are termed as continuum X-rays, or Bremsstrahlung X-rays.

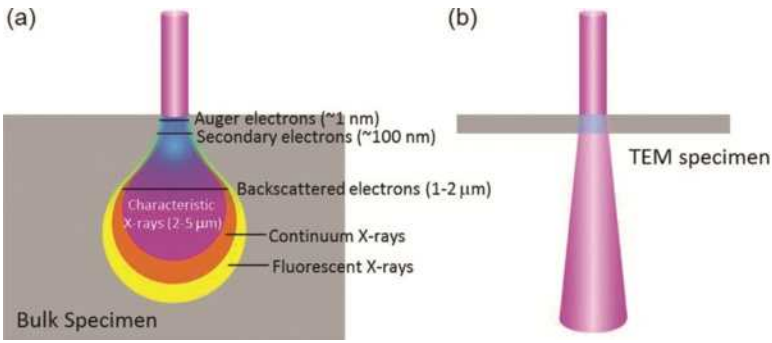

Fig. 8.1 Interaction volume of electron beam with specimen. (a) Bulk specimen (in SEM or EPMA); (b) TEM thin specimen.

Another type of X-rays is characteristic X-rays, with peak energies correspond to specific elements. They are formed by the interactions with core electrons. If inner shell electrons are ejected by the incident electrons, electrons from outer shell fill the vacancies, and thus X-rays are released to lower down the system energy. The X-ray energy equals to the energy difference of these two orbital energies, and thus the X-rays are elemental specific.

Fig. 8.2(a) illustrates the electronic structures, including the first (K), second (L), third (M), and fourth (N) shells. The principal quantum number n, azimuthal quantum number l, total angular momentum quantum number j, and outer shell electron configurations are shown on the right side of Fig. 8.2(a). If an electron in the K shell is ejected, an electron on the L_3 or L_2 may fill it, producing K_{α_1} or K_{α_2} X-ray lines, respectively. However, if it is filled by M_3 or M_2 electrons, K_{β_1} or K_{β_2} lines are resulted. Similarly, other L and M lines are defined from other shells as illustrated. In the EDS spectrum, because of the limited energy resolution (over 100 eV), peaks with small energy difference overlap together. For example, K_{α_1} and K_{α_2} overlap to form a single K_α peak. Therefore, in EDS, the peaks are simply represented in Fig. 8.2(b).

8.1.2 EDS Detector

The EDS detector is installed physically close to the TEM specimen to collect the X-rays, nearby the upper pole piece of the objective lens (for this reason, check if the detector affects the astigmatism of HRTEM images and retract it slightly as needed), as shown in Fig. 8.3(a). The EDS detector normally locates on the right side of the specimen holder and at an angle perpendicular to it, as shown in the photo of Fig. 8.3(b). However, it can also be installed on the left side of the specimen holder at other angles, depending on the port location on the TEM.

There are several important factors with an EDS detector:

1. Collection angle Ω, which is related to the active area S. The higher Ω, or the larger S, more X-rays can be collected.

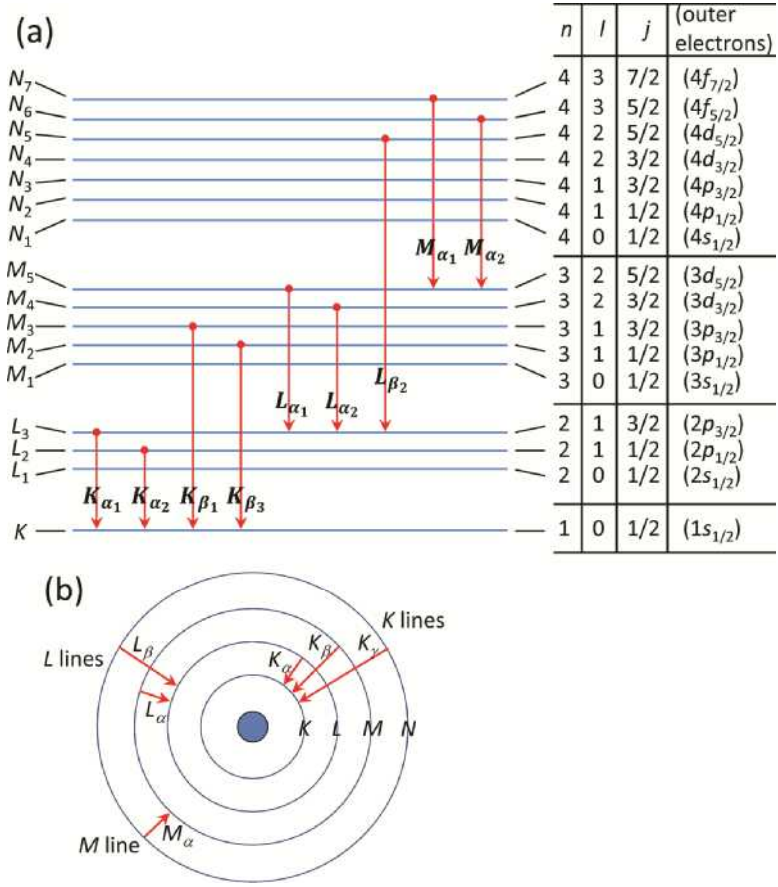

n	l	j	(outer electrons)
4	3	7/2	($4f_{7/2}$)
4	3	5/2	($4f_{5/2}$)
4	2	5/2	($4d_{5/2}$)
4	2	3/2	($4d_{3/2}$)
4	1	3/2	($4p_{3/2}$)
4	1	1/2	($4p_{1/2}$)
4	0	1/2	($4s_{1/2}$)
3	2	5/2	($3d_{5/2}$)
3	2	3/2	($3d_{3/2}$)
3	1	3/2	($3p_{3/2}$)
3	1	1/2	($3p_{1/2}$)
3	0	1/2	($3s_{1/2}$)
2	1	3/2	($2p_{3/2}$)
2	1	1/2	($2p_{1/2}$)
2	0	1/2	($2s_{1/2}$)
1	0	1/2	($1s_{1/2}$)

Fig. 8.2 (a) Electronic structure of atoms illustrating the formation of characteristic X-rays between different energy levels; (b) simplified diagram showing the characteristic X-ray lines in EDS.

2. Take-off angle α, which is the angle between the specimen surface at zero tilt and the line to the center of the detector. Some EDS detectors require a sample tilt at 20–25° facing toward the detector, while some can collect signals at zero tilt.
3. Detector window. Old detectors with beryllium (Be) windows very restrict the detection of light elements. Elements below Na cannot be detected. The type of ultrathin window (UTW) or newer atmospheric thin window (ATW), made of polymer or polymer-based composites, enables the detection of light elements. However, carbon-containing

windows absorb N K_α lines strongly. Windowless detectors do not use any window materials (nothing on the window), so high vacuum level is required. During the sample exchange, the windowless detector should be retracted and uncooled to avoid any contaminations on it.

The mostly used EDS detectors are probably Si(Li) detectors and newly developed silicon drift detectors (SDDs). The structure of the Si(Li) detector is schematically shown in Fig. 8.3(c). The X-rays penetrate the window (which keeps vacuum) and Au contact to enter the Si–Li crystal, generating pairs of positive holes and negative electrons. The number of electrons/holes is proportional to the X-ray energy. Since a high-voltage bias is applied, the holes and electrons are separated, and the charge pulse of electrons is detected by a field-effect transistor (FET). The FET must be constantly cooled by liquid nitrogen if it is at work.

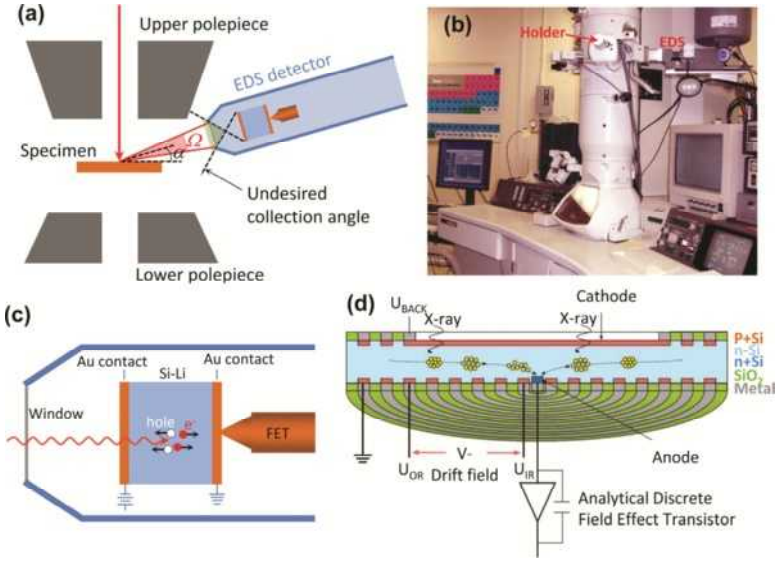

Fig. 8.3 (a) EDS detector configuration in TEM; (b) a TEM with EDS installed on the right side of the specimen holder; (c) schematic construction of the Si(Li) EDS detector; (d) SDD detector (courtesy of Oxford Instruments [4]).

The structure of SDD is schematically shown in Fig. 8.3(d) [4]. It is fabricated from high-purity silicon with a large area contact on the entrance side. The incident X-rays generate holes and electrons. In the SDD, the positive holes move to the electrodes, while negative electrons drift to the anode. The electron charge is again proportional to the energy of the X-rays. Unlike a Si(Li) detector, as the size of the anode on an SDD is small, it does not require liquid nitrogen cooling. SDDs have larger solid angles and active areas than Si(Li) detectors, with a somewhat better energy resolution with few eV's.

Note that both Si(Li) and SDD can detect light elements, and the element B can routinely be detected even in the SEM [5]. Therefore, EDS is an effective way to quickly characterize materials. Some investigators are even used to do the EDS first to ensure the correct composition, before doing anything else on the TEM.

8.1.3 EDS Artifacts

Although the EDS operation is pretty much easy, and even a beginner can learn it quickly, there are a lot of possible reasons leading to spurious EDS signals, either extra signals (additional elemental peaks or some intensified peaks) or reduced signals (reduced or disappeared peaks for light elements).

The most common spurious signals are some extra signals from areas nearby the testing spot, such as grid bar, grid washer, securing screw, specimen holder, microscope pole piece, or even the EDS system itself. As shown in Fig. 8.4(a), the incident electrons on the specimen can be scattered in different directions. If the transmitted electrons are scattered to the lower pole piece of the objective lens, or the backscattered electrons from the specimen to the upper pole piece, characteristic X-rays of the TEM system (Fe and Co) are generated. If the electrons are backscattered from the upper or lower pole pieces to the specimen, characteristic X-rays are generated from the specimen but from other areas. Similarly on same samples, the electrons can be scattered to nearby areas to form spurious X-rays from the surroundings.

Apart from the spurious signals generated by the scattered electrons, fluorescent X-rays can cause spurious signals as well. The primary X-rays, such as the continuum or characteristic X-rays generated by the

interaction of electron beam with the specimen, can also interact with other materials. As a consequence, fluorescent (or secondary) X-rays are generated. These fluorescent X-rays are spurious signals. As shown in Fig. 8.4(b), the analyzing particle is on the top of carbon support film on a piece of Cu grids. The X-rays from the sample generated by the electron beam scatter to various directions (in fact, only a small part of the primary X-rays are collected by the EDS detector). These primary X-rays may interact with the particles nearby, the Cu grids bar, and even the specimen holder if its edge is near the beam (well off the center), and thus fluorescent X-rays from these interacted areas are formed. It is very common to get the signals from the support grids.

It should be mentioned that even inside the EDS detector crystal, fluorescent X-rays can happen. When the incoming X-rays inadvertently knock out the Si *K*-shell electrons in the detector crystal, upon filling these vacancies, Si K_α peak (1.74 keV) appears, which is from the internal

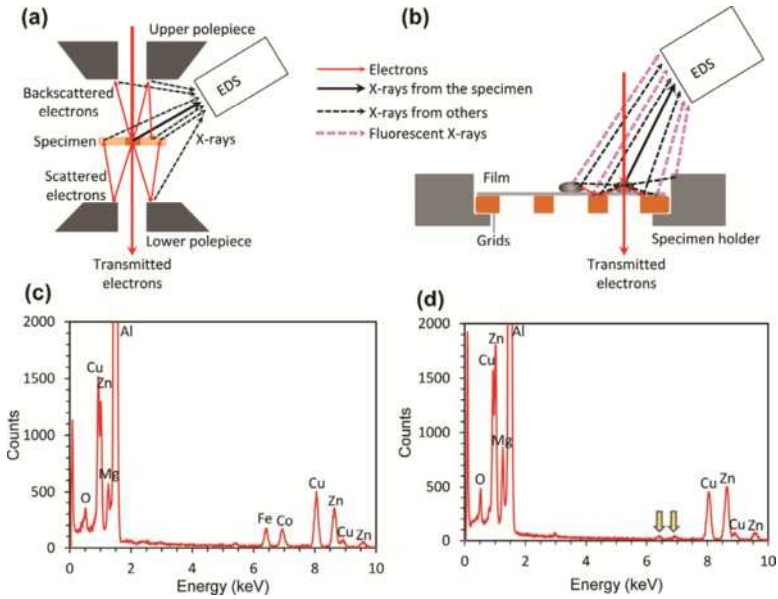

Fig. 8.4 Spurious X-ray signals generated in TEM. (a) X-ray signals generated by scattered electrons; (b) fluorescent (secondary) X-rays generated by X-rays from the sample. Solid lines represent electrons, and broken lines, various X-rays. An example of Fe/Co spurious signals from the TEM pole piece is shown in (c), and such spurious signals are reduced after tiling the sample holder toward the detector (d).

fluorescence in the Si-based detector. As a consequence, those X-rays that knocked out the detector Si electrons have their energies reduced by 1.74 keV. Therefore, a small peak appears in the front side of the major peak with 1.74 keV lower energy, which is called as the escape peak. For example, if the major peak is Cr K_α at 5.41 keV, a small peak at 3.67 keV (= 5.41 – 1.74 keV) appears, which is the escape peak of Cr K_α. Precautions should be taken for not labeling the escape peak as a characteristic peak of an element.

Fig. 8.4(c) shows an EDS spectrum from an Al–Mg–Zn alloy taken from a newly installed EDS detector at zero specimen tilt (installation was not completed). It exhibits evident Fe and Co elements from the TEM pole piece, since the specimen does not contain Fe and Co. After tilting the specimen for 20° toward the detector, the spurious signals of Fe and Co are significantly reduced, as shown in Fig. 8.4(d). These two spectra have different Cu/Zn ratios because the beam spot moved after tilting. Normally a well-installed EDS detector should not contain evidence spurious signals from the pole pieces.

8.1.4 Effects of Specimen Thickness, Tilt, and Space Location

The EDS spectra depend on the specimen thickness, tilt, and the location of the testing point with respect to the detector. As shown in Fig. 8.5(a), for a thin specimen, because of the limited interaction volume, the X-rays are not intense. The X-rays generated inside the specimen have a short absorption distance as they travel toward the detector. For a thick specimen, as shown in Fig. 8.5(b), because of the large interaction volume, the X-rays are intense. The X-rays at a greater depth have thus a longer absorption distance within the specimen. Consequently, X-rays with lower energies could be absorbed more strongly. If a thick sample contains light elements, such as C, N, or O, they will appear at lower intensities or even disappear due to the strong absorption. In addition, precautions should be taken for not working on the too thick samples to produce too high counts, as shown by the dead time of the detector. The dead time is the period during which the detector receives X-ray photons but is busy and cannot accept/process the pulses.

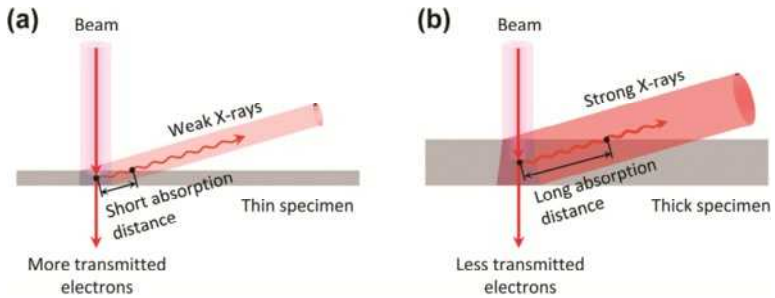

Fig. 8.5 Effect of TEM specimen thickness of the X-ray signals. (a) Thin specimen; (b) thick specimen.

The dead time should be controlled below 50%. If the counts are too high, the detector shutter will automatically close or the detector will be automatically retracted, as a protection on the detector from too intense X-ray exposure, which may damage it.

The sample tilt may affect the EDS spectra. Nowadays most EDS detectors can collect signals at the specimen zero tilt, as shown in Fig. 8.6(a), which is convenient for doing EDS without tilting. The sample can be tilted toward to the detector, as shown in Fig. 8.6(b). The tilting direction can be verified by looking at the outside of the specimen holder to ensure it is facing to the detector (the holder stage is shown in the photo of Fig. 8.3b). In this case, if it is a bulk sample, more interaction volume becomes larger, which can result in higher counts but with shorter absorption distance; if, however, it is a single spherical particle sample, the interaction volume and absorption distance may stay the same. However, if the specimen is tilted toward the opposite side of the detector, as shown in Fig. 8.6(d), a much longer absorption distance results, and if it is tilted to higher degree, the X-rays have to penetrate the sample to reach the detector on the other side. If the TEM specimen is a bulk sample, most probably no X-rays can be detected because of the long distance to penetrate, and if it is a piece of TEM grid, strong spurious signals from the grid bar would be obtained.

The sample location in the space with respect to the detector also impacts on the EDS spectra. As depicted in Fig. 8.7(a), if the thick side faces to the detector, the X-rays travel a long distance inside the specimen, whereas if the thin side faces to the detector, as shown in Fig. 8.7(b), the absorption distance is shorter. Note that the thicknesses at the detecting

points are the same in Fig. 8.7(a) and (b), but the spectra can be different, depending on the detector orientation. Sometimes the same sample, when it is taken out and installed back, could generate different types of EDS spectra, just because of the different orientation with respect to the detector. Therefore, the user should have a clear mind about the EDS detector location.

How to figure out the EDS detector location is demonstrated in Fig. 8.8. Spectra in Fig. 8.8(a) and (b) are taken from the two edges of spherical particles at locations A and B, respectively. They are the same

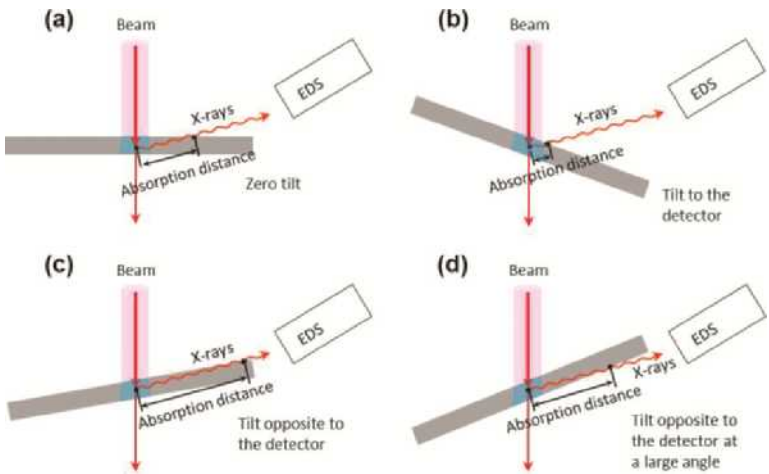

***Fig. 8.6** Effect of specimen tilt on the EDS signals. (a) Zero tilt; (b) tilt facing to the detector; (c) tilt opposite to the detector for a small angle; (d) tilt opposite to the detector for a large angle so that X-rays have to penetrate the specimen to reach the detector.*

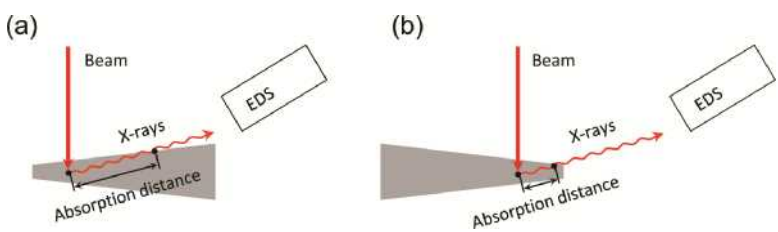

***Fig. 8.7** Effect of orientation of uneven TEM specimen on the X-ray signals. (a) Thick side facing the EDS detector; (b) thin side facing the EDS detector.*

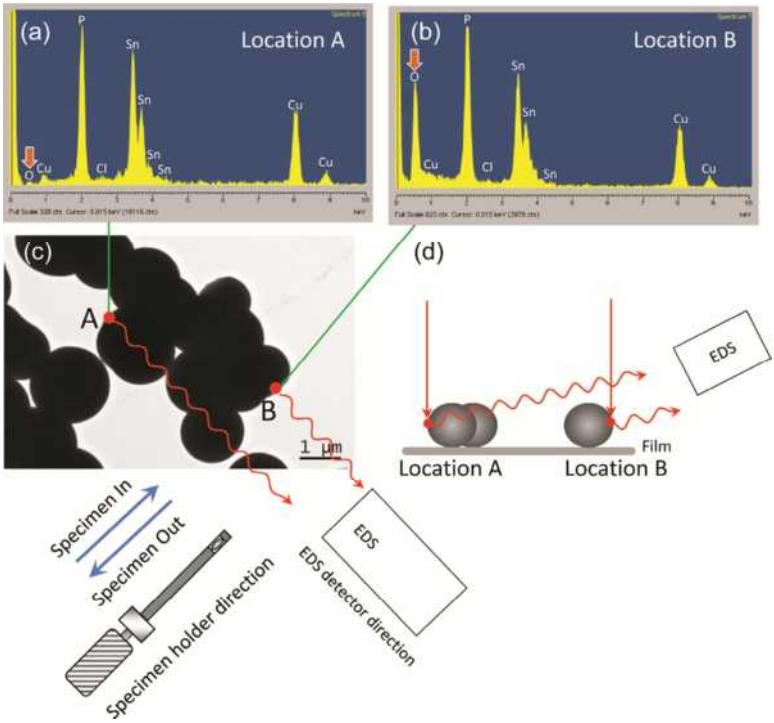

Fig. 8.8 Example of the effect of specimen location on the X-ray signals. (a, b) EDS spectra from locations A and B, respectively, in the image in (c); (d) schematic space locations. The EDS detector orientation can be found by moving the specimen holder slightly, as indicated below the image in (c). Arrows in (a) and (b) indicate the different O peak heights from locations A and B with the same compositions.

type of particles with almost the same size, while spectrum in Fig. 8.8(a) exhibits very low-oxygen peak, and spectrum in Fig. 8.8(b) exhibits normal oxygen peak, as indicated with arrows. To identify the reason, it is necessary to find out the detector orientation. The experiment was done using the TEM/EDS shown in Fig. 8.3(b), and the EDS detector locates on the right side of the specimen holder. The specimen holder direction can be found by slightly retracting it and then inserting it, and the image moving direction during inserting is thus the holder direction. It was found that during inserting the specimen holder, the image moved along from lower-left to upper-right direction, as indicated below Fig. 8.8(c), and thus the EDS located on the right side of the holder at an angle of 90°. It is evident that spot B is in the front of the detector,

so that X-rays directly reach it, while spot A is at the backside of the particle, so that the X-rays have to travel through the particles to reach the detector, as shown in Fig. 8.8(d). Therefore, the low-energy oxygen X-rays are greatly absorbed during traveling. Other peaks could also be absorbed, such as P showing relatively lower P/Sn ratio compared with the spectrum in Fig. 8.8(b).

8.1.5 Experimental Procedures

To collect EDS data correctly, the following precautions should be taken:

1. Select thinner specimen for EDS, especially for light-element analysis (if the sample is too thin, the counts will not be sufficient). If it is a wedge-shaped sample or particle, check the detector location to ensure the thinner side faces to the detector.
2. Use EDS mode (refer to Fig. 6.7) to get a small spot on the specimen, or use STEM mode if available, to reduce the electron beam size. Focus the image and ensure the spot is on the interested area.
3. Check the detector configuration and use zero tilt or tilt 20–25° toward the detector, but never tilt the specimen to the opposite side to the detector.
4. Control the beam intensity to ensure the dead time is less than 50%. For quantitative analysis, collect for a sufficiently long period (in several minutes) to get enough counts (over several thousands) for higher accuracy.
5. After the EDS collection, check if the sample is still at the same location without drifting. If it is drifted, the collected spectrum is not exactly from the original spot.
6. To collect EDS, never use the regular objective aperture, which generates too high X-ray counts. If the aperture is inserted, strong X-rays are produced from the aperture since it is a bulk sample; it also backscatters electrons to the specimen to produce spurious signals from other areas. The high-contrast aperture may be used, if it does not change the counts significantly.

8.1.6 *EDS Applications*

The EDS can be used for qualitative and quantitative analyses to identify and quantify the elements in the specimen. The data collection can be done in different ways, such as by point analysis, line scan, or elemental mapping. The line scan and mapping should be done in the STEM mode.

(a) Qualitative Analysis

When an EDS spectrum is acquired, qualitative analysis can be done quickly using the EDS program of the instrument. Possible spurious signals could be avoided or reduced by using the following measures:

1. Work near the center of the stage position, or use Be stage (the sample area is made of Be which cannot be detected by most of the EDS systems), to minimize signals from the sample holder.
2. Work near the center of the grid to minimize the signals from the grid bars.
3. Tilt the specimen toward the EDS detector for 20–25° to minimize the signals from the TEM pole pieces (Fe and Co).
4. Check the sample locations to avoid X-ray pathways from surrounding areas (refer to Fig. 8.8). In most case, tilting toward the EDS detector for 20–25° is helpful to get signals from the target only.
5. If peaks are overlapped, try to change the process time to improve the peak resolution (sharpen the peak), or energy range to check other peaks.

The EDS spectrum in Fig. 8.9(a) was taken from Pt–Co–W nanoparticles (NPs) with low W concentration (3.8 at.%). The positions of W *M* lines (left side) and *L* lines (right side) are indicated. The W L_{α_1} is at 8.396 keV [6], which partially overlaps with Cu K_{α_1} at 8.046 keV and K_{α_2} at 8.026 keV; W L_{β_1} is at 9.671 keV, which partially overlaps with Pt L_{α_1} at 9.441 keV and L_{α_2} at 9.360 keV. The overlaps make Cu $K\alpha$ (K_{α_1} and K_{α_2}) and Pt L_α (L_{α_1} and L_{α_2}) peaks evidently nonsymmetrical with a small shoulder on their right sides, as indicated by two arrows.

At the lower energy range, as magnified in the inset, isolated W M_α peak appears (M_{α_1} is at 1.775 keV and M_{α_2} is at 1.773 keV), indicating the presence of W. The EDS spectrum in Fig. 8.9(b) was taken from Pt–Ni–Fe NPs without W. The W peak positions are still indicated for comparison. The Pt peak is symmetrical without a shoulder on its right. At the lower energy range (inset), a Si K_α appears at 1.739 keV, which is symmetrical indicating no overlap with W M_α peak. To identify the presence of an element, it is necessary to check with different peaks and peak symmetry for any possible peak overlaps.

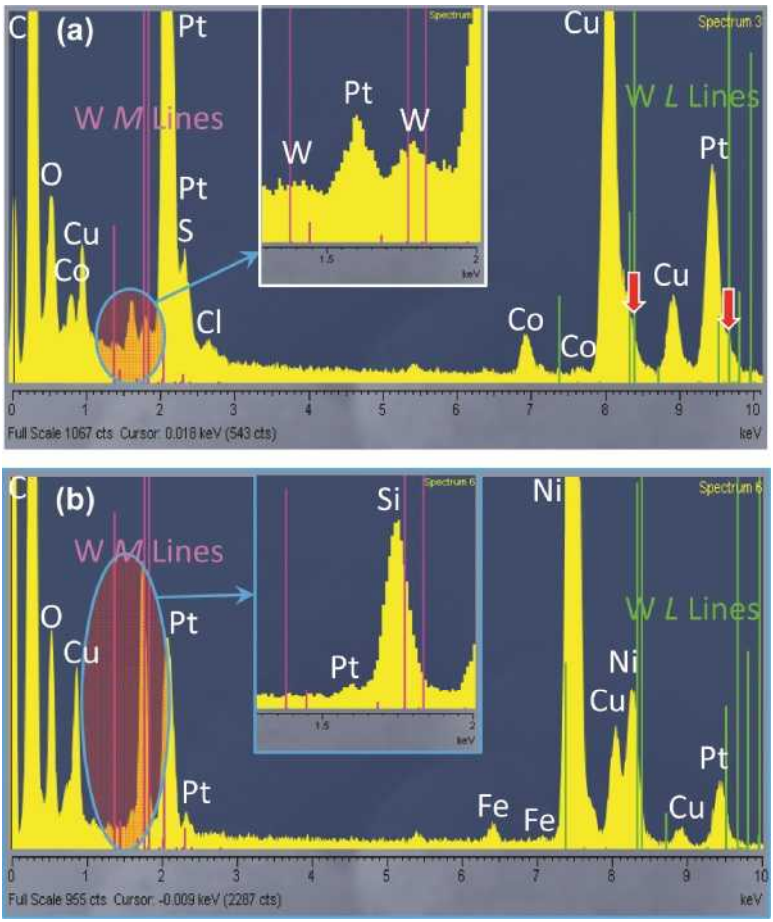

Fig. 8.9 Qualitative analyses of samples with W (a) and without W (b).

(b) Quantitative Analysis

In a bulk sample, such as a sample for SEM or EPMA analysis, the content ratio:

$$\frac{C_A}{C_S} = K\frac{I_A}{I_S} \tag{8.1}$$

where C_A (unknown) and C_S (known) are the weight concentrations of element A in the sample and standards, respectively, and I_A and I_S are the intensities of the same line peaks from the sample and standard, respectively. The K is a sensitivity factor [7], which is not a constant but related to:

1. Z: atomic number;
2. A: absorption of X-rays with the specimen; and
3. F: fluorescence of X-rays within the specimen.

In the bulk-sample analysis, the ZAF correction of K is conducted considering the above three factors.

However, for a thin TEM specimen, the factors A and F can be ignored. If the sample contains A and B elements with weight concentrations C_A and C_B, respectively,

$$\frac{C_A}{C_B} = k_{AB}\frac{I_A}{I_B} \tag{8.2}$$

where I_A and I_B are the intensities of a characteristic peak above the background which can be measured experimentally. The factor k_{AB} is termed as Cliff–Lorimer (C–L) factor [8], which is not a constant but related to the kV and atomic number Z. It can be obtained by using a common standard such as Si,

$$k_{AB} = \frac{k_{ASi}}{k_{BSi}} \tag{8.3}$$

Here, k_{ASi} and k_{BSi} are C–L factors of elements A and B to Si, respectively, which are already determined and stored in the computer program by the EDS manufacturer. By assuming

$$C_A + C_B = 1 \tag{8.4}$$

It is possible to obtain C_A and C_B using Eqs. 8.2 and 8.4. A system with more elements can be quantified similarly.

This quantification using given k factors is standardless analysis. If the user conducts measurements using a standard with accurately known compositions, it is needed to calibrate the k_{AB} factor using Eq. 8.2.

In practice, the standardless quantification can already provide sufficiently accurate results. The following precautions should be made:

1. Select thin areas for data collection to avoid the effects from A (absorption) and F (fluorescence).
2. Ensure the thinner area is facing physically to the EDS detector (refer to Fig. 8.7).
3. Collect sufficient counts, at least 1,000 for the select peak. Normally it takes several minutes to get sufficient counts at thin areas, so ensure there is no sample drift during the data collection.
4. If the sample is at a two-beam condition, slight tilt it off the strong dynamical diffraction to avoid any possible channeling effect.

Using a modem EDS detector and updated software, it is routinely possible to achieve 2 wt.% accuracy for heavy elements, or 5 wt.% accuracy for light elements. However, if the sample is thick or inappropriately oriented, such as in the example of Fig. 8.8, huge error could be resulted for the light elements.

Fig. 8.10 shows an example of EDS spectrum taken from Pt–Cu NPs (refer to the supporting document of reference [9]). The specimen was thin (dispersed NP), and the spectrum full scale showing Pt is at 1,829 counts. Since the sample contains Cu, Ni grid was used to avoid signals from the grid. Standardless quantification was done using Pt L_α and Cu K_α lines. Up to six spectra were collected from different thin areas, and the quantification results are listed in Table 8.2. These results are very close to each other with very low standard deviation, and the mean results are close the stoichiometry of Pt_3Cu.

Table 8.2 Quantification Results of Pt–Cu nanoparticles (at.%).

Spectrum	Cu	Pt
Spectrum 1	33.15	66.85
Spectrum 2	34.68	65.32
Spectrum 3	33.83	66.17
Spectrum 4	32.16	67.84
Spectrum 5	33.41	66.59
Spectrum 6	32.80	67.20
Mean	33.34	66.66
Std. deviation	0.87	0.87

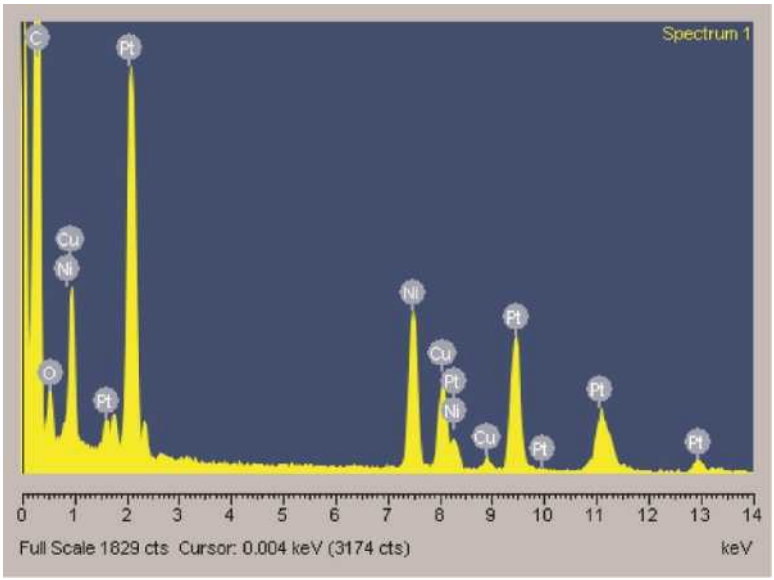

Fig. 8.10 EDS spectrum of Pt–Cu sample for quantitative analysis. The signals of Ni are from the grid used.

(c) Point Measurement

Although point analysis can be done in the TEM mode using a small spot, preference is given to the EDS mode or STEM mode. Fig. 8.11 illustrates the point analysis of Bi–Sn eutectic nanowires [10]. Two nanowires exhibit alternating segments in darker and lighter contrast. The EDS spectra (left side) are taken from the indicated areas using TEM EDS mode. It is found that the darker area belongs to Bi, and the lighter area belongs to Sn. The image contrast here is the scattering absorption contrast, since the heavier

element scatters electrons at larger angles that are filtered out by the objective aperture, and thus it shows the darker contrast. Further, the selected-area electron diffraction (SAED) patterns from the segments, as shown in the bottom side of the figure, reveal that within the segments, the Bi and the Sn are single crystals. Note that the EDS spectrum from the Sn region contains evident Bi signal, indicating a solid solution of Bi in Sn, which is consistent with the Bi–Sn phase diagram, while the very faint Sn signal in the EDS spectrum from the Bi region may be caused by spurious X-rays from the nearby Bi areas during the EDS acquisition. The signals of Al, O, and P are from the surface residuals of template and reactants, and Cu is from the grid bar of the TEM specimen.

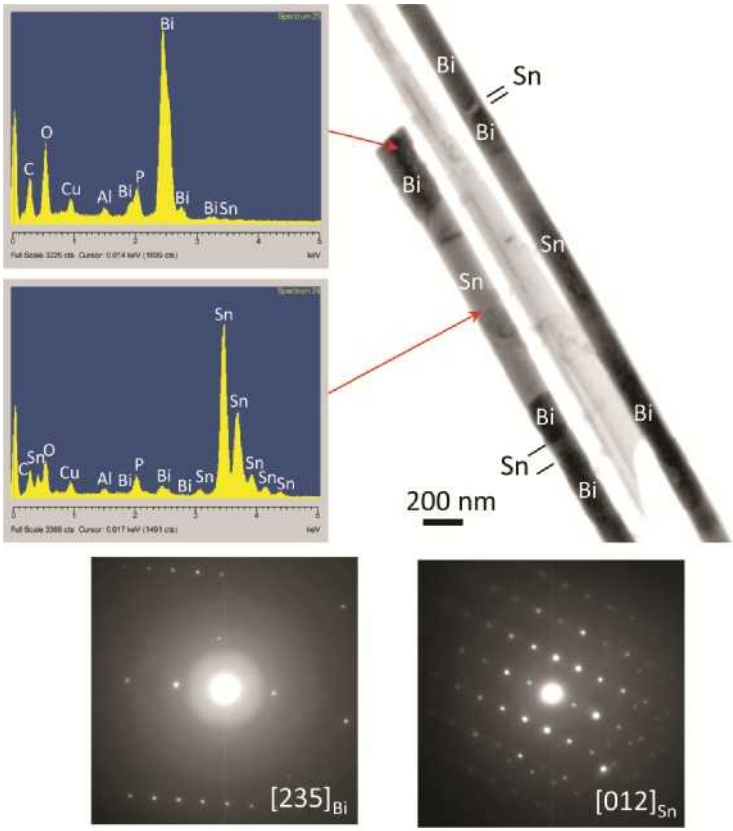

Fig. 8.11 EDS analyses of Bi–Sn eutectic nanowires. The EDS spectra on the left side are collected from Bi and Sn using TEM EDS mode.

To identify small objects at nanometer scale, STEM is required. Fig. 8.12(a) is a STEM image of In_2O_3–Pd binary NP superlattices (BNSL) [11], taken using a spot size of 1 nm. The large NPs have average side of 16 nm, and smaller ones, 6 nm. Two NPs, labeled as "b" and "c", respectively, are selected for the EDS analysis in the STEM mode. Despite the elements induced by the chemicals during the sample preparation as well as Cu signals from the grid, the EDS spectrum from the large particle presents In and O signals without Pd (Fig. 8.12b), whereas that from the small particle shows the evidence of Pd (Fig. 8.12c), although spurious In signals from the surrounding large particles are also present (hard to avoid). The EDS analysis is consistent with the assumption that the large NPs are In_2O_3 and small NPs are Pd.

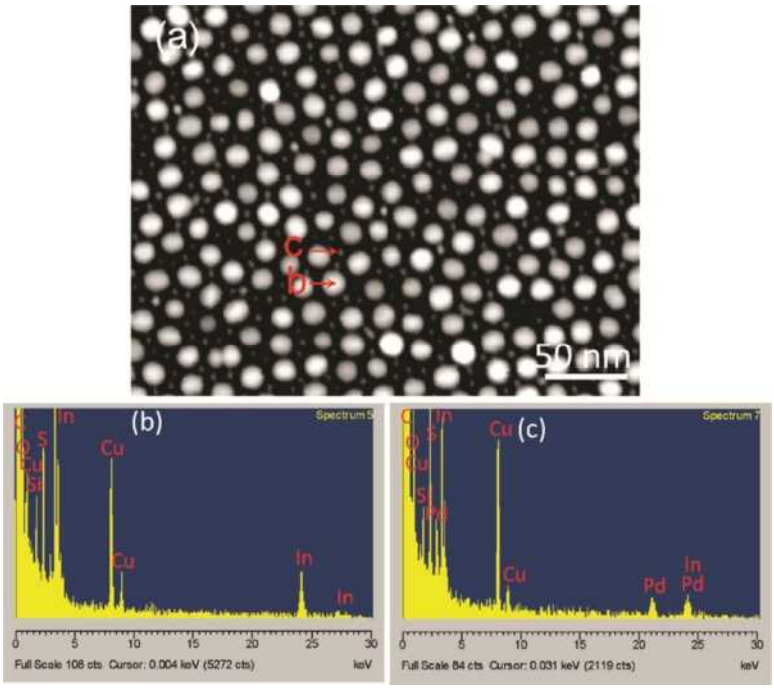

Fig. 8.12 (a) STEM image containing large In_2O_3 and small Pd and NPs; (b) EDS from a large NP labeled as "b" in (a); (c) EDS from a small NP "c" in (a).

(d) Line Scan

A line scan should be done in the STEM mode. First, define a line direction and size of the line, say 120 points. During the beam scanning, the EDS spectrum is collected at each spot, and thus the profiles along the line are obtained. The profile can be intensity of peaks, or atomic or weight concentrations.

Fig. 8.13(a) is a STEM image showing the presence of B_4C and Al [5]. A magnified part from the framed area in Fig. 8.13(a) is shown in Fig. 8.13(b). A line scan crossing the interface is performed in the STEM mode to collect the EDS composition profiles, as shown in Fig. 8.13(c). No indication of any reactant phases is found at the interface. In Fig. 8.13(d), a border of AlB_{10} and B_4C is illustrated. An EDS line scan is performed crossing $AlB_{10}/B_4C/Al$ phases to reveal the composition profiles, as shown in Fig. 8.13(e). It is evident that the AlB_{10} region contains Al, B, and C, whereas in the B_4C region, Al intensity is low, and B and C intensities are a little higher. When the line scan reaches the Al grain, high Al counts are encountered while B and C counts become very low. Such line scan can provide composition profiles to identify different particles or phases.

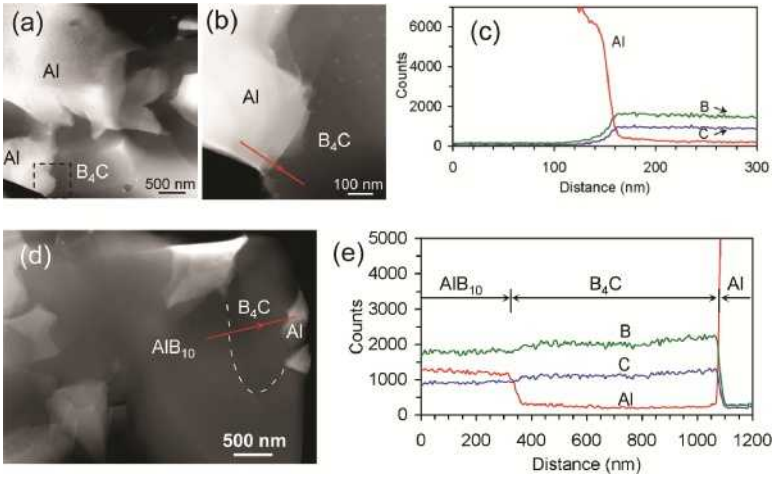

Fig. 8.13 EDS line scan. (a) STEM image of B_4C–Al interface; (b) enlarged from the framed area in (a); (c) EDS line scan profile from the line position shown in (b); (d) STEM image showing AlB_{10}–B_4C–Al interfaces; (e) EDS line scan profile crossing the AlB_{10}–B_4C–Al interfaces.

(e) Mapping

The EDS elemental mapping should be done in the STEM mode, which can provide 2D compositional distribution, instead of 1D profile by the line scan. At first, a 2D scanning area is defined, say 120 × 100 spots. Then the beam scans spot by spot (120 spots in a line, and 100 lines to complete the area). It takes much longer time for mapping than spot or line scans. Usually the sample drifting is a problem during the long-time data collection. Some programs offer drift collections by selecting a small reference area in a high contract, so that after some defined period of time, for example, after each line, an image of the reference area is taken and any found drift is thus corrected.

Fig. 8.14 shows an EDS mapping example of Bi–Sn nanowires [10]. The elemental mapping was done in the STEM mode, with drift correction performed. A STEM image of nanowires is shown in Fig. 8.14(a). An area is selected to map Bi and Sn elements, as shown in the magnified STEM image along with two elemental maps of Bi and Sn in Fig. 8.14(b). It is evident that the alternating segments within the wires are Bi and Sn elements only. The elemental mapping can provide elemental distributions directly, although it takes longer time to collect the data.

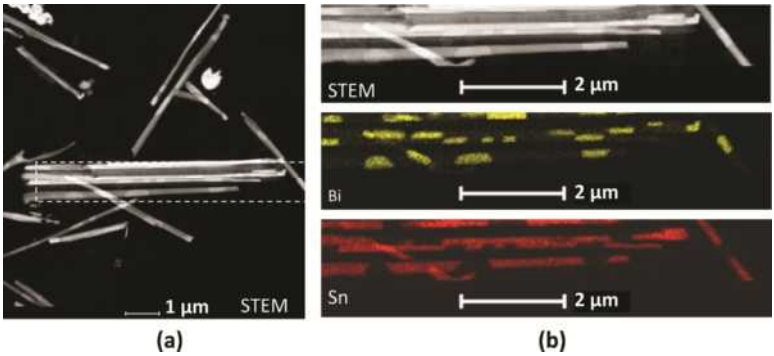

Fig. 8.14 (a) STEM image of Bi–Sn eutectic nanowire; (b) enlargement of the framed area in (a) along with the EDS elemental maps Bi and Sn.

8.2 Electron Energy-Loss Spectroscopy

8.2.1 Formation of EELS

The EELS signals come from the interaction of incident electrons with specimen atoms. If the incident electrons interact with specimen atoms and knock out their core electrons, continuum or characteristic X-rays are generated when outer-shell electrons fill these vacancies. However, these incident electrons lose a certain amount of energy, that is, their energy was transferred to the X-rays or in other forms during the interaction (refer to Fig. 1.2 in Volume 1). These transmitted electrons are collected and their energies are analyzed by EELS. Similar to the formation of EDS signals, the energy-loss edges in EELS spectra are related to the electronic structure of the atoms, as shown in Fig. 8.2. The EELS edges are specified using the subshells of the notations on the left side of Fig. 8.2(a). Since the energy loss is elemental specific, it is possible to identify the element using EELS spectra.

The energy losses of transmitted electrons are detected using magnetic lens. As illustrated in Fig. 8.15(a), the transmitted electrons pass through an entrance aperture to enter the magnetic lens, where the charged electrons are deflected in the magnetic field. Those electrons with lower energies are deflected at larger angles; hence, when they arrive at the dispersion plane, they move to the upper position compared with those electrons retaining initial energy E_0 without energy loss. Thus, electrons with different energy losses are dispersed. The higher the energy loss, the further distance from the zero-loss peak (ZLP) with energy E_0. The separation of electron energies with a magnetic prism is similar to an optical glass prism, which can separate a white light into different colors, as shown in Fig. 8.15(b). However, in the case of the glass prism, the light with higher energy (violet) deflects at a larger angle than the light with lower energy (red).

During the collection of EELS spectra, the electron beam intensity should be controlled to avoid high electron intensity in the spectrum, which may oversaturate it. Alignments of the spectrometer are required to make the ZLP appear symmetrical, and calibrate its energy dispersion scale.

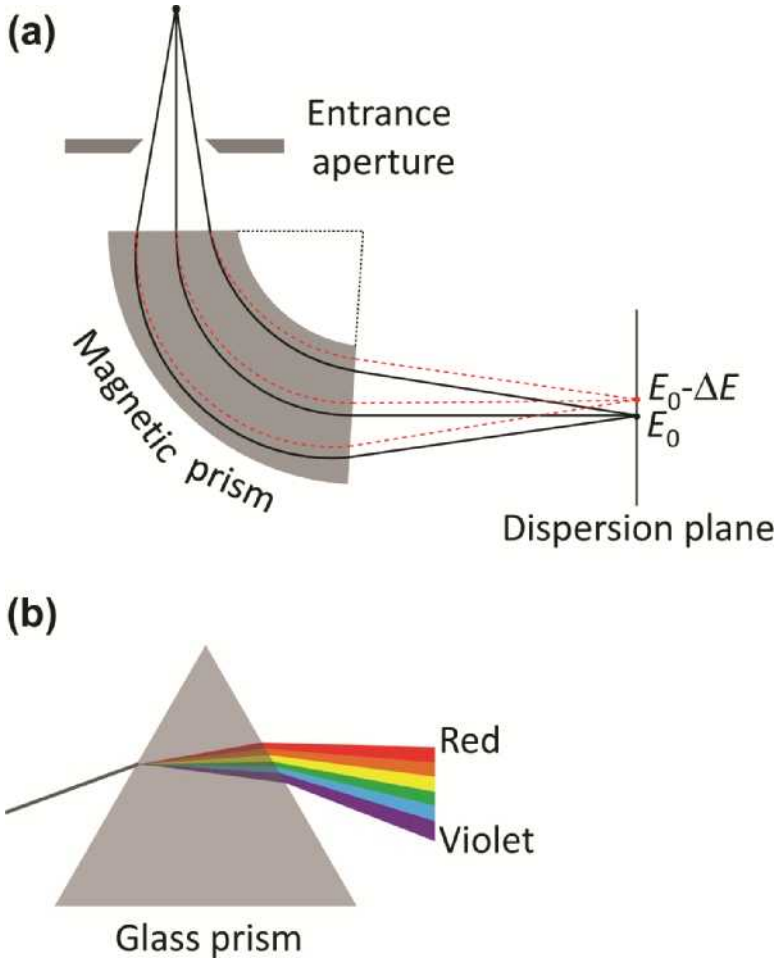

Fig. 8.15 (a) Magnetic prism to separate electrons with different energies; (b) optical glass prism to separate white mixed lights.

An example of an EELS spectrum is shown in Fig. 8.16(a), which contains a ZLP, and broad peaks from plasmon resonance. Note that the ZLP has high electron intensity. At higher energy-loss level, elemental ionization edges can be found, as shown in Fig. 8.16(b). These edges are formed on the high background. One may select a window (shadowed in Fig. 8.16b) in the front of the edge to simulate the background using the power law as

$$I = A \cdot E^{-r} \tag{8.5}$$

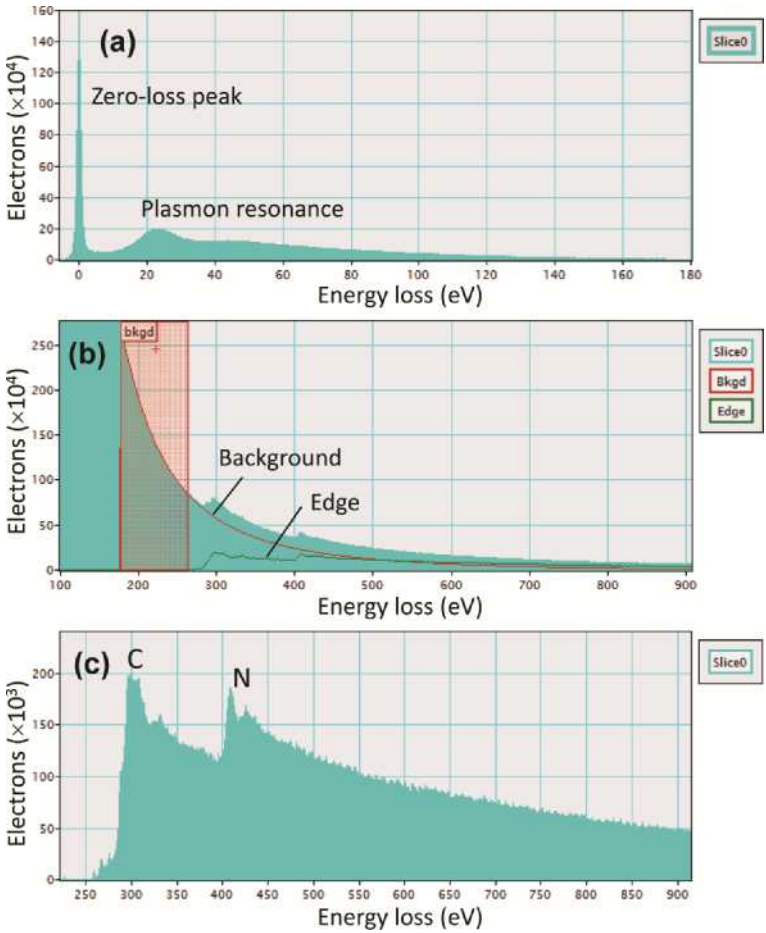

Fig. 8.16 (a) EELS spectrum showing ZLP; (b) EELS spectrum showing two edges, and a shadowed area before the edges is selected to define the background; (c) background-subtracted spectrum.

Here, I is the intensity (y axis), E is the energy loss (x axis), and A and r are the two fitting parameters. After subtracting the calculated background using Eq. 8.5, the edge peak is shown in Fig. 8.16(c). The notation of ionization edges is shown on the left side of Fig. 8.2.

8.2.2 *EELS Qualitative and Quantitative Analyses*

The EELS spectra can be used for both qualitative and quantitative analyses. Since the EELS signals are recorded below the specimen, the specimen should be thin enough to provide good EELS spectra for these analyses.

In the EELS spectrum, the characteristic edges are formed by ionization of core-shell electrons with different energy levels (refer to Fig. 8.2), and thus the energy level of the edge can be used to identify the specific elements. In practice, it is very important to calibrate the spectrometer first to ensure the correct zero-loss position and the energy dispersion to ensure the correct energy of the edge. Afterward, the identification of the edges is straightforward with even fewer possible artifacts than EDS. In the EELS spectrum in Fig. 8.16(c), the two edges are identified as C *K* and N *K* edges, at 281 and 401 eV, respectively.

To quantify the EELS spectra, suppose the sample contains A and B elements. Similar to the EDS quantification in Eq. 8.2, we have [6, 7, 12]

$$\frac{N_{\mathrm{A}}}{N_{\mathrm{B}}} = \frac{I_{\mathrm{A}}(\beta,\Delta)}{I_{\mathrm{B}}(\beta,\Delta)} \cdot \frac{\sigma_{\mathbf{B}}(\beta,\Delta)}{\sigma_{\mathbf{A}}(\beta,\Delta)} \tag{8.6}$$

where N represents the number of atoms per unit area of the specimen with thickness t; β, collection semiangle; Δ, energy window; I, the intensity above the background; and σ, partial ionization cross section. The subscripts A and B indicate the elements A and B, respectively. Both I and σ are functions of β and Δ. The intensity can be measured by subtracting the background using Eq. 8.5, and the cross section σ_{K} can be calculated using the EELS software provided on the instrument. The composition ratio

$$\frac{C_A}{C_B} = \frac{N_A}{N_B} \tag{8.7}$$

and therefore, C_{A} and C_{B} can be obtained under the condition of $C_{\mathrm{A}} + C_{\mathrm{B}} = 1$. The EELS software can provide the composition outputs.

To get accurate quantification results, it is very important to use very thin specimen, and choose appropriate beam convergence semiangle α and spectrometer collection semiangle β. The α is controlled by the condenser aperture size and/or the condenser lenses (C1 and C2), and β is controlled by the selection of the spectrometer entrance aperture, and the experimental mode (either diffraction or image mode) [7]. A simple case of a dedicated STEM mode is shown in Fig. 8.17. Let's only change the electron beam with different α angles while the specimen and the

entrance aperture are fixed (the angle β is thus fixed, which is determined by $\beta = 0.5d/h$ according to the geometry as shown in Fig. 8.17a). In Fig. 8.17(a), the incident electrons focus on a point in a semi-angle angle α, forming a cone shape (the cone is filled with electrons). Let $\alpha = \beta$. Consider the ray 1 on the surface of this cone, which can either go straight as ray 2 without any scattering, or scattered at different angles. Since $\alpha = \beta$, the scattered ray 3, in an angle of 2β with ray 2, can just enter the aperture. Other electrons between these two rays of 2 and 3 have scattering angles less than 2β. If $\alpha < \beta$, as shown in Fig. 8.17(b), since the ray 3 scattered at 2β is excluded by the entrance aperture, the electrons that can enter the aperture are at the scattering angles less than 2β. However, if $\alpha > \beta$, as shown in Fig. 8.17(c), the unscattered ray 2 is excluded by the entrance aperture (while other unscattered electrons with less convergence angles can still enter), scattered electrons with scattering angle larger than 2β can also enter the aperture. This situation should be avoided. In the EELS experiment, select $\alpha \leq \beta$ so that the electrons experience less scattering events. Note that if the EELS is done using a TEM image or diffraction mode (rather than STEM) with a broad parallel beam, β is very large. For example, in the TEM image mode without an objective aperture, $\beta > 100$ mrad, and thus α has no effect on the quantification.

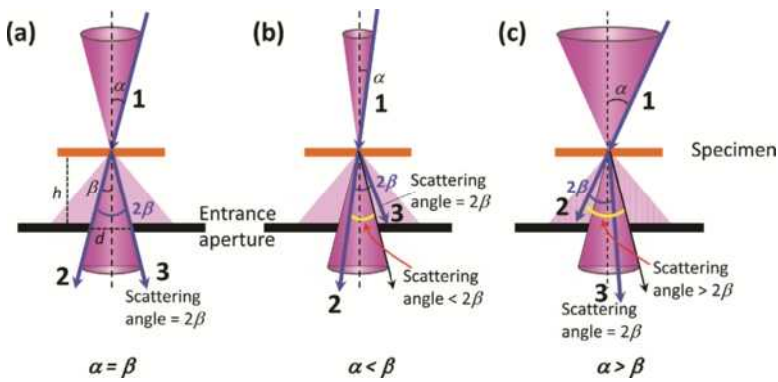

Fig. 8.17 Beam convergence semiangle α and spectrometer collection semiangle β in the STEM mode. (a) $\alpha = \beta$; (b) $\alpha < \beta$; (c) $\alpha > \beta$.

Using the EELS spectrum in Fig. 8.16(b), a quantification yields atomic ratio of 1.00 C and 0.85 N, or 54.0 at.% C and 46.0 at.% N only when two elements are present. The following conditions are used for the quantification: 200 kV beam energy, 5.0 mrad convergence angle, and 100.0 mrad collection angle. The background is fit using power law, and the cross section model is computed using Hartree–Slater model, as shown in Fig. 8.18.

8.2.3 *Energy-Filtered TEM*

As shown in a comparison between EDS and EELS in Table 8.1, more information can be retrieved from EELS than EDS, and it has been widely used in physical and biological sciences [7, 12–14]. Although nowadays the elemental qualitative and quantitative analyses are routinely done by EDS, EELS can provide electronic structure information that is not possible by EDS. In addition, if installed with an EELS energy filter, energy-filtered TEM (EFTEM) can provide enhanced imaging capabilities. Here, two major EFTEM applications are demonstrated.

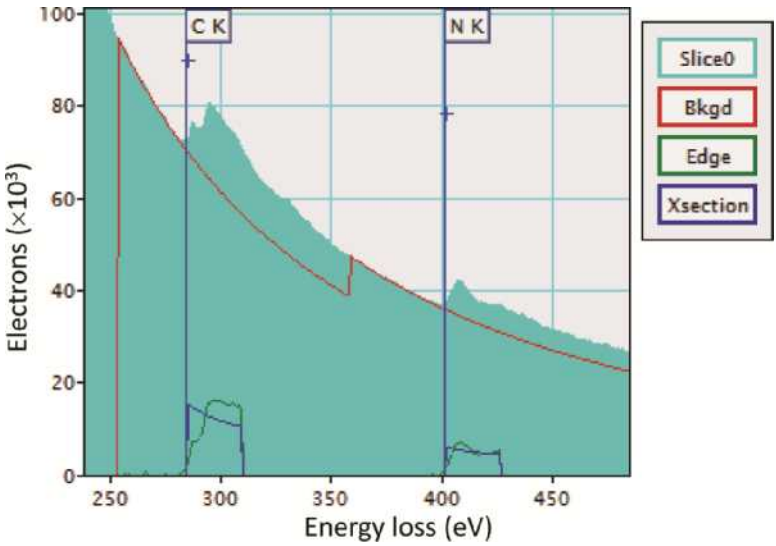

Fig. 8.18 Quantification of an EELS spectrum.

(a) Zero-Loss Filtering

Without energy filtering, the inelastically scattered electrons contribute to the final images and diffraction patterns. These electrons have different energies, causing focusing problems. Especially for thick samples, the image appears as blurry which cannot be focused anyway. In the diffraction pattern, the inelastic electrons contribute to the halo background and thus the diffraction maxima show reduced intensities over the background.

Zero-loss filtering is done by using an energy filter to pass the zero-loss electrons only for either images or diffraction patterns. After the filtering, only elastic electrons without any energy loss are included. The filtered images can have improved contrast and focusing quality.

Fig. 8.19 shows comparisons of unfiltered (left) and filter (right) images and diffraction patterns from a Ni-base superalloy. After the filtering, the dislocations and a particle (arrow indicated) appear clearly. In the diffraction pattern, both diffraction maxima (spots) and Kikuchi lines display clearly after filtering.

The operation of zero-loss filtering is straightforward. In the EFTEM mode, once ZLP is aligned and calibrated, all acquired images or diffraction patterns are already zero-loss filtered, unless the filter is deactivated.

(b) Elemental Mapping Methods

EFTEM can be used to selectively map elements. This process is normally faster than the EDS mapping. There are two mapping modes routinely used: three-window method and jump-ratio method.

The three-window method is the most used one. As illustrated in Fig. 8.20(a), there are three windows to be defined: one window after the edge (post-edge), and two windows before the edge (pre-edge 1 and pre-edge 2). These two pre-edges are used to simulate the background using the power law (Eq. 8.5), and the map is the subtraction of the background image from the post-edge image, that is, only the shadowed area in Fig. 8.20(a) contributes to the elemental map.

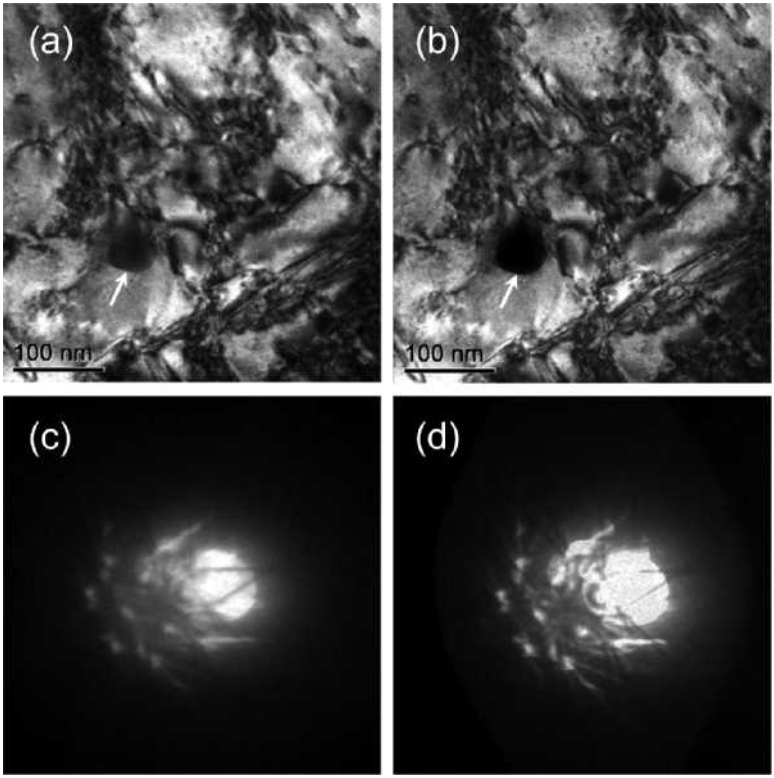

***Fig. 8.19** Unfiltered (a) and filtered (b) images, and unfiltered (c) and filtered (d) diffraction patterns.*

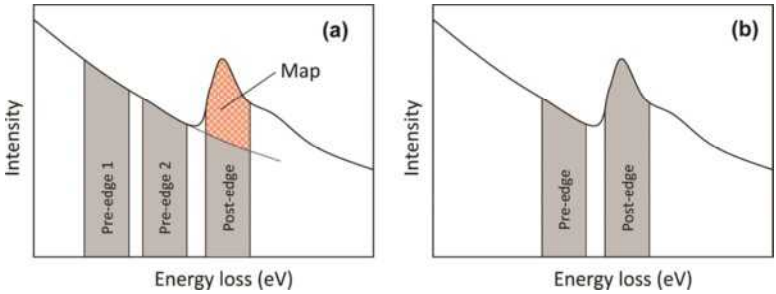

***Fig. 8.20** (a) EELS mapping using standard three-window method; (b) jump-ratio mapping using two windows.*

Jump-ratio mapping is done by only using two windows: one post edge and one pre edge. The mapping is a division of the post-edge image over the pre-edge image (Fig. 8.20b). In case the elemental concentration

is too low to use the three-window method, the jump-ratio method can be used [13]. It can enhance qualitative elemental information and reduce the effects of diffraction contrast on the image. However, it should be noted that the jump-ratio maps cannot be used for quantification and sometimes they are susceptible to background slope changes due to specimen thickness variations. Therefore, normally the mapping should be done using the standard three-window method. During the three-window mapping, the user may save the three images for post-processing, and the jump-ratio image can be calculated by a simple math calculation using any other program. However, the three-window elemental map has to be done using the EFTEM computer program.

Fig. 8.21 presents an example of a Fe–Zr alloy [15]. The zero-loss image is shown in Fig. 8.21(a), exhibiting polycrystalline grains. The images of pre-edges 1 and 2 are shown in Fig. 8.21(b) and (c), respectively, and the post-edge image is shown in Fig. 8.21(d). Dividing the post-edge image in Fig. 8.21(d) with the pre-edge 2 image in Fig. 8.21(c) results a jump-ratio image in Fig. 8.21(e). The brighter regions indicate the Fe distribution, while the grain structures are not clearly revealed. However, the Fe map by the three-window method is shown in Fig. 8.21(f). The brighter areas indicate the higher concentrations of Fe. The grain structures are resolved, which are comparable with the zero-loss image in Fig. 8.21(a).

8.2.4 *EFTEM Experimentation and Applications*

The EFTEM experiments involve more procedures than EDS. Basically, the following procedures are needed:

1. Perform routine alignments of the TEM.
2. Find a ZLP and tune the spectrometer to get a symmetrical ZLP.
3. Get an EELS spectrum to ensure the elements are present.
4. Shift the energy loss to 110 eV (recommended for most cases), and in the live search mode, increase the beam intensity as needed until a clear image appears, and focus the image. As the energy window moves away from 0 eV, the image normally appears as out of focus. This is a very important step to get well-focused maps.

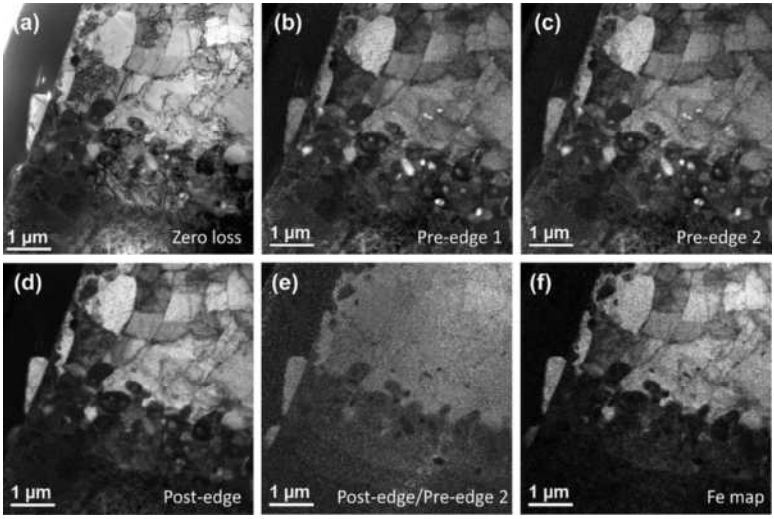

Fig. 8.21 Mapping Fe in a Fe–Zr alloy. (a) Zero loss image; (b) pre-edge 1 image; (c) pre-edge 2 image; (d) post-edge image; (e) jump-ratio image obtained by dividing the post-edge image in (d) over the pre-edge 2 image in (c); (f) Fe map formed by three-window method.

5. Select the analyzing element and edge, and define the post-edge, pre-edge 1, pre-edge 2, and exposure time to start the mapping process. The program can provide auto or manual tracking to avoid sample drifting, which can be switched off (or do not shift the image during the manual tracking) if the sample drifting is not an evident problem.
6. Repeat step (5) to map any other elements.
7. Assign maps with different colors, and superimpose them together to get an image displaying the elemental distribution. This process can be done using Color Mix of DigitalMicrograph (or other image processing programs). Different maps may not be at the same location if there is a drift. During the superimposing, manually shift them back to the same position.

During the EFTEM experiment, ZLP alignment should be done often to ensure the correct energy positions.

Fig. 8.22(a) shows a Fe NP coated with carbon shells [16]. The Fe and C maps, taken using three-window method, are shown in Fig. 8.22(b) and (c), respectively. Further, color the Fe map green, and the

carbon map blue, as shown in Fig. 6.18(d) and (e), respectively. Afterward, superimpose these two colored maps together as a map with two different colors, as shown in Fig. 6.18(f), which clearly the Fe cores covered with C shells. If the Fe and C maps were not colored, they would not show clearly in the superimposed map.

EFTEM characterization of magnetic graphene nanocomposites is demonstrated in Fig. 8.23 [17]. In the zero-loss image in Fig. 8.23(a), Fe_2O_3 oxide NPs are dispersed on graphene sheets. Fig. 8.23(b) depicts the C map, where the brighter cracking-shaped area shows the folded nature at the edge or stacking phenomena among individual graphene sheets. The Fe map and O map exhibit basically the same elemental distributions, as shown in Fig. 8.23(d) and (e), respectively. Their superimposed image is shown in Fig. 8.23(g), indicating that the NPs are iron oxide. On the other hand, summation of Fe and C maps yields the map in Fig. 8.23(h). The summation of Fe, C, and O gives the elemental distribution, as shown in Fig. 8.23(i).

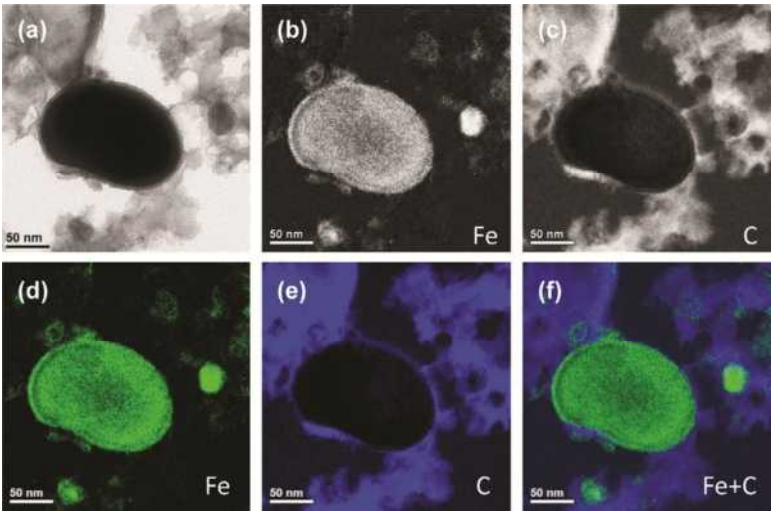

Fig. 8.22 EFTEM of Fe/C core/shell NPs. (a) Zero-loss image; (b) Fe map; (c) C map; (d) colored Fe map; (e) colored C map; (f) superimposed maps of Fe and C.

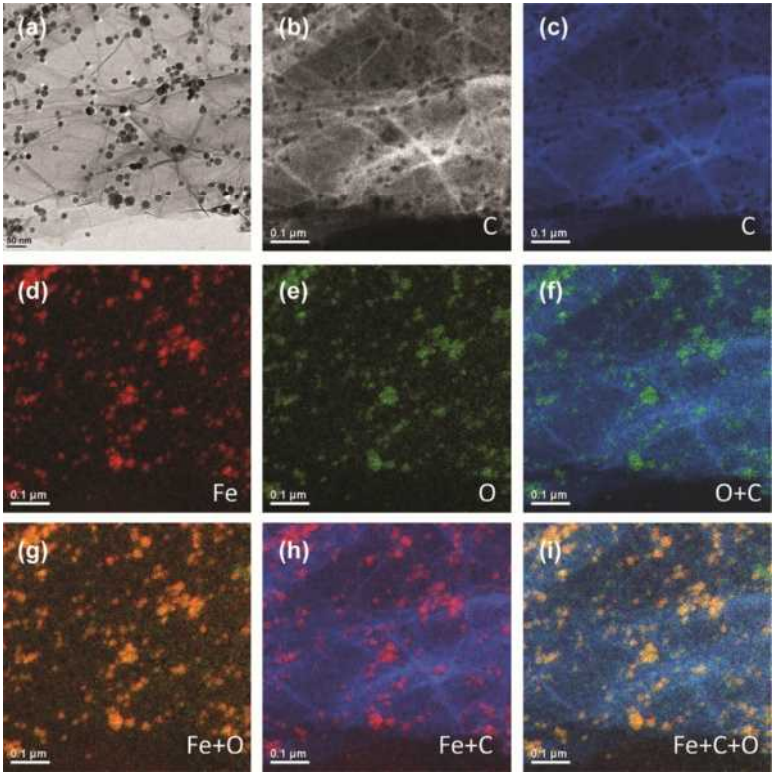

Fig. 8.23 EFTEM of the magnetic graphene nanocomposites. (a) Zero-loss image; (b) C map; (c) colored C map; (d) colored Fe map; (e) colored O map; (f) colored O+C map; (g) colored Fe+O map; (h) colored Fe+C map; (i) colored Fe+C+O map.

EDS and EELS can be used together to characterize materials. Fig. 8.24(a) shows a typical TEM image of PbSeTe ternary alloy nanocubes, demonstrating a perfect cubic morphology and relatively uniform size distribution with an average side length of 11.0 nm [18]. An SAED pattern is inserted, which shows the nanocubes are all [001] oriented and well aligned to exhibit textured features. Careful inspection, with astigmatism corrected and well-focused, reveals a single lattice, that is, all the reflection spots in the rings are from a single lattice. HRTEM of a single nanocube (Fig. 8.24b) shows clear lattice fringes, with an interfringe distance of ~3.18 Å over the entire nanocube surface. This analysis suggests that the as-prepared PbSeTe is a uniform

alloy without a heterogeneous structure. An EDS line scan over a single nanocube in the STEM mode is shown in Fig. 8.24(c), which reveals the compositional variation over a single nanocube. The EDS intensity profiles of Pb, Se, and Te are plotted as a function of the distance crossing the nanocube, showing uniform distributions of Pb, Se, and Te through the scanned area. This further verifies a ternary alloy structure in the as-formed PbSeTe. The elemental maps of Pb (red), Se (purple), and Te (green) are shown in Fig. 8.24(d)–(f), respectively. These elements are uniformly distributed in each cube with the same cube size in each map. The Se+Te overlap map is shown in Fig. 8.24(g), indicating an even distribution for both Se and Te elements. This further confirms the ternary alloy structure.

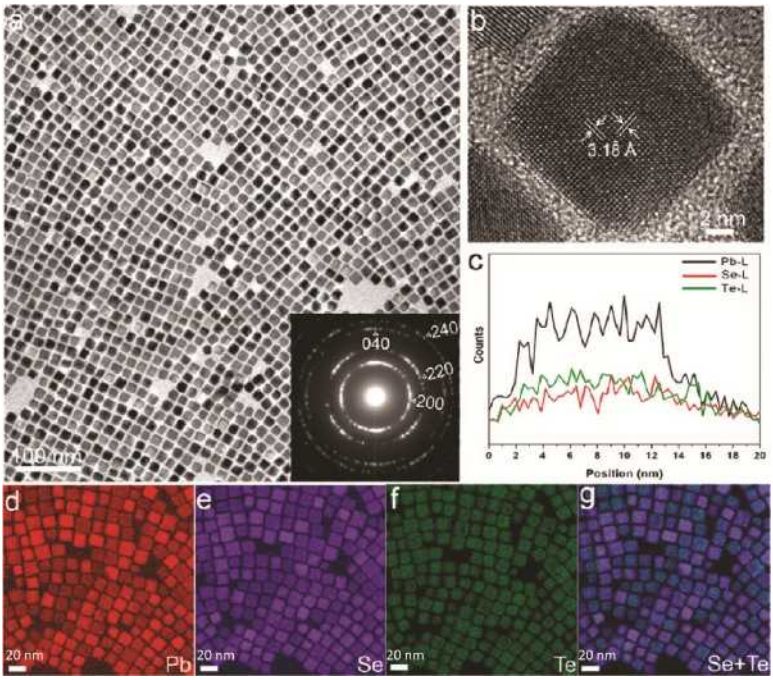

Fig. 8.24 PbSeTe ternary alloy single nanocubes. (a) TEM image; inset is an SAED pattern; (b) HRTEM image; (c) STEM EDS line scan profile of an individual nanocube; (d–g) elemental maps of Pb, Se, Te, and Se+Te overlap, respectively.

Fig. 8.25 shows TEM characterization of PbSeTe ternary alloy core/shell nanocubes synthesized differently from the nanocubes in Fig. 8.24 [18]. Fig. 8.25(a) presents a TEM image of the PbSeTe nanocubes, with averaged size of 11.0 nm. An SAED pattern is shown in Fig. 8.25(b), with special precaution exercised to avoid any astigmatism or unfocus. Apparent double rings can be observed, as indicated by double markers.

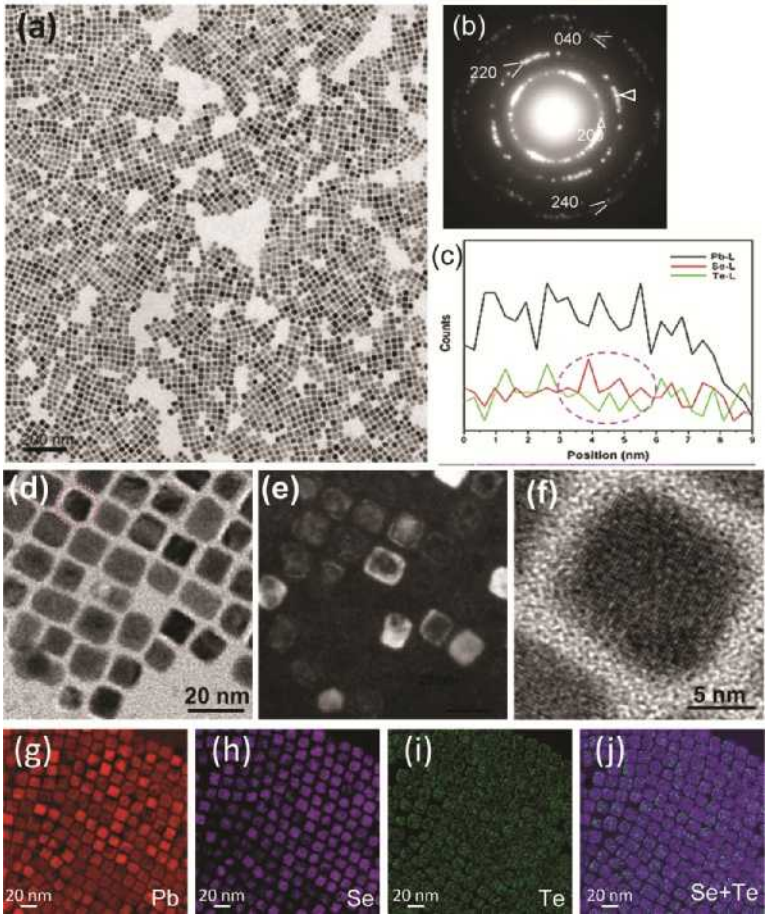

Fig. 8.25 PbSeTe core/shell nanostructures. (a) TEM overview image; (b) SAED; (c) STEM EDS line scan profile of PbSeTe core/shell nanocubes; (d) magnified TEM image; (e) WBDF image of (d); (f) HRTEM image of the circled particle in (d); (g–j) elemental maps of Pb, Se, Te, and their Se+Te overlap, respectively.

The distance between the double rings is related to the scattering angle, or the radius of the ring. At higher scattering angles, the distance is larger. The radius of the first ring is too small to be evident in the pattern. The compositional architecture of these core/shell nanocubes was supported by STEM EDS line scan analysis across one nanocube. Fig. 8.25(c) suggests that more Se is present in the center and more Te is distributed along the edges, as shown in the circled area. Note that, due to the spurious signals in the EDS from the surrounding areas, the line scan profiles do not correspond to the core/shell positions, as the scale is so small. A high magnification image is shown in Fig. 8.25(d), and a corresponding WBDF image of this area is presented in Fig. 8.25(e), depicting shell structures and indicating double lattices due to the strain field induced by the mismatch between the shell and the core. A HRTEM image of the circled particle in Fig. 8.25(d) is shown in Fig. 21(f), which reveals complex features formed by the interference of these two lattices. Furthermore, the core/shell structure is confirmed by their elemental mapping results (Fig. 8.25g–j), in which Pb is seen uniformly distributed in the nanocubes and Te prefers to reside only in the shells, whereas more Se appears in the cores. Note that the cube size of Se in Fig. 8.25(h) is slightly smaller than the cubes of Pb or Te images, with larger gaps between the cubes, indicating the Se is in the core area.

References

[1] R.D. Leapman, J.A. Hunt. Comparison of detection limits for EELS and EDXS. *Microsc. Microanal. Microstruct.* **2**, 231–244 (1991).

[2] H. Müllejans, J. Bruley. Electron energy-loss spectroscopy (EELS); comparison with X-ray analysis. *J. de Phys. IV* **03**, 2083–2092 (1993).

[3] P. Kohler-Redlich, J. Mayer. Quantitative analytical transmission electron microscopy. In: *High-Resolution Imaging and Spectrometry of Materials*, edited by M. Rühle, F. Ernst. Springer, New York. pp. 119–188 (2003).

[4] Oxford Instruments. *EDS in the TEM Explained*. Retrieved from http://www.oxford-instruments.com.

[5] Z. Luo, Y. Song, S. Zhang, D.J. Miller. Interfacial microstructure in a B_4C/Al composite fabricated by pressureless infiltration. *Metall. Mater. Trans.* **A43**, 281–293 (2012).

[6] D. Shindo, T. Oikawa. *Analytical Electron Microscopy for Materials Science*. Springer Japan, Tokyo, 2002.

[7] D.B. Williams, C.B. Carter. Transmission Electron Microscopy: A Textbook for Materials Science. Springer, New York, 2009.

[8] G. Cliff, G.W. Lorimer. The quantitative analysis of thin specimens. *J. Microsc.* **103**, 203–207 (1975).

[9] J. Zhang, H. Yang, B. Martens, Z. Luo, D. Xu, Y. Wang, S. Zou, J. Fang. Pt–Cu nanoctahedra: Synthesis and comparative study with nanocubes on their electrochemical catalytic performance. *Chem. Sci*. **3**, 3302–3306 (2012).

[10] S.-H. Chen, C.-C. Chen, Z.P. Luo, C.-G. Chao. Fabrication and characterization of eutectic bismuth-tin (Bi-Sn) nanowires. *Mater. Lett.* **63**, 1165–1168 (2009).

[11] Z. Sun, Z. Luo, J. Fang. Assembling nonspherical 2D binary nanoparticle superlattices by opposite electrical charges: The role of Coulomb forces. *ACS Nano* **4**, 1821–1828 (2010).

[12] R.F. Egerton. *Electron Energy Loss Spectroscopy in the Electron Microscope.* Third Edition. Springer, New York, 2011.

[13] F. Hofer, W. Grogger, P. Warbichler, I. Papst. Quantitative energy-filtering transmission electron microscopy (EFTEM). *Mikrochim. Acta* **132**, 273–288 (2000).

[14] V.J. Keast. Application of EELS in materials science. *Mater. Charact.* **73**, 1–7 (2012).

[15] C.-C. Wei, A. Aitkaliyeva, Z. Luo, A. Ewh, Y. Sohn, J.R. Kennedy, B.H. Sencer, M.T. Myers, M. Martin, J. Wallace, M.J. General, L. Shao. Understanding the phase equilibrium and irradiation effects in Fe–Zr diffusion couples. *J. Nucl. Mater.* **432**, 205–211 (2013).

[16] J. Zhu, S. Pallavkar, M. Chen, N. Yerra, Z. Luo, H.A. Colorado, H. Lin, N. Haldolaarachchige, T.C. Ho, D.P. Young, S. Wei, Z. Guo. Magnetic carbon nanostructures: Microwave energy–assisted pyrolysis vs conventional pyrolysis. *Chem. Commun.* **49**, 258–260 (2013).

[17] J. Zhu, M. Chen, H. Qu, Z. Luo, S. Wu, H.A. Colorado, S. Wei, Z. Guo. Magnetic field induced enhancement in capacitance of graphene and magnetic graphene nanocomposites. *Energy Environ. Sci.* **6**, 194–204 (2013).

[18] Z. Quan, Z. Luo, W.S. Loc, J. Zhang, Y. Wang, K. Yang, N. Porter, J. Lin, H. Wang, J. Fang. Synthesis of PbSeTe single ternary alloy and core-shell heterostructured nanocubes. *J. Am. Chem. Soc.* **133**, 17590–17593 (2011).

CHAPTER 9

Specific Applications

Characterizations of materials by a transmission electron microscope (TEM) require not only instrumental operation skills, but also data processing and computation skills to interpret the results. To meet the needs of TEM characterization for specific applications, various TEM techniques have been developed.

The imaging methods with different contrast mechanisms and electron diffraction techniques introduced so far in this book are mainly based on qualitative descriptions. However, more meaningful information may be retrieved from quantification of the images or diffraction patterns that may be routinely ignored when such quantification efforts are not applied.

If the sample is solid and conductive, such as metals, the TEM analyses are relatively straightforward, while for liquid or beam-sensitive materials, the TEM analyses are more challenging. In this respect, methodologies to study biological samples have been applied to investigate material samples. For example, as mentioned in Chapter 2 in Volume 1, the liquid sample can be prepared by negative staining (Section 2.1). However, a more direct method is to freeze the liquid sample and observe it in TEM while it stays in a frozen status.

Some TEM specimens are very sensitive to the electron beam. Even using a very weak beam, they often exhibit damaged structures in the recorded images. For these materials, low-dose imaging has been developed.

A shortcoming of TEM is that the TEM image is only a 2D picture of the 3D sample. To overcome this 2D problem, electron tomography (ET) has been developed.

In the previous chapters, fundamentals about diffraction, imaging, and elemental analyses have been introduced. This chapter moves further to some specific applications of TEM, in the areas of quantitative electron microscopy, *in situ* electron microscopy, cryoelectron microscopy (cryo-EM), low-dose imaging, and ET.

9.1 Quantitative Microscopy

From quantitative processing of the TEM data, additional information can be retrieved [1–8]. Much progress has been made to reveal or solve the crystalline atomic structures or atomic positions from TEM or scanning TEM (STEM) data at high magnifications [1–5, 7].

In this section, imaging processing is made on the TEM images taken at medium to low magnifications (lower than atomic resolution), in terms of microstructure homogeneities. A particular example is the dispersion degree of composites, which is technically a very important parameter to evaluate the composites. It has been well accepted that a good dispersion of fillers favors the mechanical and physical properties, while large agglomerates are the weak sites to reduce such properties. How to quantify the dispersion degrees can be done based on TEM investigations. In addition, the polycrystalline powder electron diffraction patterns can be processed quantitatively.

9.1.1 *Quantification of Size Homogeneity*

We start with the quantification of size homogeneity. In TEM studies, it is often needed to measure the object size [9]. Suppose a set of measurements is done, the measurement data are then divided into groups with interval of Δx, and the frequency density f_i of the i-th group is

$$f_i = \frac{n_i}{N \cdot \Delta x} \tag{9.1}$$

where n_i is the number of data falling into this group, and N is the total number of the measurements. Therefore, a histogram can be constructed to exhibit the spacing data distribution, as shown in Fig. 9.1(a). If the interval Δx is small enough (usually divided into 10–100 classes) and the number of measurements N is large sufficiently (usually over 100), one may obtain a curve of the frequency function, that is, the probability density function (PDF) $f(x)$ on the measurement data, as shown in Fig. 9.1(a). The $f(x)$ has a mean value μ and a standard deviation σ. As the number of measurements N is sufficiently large, the sample mean $\overline{x}$ and sample standard deviation s may be used to estimate the population mean μ and the population standard deviation σ, respectively, that is, $\hat{\mu} = \overline{x}$

and $\hat{\sigma} = s$, where $\hat{\mu}$ and $\hat{\sigma}$ are the estimators of μ and σ, respectively. It is apparent that the size distribution character is related to σ, as a lower σ makes a higher degree of homogeneity. However, the quantity σ is not a good measure of the homogeneity degree, as it depends on the unit of the size, and thus the homogeneity degrees of measurements in different size ranges are not comparable using σ. For example, for two sets of measurements with μ_1 = 10.5 nm and σ_1 = 0.5 nm and μ_2 = 5.0 μm and σ_2 = 0.4 μm, one cannot compare their homogeneities by comparing σ_1 and σ_2. Only with the same μ, the homogeneity degree can be compared through σ. If μ_1 = 10.5 nm and σ_1 = 0.5 nm and μ_2 = 10.5 nm and σ_2 = 0.4 nm, the second set has a higher homogeneity degree because of a lower σ.

Considering a data distribution $f(x)$ with mean μ in the entire range, we may define the homogeneity degree as the probability within a certain data range around μ, and thus two quantities, $H_{0.1}$ and $H_{0.2}$, in the range of $\mu \pm 0.1\mu$ and $\mu \pm 0.2\mu$, respectively, are obtained as follows:

$$H_{0.1} = \int_{0.9\mu}^{1.1\mu} f(x) \cdot dx \tag{9.2a}$$

$$H_{0.2} = \int_{0.8\mu}^{1.2\mu} f(x) \cdot dx \tag{9.2b}$$

By this definition, the homogeneity quantities, $H_{0.1}$ and $H_{0.2}$, are the areas in the $\mu \pm 0.1\mu$ and $\mu \pm 0.2\mu$ ranges, respectively (shadowed areas in Fig. 9.1b). A distribution with higher degree of data concentration, that is, less σ, would possess higher PDF around μ, and thus it possesses higher H values according to this definition. Note that $H_{0.1}$ and $H_{0.2}$ are dimensionless quantities, and thus it is possible to compare the homogeneity degrees of measurements in different units through $H_{0.1}$ and $H_{0.2}$.

For the common normal, lognormal, gamma, and Weibull distributions, the quantities of $H_{0.1}$ and $H_{0.2}$ have been formulized as function of the ratio μ/σ [9], as plotted in Fig. 9.1(c). Both $H_{0.1}$ and $H_{0.2}$ are monotonic functions of μ/σ. Therefore, if μ/σ is known, $H_{0.1}$ and $H_{0.2}$ are uniquely determined. For simplicity, one may use only $H_{0.1}$ to quantify the homogeneity.

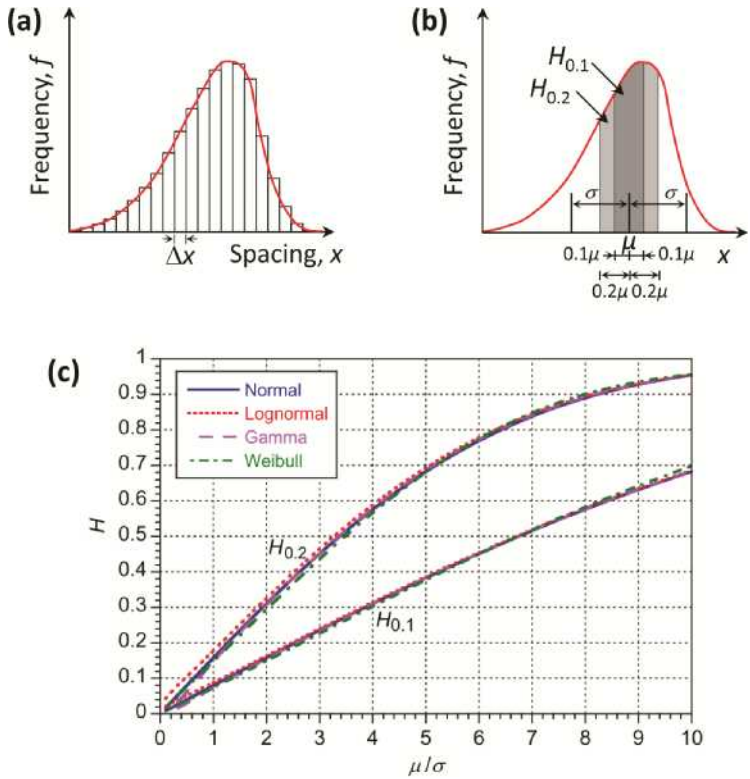

***Fig. 9.1** (a) Construction of histogram; (b) definition of homogeneity $H_{0.1}$ and $H_{0.2}$ quantities from the frequency function f(x); (c) $H_{0.1}$ and $H_{0.2}$ as a function of μ/σ.*

In practice, it is found that most of the measurements obey the lognormal distribution, whose homogeneity is expressed as:

$$H_{0.1} = 1.1539\times10^{-2} + 7.5933\times10^{-2}\left(\frac{\mu}{\sigma}\right) + 6.6838\times10^{-4}\left(\frac{\mu}{\sigma}\right)^2 - 1.9169\times10^{-4}\left(\frac{\mu}{\sigma}\right)^3 + 3.9201\times10^{-6}\left(\frac{\mu}{\sigma}\right)^4 \quad (9.3a)$$

$$H_{0.2} = 2.266\times10^{-2} + 0.15629\left(\frac{\mu}{\sigma}\right) + 4.442\times10^{-4}\left(\frac{\mu}{\sigma}\right)^2 - 1.2738\times10^{-3}\left(\frac{\mu}{\sigma}\right)^3 + 5.9978\times10^{-5}\left(\frac{\mu}{\sigma}\right)^4 \quad (9.3b)$$

Fig. 9.2 demonstrates the size homogeneity quantifications using two samples A and B, with different size distributions [9]. The sample A

contains particles with variable size. A representative TEM image is shown in Fig. 9.2(a), and the measured histogram is shown in Fig. 9.2(b), compared with the calculated PDF's using normal, lognormal, gamma, and Weibull models, respectively. The measurement statistics are listed in Table 9.1. According to the measured ratio $\bar{x}/s$ = 2.008, $H_{0.1}$ values are calculated by replacing μ/σ with $\bar{x}/s$ in the formulas for different models (the formulas can be found in reference [9]), as listed in Table 9.2. As the lognormal model gives the best fit, with the correlation coefficient r = 0.963, which is the highest among others, the homogeneity of the sample A is quantified as $H_{0.1} = 16.5\%$ by the lognormal model. Therefore, 16.5% particles are in 1.081–1.321 μm range ($0.9\bar{x} - 1.1\bar{x}$ range).

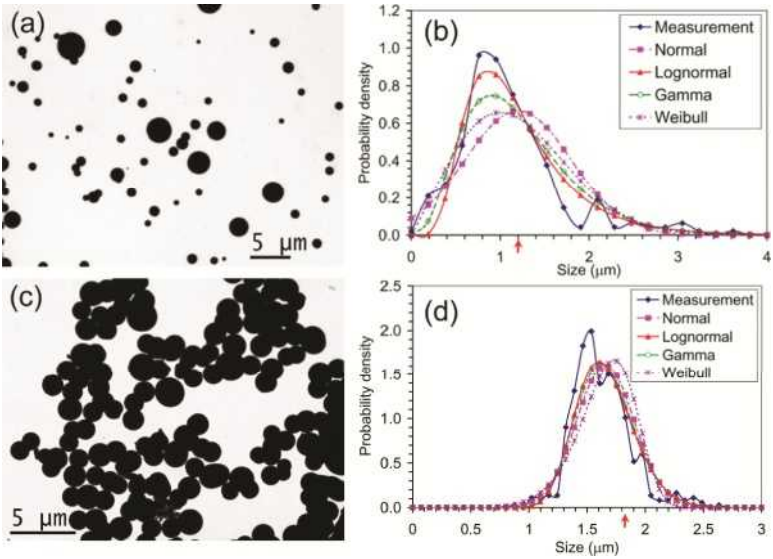

Fig. 9.2 (a) Representative TEM image of the sample A with variable size; (b) probability density distributions of the sample A; (c) representative TEM image of the sample B with homogeneous size; (d) probability density distribution of the sample B. Arrow indicates the mean size.

Table 9.1 Measurement statistics of samples A and B in Fig. 9.2.

Sample	$\bar{x}$ (μm)	s (μm)	$\bar{x}/s$	N
A	1.201	0.598	2.008	251
B	1.658	0.249	6.659	501

Table 9.2 Homogeneity quantification of samples A and B in Fig. 9.2.

	Normal distribution		Lognormal distribution		Gamma distribution		Weibull distribution	
	$H_{0.1}$	r	$H_{0.1}$	r	$H_{0.1}$	r	$H_{0.1}$	r
A	15.9%	0.842	16.5%	0.963	15.6%	0.941	15.0%	0.901
B	49.5%	0.938	49.8%	0.965	49.5%	0.957	49.5%	0.885

On the other hand, the sample B contains particles with a more homogeneous size. A representative TEM image is shown in Fig. 9.2(c), and the measured histogram is shown in Fig. 9.2(d), with the measurement statistics listed in Table 9.1. The measured ratio $\bar{x}/s$ = 6.659, which is much higher than that of sample A. Calculated $H_{0.1}$ quantities are listed in Table 9.2, along with the correlation coefficient r of each model. The lognormal gives the best fit with r = 0.965. Therefore, the homogeneity of the sample B is quantified as $H_{0.1}$ = 49.8% by the lognormal model, which are significantly higher than that of sample A.

9.1.2 *Quantification of Directional Homogeneity*

Quantification of directional homogeneities involves circular data. Circular data are angles in the 2D space, including axial data (vary from 0 to π) and directional data (vary from 0 to 2π). Schematic examples of the axial data are shown in Fig. 9.3(a) and (b), where the linear features align well along a direction (the mean direction) in (a), but align in a less degree in (b). Since θ and $\theta + \pi$ are equivalent, the measured θ angle range is π. The angle distribution is plotted on the unit circle in (c), which covers only a half circle. Each point on the circle represents an orientation angle. The directional data examples are given in Fig. 9.3(d) and (e), where the feature directions are considered in (d), or the tangent direction distribution along a curve in (e). Here, the measured angle θ range is 2π. The angle distribution is plotted on the circle in (f), which covers the full circle.

The quantification of angular data, either axial or directional, requires circular statistics. An arbitrary angle θ can be regarded as a unit vector $\mathbf{X}$, or as a point on the unit circle, with Cartesian coordinates of $\cos\theta$ and $\sin\theta$. By measuring the angle θ_i (i = 1, 2, …, N) of a number of features, the mean direction $\bar{\theta}$ is the direction of the resultant vector, $\mathbf{R} = \mathbf{X}_1 + \mathbf{X}_2 + \cdots + \mathbf{X}_N$, with a resultant length R. Dividing this vector $\mathbf{R}$

by the number N yields the mean resultant vector $\overline{\mathbf{R}}$ with length $\overline{R}$, whose coordinates are

$$\overline{C} = \frac{1}{n}\sum_{j=1}^{N}\cos\theta_j,\ \ \overline{S} = \frac{1}{n}\sum_{j=1}^{N}\sin\theta_j \tag{9.4}$$

Thus,

$$\overline{R} = \sqrt{\overline{C}^2 + \overline{S}^2}\ ,\quad \overline{\theta} = \begin{cases} \tan^{-1}\left(\dfrac{\overline{S}}{\overline{C}}\right) & \text{if } \overline{C} \geq 0 \\ \tan^{-1}\left(\dfrac{\overline{S}}{\overline{C}}\right) + \pi & \text{if } \overline{C} < 0 \end{cases} \tag{9.5}$$

The mean resultant length $\overline{R}$ is a measure of the circular data concentration, and $0 \leq \overline{R} \leq 1$. When $\overline{R} = 0$, $\overline{\theta}$ is not defined, which is the case of uniform (or random) distribution; and when all θ_i angles are the same, $\overline{R} = 1$. This mean resultant length value may be used to quantify the homogeneity degree H_{R}, that is

$$H_{\mathrm{R}} = \overline{R} \tag{9.5}$$

Accordingly, $0 \leq H_{\mathrm{R}} \leq 1$. Here, we use the sample mean resultant length $\overline{R}$ to estimate the population mean resultant length ρ, assuming the measurement number n is sufficiently large. Alternatively, similar to the size distribution, one may use $H_{0.1}$ and $H_{0.2}$ to define the circular data homogeneities (shadowed areas in Fig. 9.3c and f), as discussed in reference [9].

An example of directional data is to quantify the line straightness, if the line is long enough to provide sufficient directional data. A carbon nanofiber (CNF) A is straighter in Fig. 9.4(a), while another B is more curved in Fig. 9.4(b). Here, we suppose they are 2D samples, which lay on the flat support films. The lines are divided into small sections and then the tangent direction angles at each point are measured using a program *ImageJ* [10]. The measurements are listed in Table 9.3. It is evident that the angles of fiber A in Fig. 9.4(a) are more concentrated, with H_{R} = 97.3%, while angles of curved fiber B in Fig. 9.4(b) are less concentrated, with H_{R} = 82.2%. The straightness of fiber A is higher than fiber B. If $1 - H_{\mathrm{R}}$ is defined as the curvature, then fiber B has higher curvature and fiber A.

Table 9.3 Quantification of the directional data in Fig. 9.4.

Sample	Measurement			Straightness, H_R	Curvature $1-H_R$
	$\bar{C}$	$\bar{S}$	N		
Straight fiber A in Fig. 9.4(a)	0.8636	0.4478	95	97.3%	2.7%
Curved fiber B in Fig. 9.4(b)	0.8063	0.1576	112	82.2%	19.8%

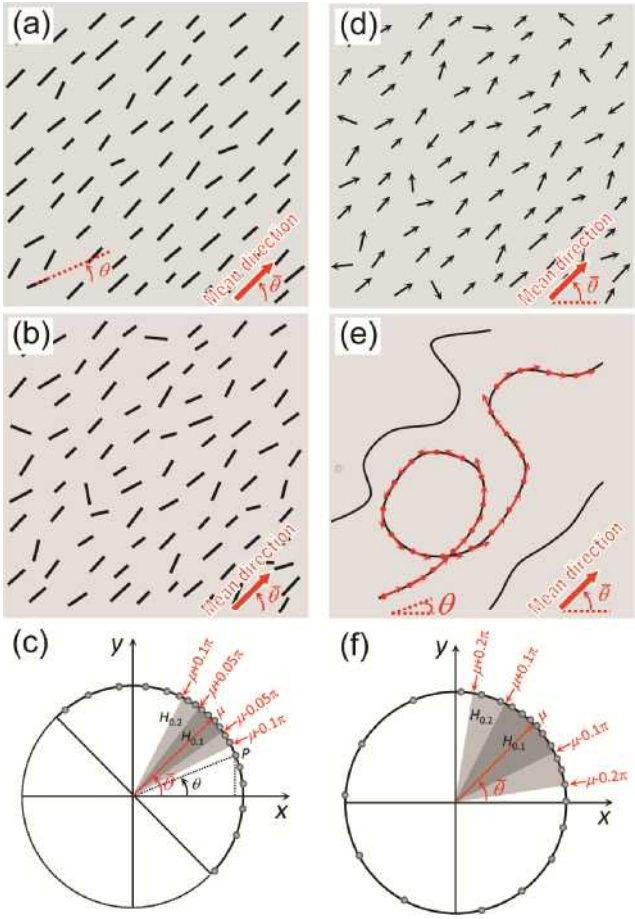

Fig. 9.3 Schematic microstructures showing orientation distributions. The lines align well along a mean direction in (a) but not aligned well in (b), with orientation distribution of axial data on the half circle in (c). Alignments of directional lines in (d) and directions of tangent lines in (e), with orientation distributions on the full circle in (f).

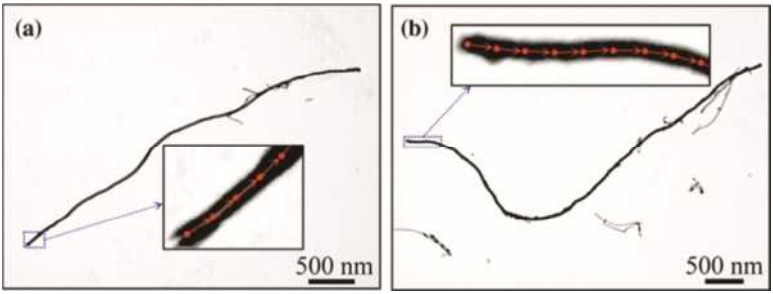

Fig. 9.4 Quantification of a straighter fiber in (a) and a curved fiber in (b). Images are taken by TEM.

9.1.3 Dispersion Quantification

Dispersion degree is an important parameter in composite materials, since it is directly correlated with the material properties. Rather than visual estimation of good or bad dispersions, the dispersion degree should be quantified from the TEM images.

The dispersion quantity is related to the free path spacing between the inclusion particle surfaces (rather than the particle center spacing), regardless of their shape or size [11–13]. The more the uniform spacing between the surfaces of the inclusions, the higher the dispersion grade will be. When all of the inclusion particles are distributed at an equal free path distance, the dispersion is defined as 100%. Fig. 9.5(a) depicts schematically a solid sample with various irregular inclusions (in dark color) in a matrix [13]. A section is made, as shown in Fig. 9.5(b), where these inclusions are seen in a 2D plane view, either on the section surface or on a 2D projection of the very thin section. Since the inclusion particles have very irregular shape, it is difficult to calculate the spacing between them from the particle center (x, y) positions. However, one may use a random line to intercept these particles to obtain the free path spacing measurements between these inclusions, x_1, x_2, …, x_i, …, x_N, as shown in Fig. 9.5(b). If two particles attach together on this line, their spacing is counted as $x = 0$. The data homogeneity $H_{0.1}$ thus becomes the dispersion degree $D_{0.1}$.

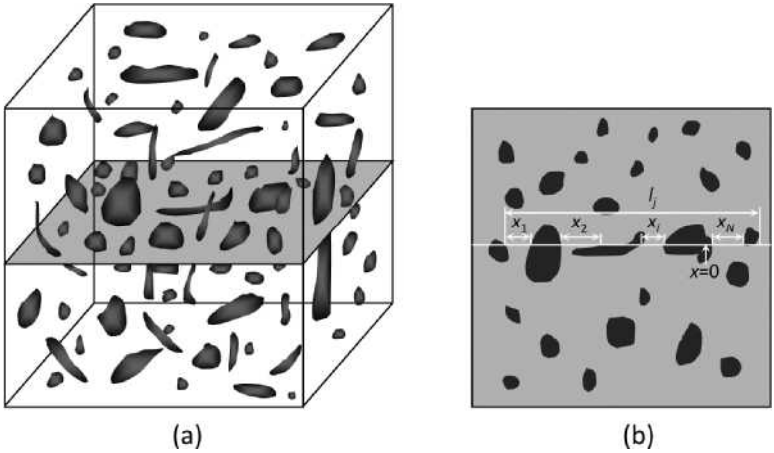

Fig. 9.5 (a) A solid specimen contains various irregular inclusions (dark color) in the matrix; (b) a section from the solid specimen, where free-path spacing of the inclusions is measured.

Below are the procedures to quantify the dispersion $D_{0.1}$ from TEM images:

1. Place arrays of parallel lines over a TEM micrograph, as shown in Fig. 9.6. For isotropic sample, two perpendicular arrays are applied so that dispersions can be measured along both directions, and the sample dispersion is the average dispersion along these two directions. If the sample is anisotropic, the array of parallel lines can be placed along any particular direction, so that the dispersion $D_{0.1}$ is measured along that direction. Depending on the sampling number N of measurements which should be over 100, a TEM image is normally divided into 10–20 grid lines. If the TEM image is taken randomly (or after rotation randomly), the grid lines are placed horizontally and vertically to make the distance measurement easier.
2. Measure the free-path distance x_i using *ImageJ* [10] or other programs. Note that scale bars on the TEM negatives could produce up to 10% error; thus, the scale bars need calibration for accurate distance measurement, refer to Section 3.2.8 for magnification calibration in Volume 1. The sampling number N is expected to be greater than 100; otherwise increase the grid lines, or use more micrographs even make montages of the micrographs to achieve more measurements.

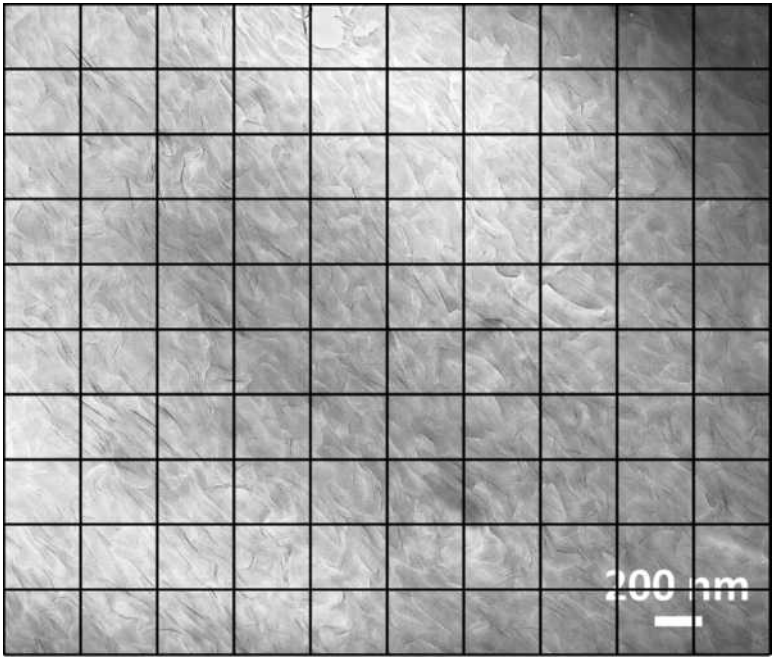

Fig. 9.6 An example of a TEM image, which is divided by 10 × 10 grid lines for the dispersion quantification along the grid lines.

3. Based on a set of free-path distance data, calculate the data sample mean $\bar{x} = \sum_i x_i / N$ and data sample standard deviation $s = \sqrt{\sum_i (x_i - \bar{x})^2 / (N-1)}$.
4. Calculate the dispersion quantity $D_{0.1}$ by using the ratio $\bar{x}/s$ to substitute μ/σ in Eq. 9.3a for lognormal distributions using Eq. 9.3a. Here, $D_{0.1} = H_{0.1}$.

A typical microstructure of a polymer 2102A with 7.5 wt.% 30B clay with a good dispersion degree, exfoliation, is shown in Fig. 9.7(a) [12]. Generally, the original big clay clumps are completely broken up and the clay platelets dispersed all over the entire area. The framed area is magnified in Fig. 9.7(b), where it is seen that the clay platelets are exfoliated and well dispersed within the matrix. For quantitative measurements, Fig. 9.7(a) is divided by 10 × 10 grid lines, and the free-path spacing distances between the clay platelets along these grid lines are measured to construct

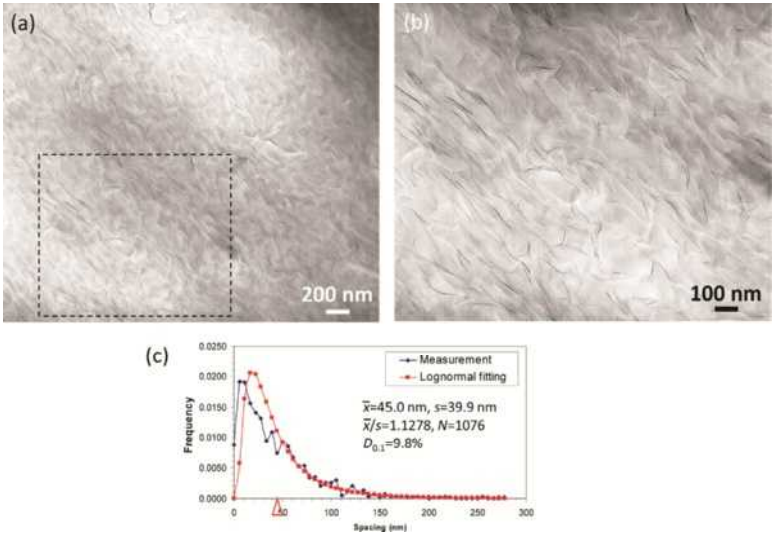

Fig. 9.7 (a) Microstructure of exfoliated 2102A with 7.5 wt.% 30B; (b) magnified image from the framed area in (a); (c) layer spacing distance histogram. Curve fitting by lognormal distribution is superimposed, and the arrowhead indicates the mean spacing position.

a histogram, as shown in Fig. 9.7(c). A lognormal distribution curve is superimposed, which fits the measured frequency curve. Therefore, the dispersion $D_{0.1}$ is calculated using Eq. 9.3a for the lognormal distribution model. The statistics of the measurements are labeled in Fig. 9.7(c). The mean spacing is $\overline{x}$ = 45.0 nm, and standard deviation is s = 39.9 nm, and thus $\overline{x}/s$ = 1.1278. Hence, $D_{0.1}$ = 9.8%, which means about 9.8% spacing data are in the range of 40.5–49.5 nm, or in the range of $0.9\overline{x} - 1.1\overline{x}$.

Another example, the same type of composites but with a less dispersion degree, intercalation, is shown in Fig. 9.8. The platelets are widely spaced because of the lower filler content (2.5 wt.%). The original clay particles are broken up and the clay particles are well dispersed in overall, while aggregations composed of few platelets exist, as shown in the enlargement in Fig. 9.8(b) from the central framed area of Fig. 9.8(a). In order to increase the measurement N, Fig. 9.8(a) is shown in a lower magnification and it is divided by 20 × 20 grid lines to construct the histogram in Fig. 9.8(c). It is seen from Fig. 9.8(c) that the spacing data

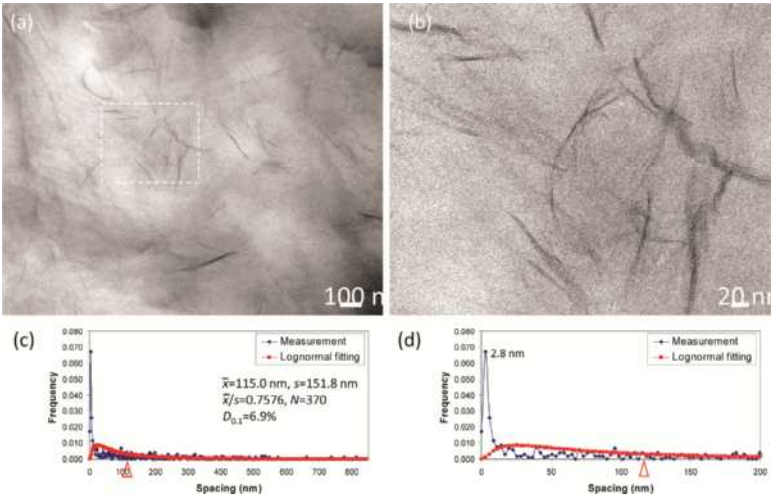

Fig. 9.8 (a) Microstructure of intercalated PA12 with 2.5 wt.% 30B; (b) magnified image from the framed area in (a); (c) layer spacing distance histogram; (d) enlarged histogram from (c) showing the details in the short spacing ranging from 0 to 200 nm. Curve fitting by lognormal distribution is superimposed, and the arrowheads indicate the mean spacing position.

scatter largely. In the short spacing range, as shown in the magnified part in Fig. 9.8(d), a high frequency peak appears at 2.8 nm, which means these platelets within clumps are just slightly opened. The appearance of this sharp peak in the short distance range is an evident indication of the intercalation. Although the peak position depends on the group number of the sampling to plot the histogram, it reflects the high-frequency spacing data in a rough range. The mean spacing is measured as $\overline{x}$ = 115.0 nm with a standard deviation of s = 151.8 nm, and thus $\overline{x}/s$ = 0.7576. Hence, this intercalated example has $D_{0.1}$ = 6.9%, which is lower than the exfoliated dispersion of $D_{0.1}$ = 9.8% in Fig. 9.7.

9.1.4 *Electron Diffraction Pattern Processing and Refinement*

As mentioned in Section 4.3.1 in Volume 1, polycrystals give rise to rings in the selected-area electron diffraction (SAED) patterns, and indexing of such ring patterns is analog to the indexing of powder X-ray diffraction patterns. However, quantification of the ring SAED patterns

can be done if the sample is very thin, such as monodispersed nanoparticles (NPs), based on kinematic scattering theory [14–23].

An SAED pattern from the Au_3Fe_{1-x} NPs is shown in Fig. 9.9(a), which contains both $L1_2$ superlattice and fundamental reflections, as marked by vertical bars above and below the radial horizontal line, respectively [23]. If the SAED pattern is digitalized (or even scanned from negative films), the reflections are displayed as the intensity distributions at each pixel. If it is an 8-bit gray scale image, the intensity range is 0–255. Therefore, on the SAED pattern, first find out its center, and then plot the radical intensity profile distribution. Some programs can produce such radical profiles, such as ELD [14]. Fig. 9.9(b) shows the intensity profile of Fig. 9.9(a), with the center highest intensity recorded as 255 from the direct beam. It is apparent that the center is oversaturated (all center range is at 255). All of the superlattice and fundamental reflections are superimposed upon the high background contributed by the strong center beam. Since the sample is very thin, the center beam is very strong. The background intensity I at 2θ scattering angle can be roughly fit by a power law, that is

$$I = b(2\theta)^c \tag{9.7}$$

where b and c are fitting parameters, which are found to be b = 51.422 and c = –0.89902 by linear regression. The resulting intensity profile after subtracting the background clearly presents the weak $L1_2$ superlattice reflections among the face-centered cubic (FCC) fundamental reflections, as shown at the bottom in Fig. 9.9(b), although the background contribution is not completely removed.

The diffraction data are further processed. Firstly, Pawley refinement [24] is performed on this pattern using the intensity profile in Fig. 9.9(b). After refining all necessary parameters with sufficient cycles, a good fit is achieved, with a weighted profile R-factor R_{wp} = 0.68%, background-corrected weighted profile R-factor R_{wpb} = 4.28%, and profile R-factor R_p = 0.48%, as shown in Fig. 9.9(c). The refinement also outputs fitted background, as shown in Fig. 9.9(c). After subtracting this background, the experimental and simulated reflection intensities, as well as their difference, are plotted in Fig. 9.9(d). The high background,

mainly from the strong center beam, is sufficiently removed. The Pawley refinement can provide accurate lattice parameters from the diffraction data but not atomic positions since atoms are not needed for the algorithm.

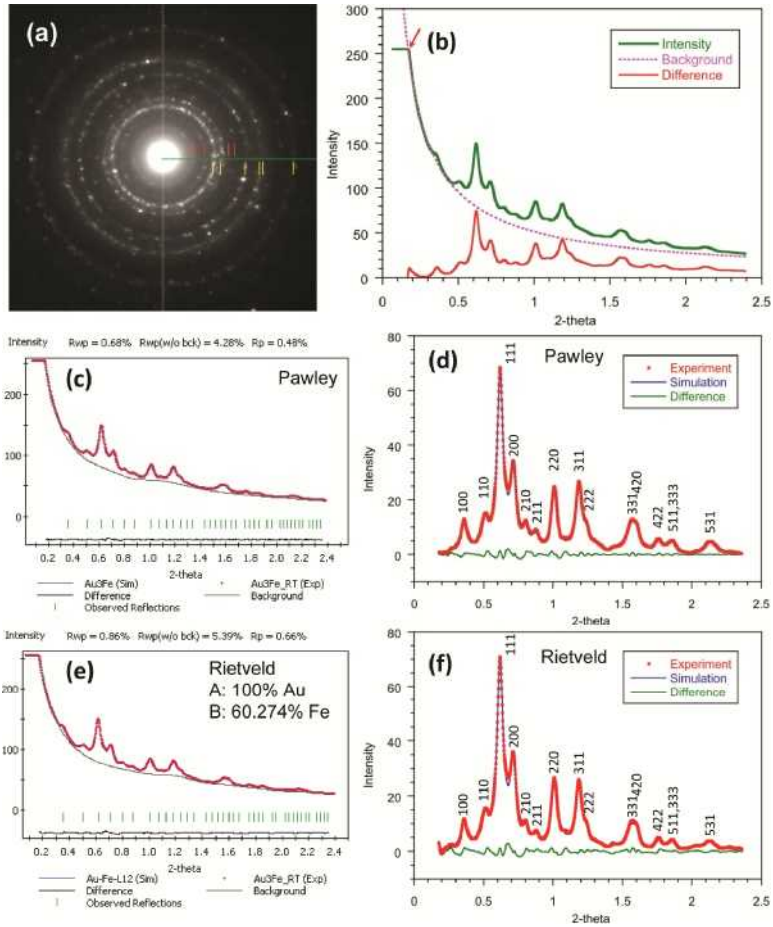

Fig. 9.9 (a) SAED pattern of Au_3Fe_{1-x} at RT; (b) intensity profile, as well as the difference after subtracting the simulated background using the power law as described in the text; (c) the Pawley refinement (refined background is shown); (d) reflection intensities after subtracting the refined background in (c); (e) the Rietveld refinement (refined background is shown); and (f) reflection intensities after subtracting the refined background in (e).

Considering the small particle size, Rietveld refinement [25] is performed, on the base of the refined results available from the previous Pawley refinement, using a kinematical approximation. The refinement results are R_{wp} = 0.86%, R_{wpb} = 5.39%, and R_p = 0.66%, as shown in Fig. 9.9(e). The refined background is also shown in Fig. 9.9(e). After subtracting this background, the experimental and simulated reflection intensities, as well as their difference, are plotted in Fig. 9.9(f). The low *R*-factor of R_{wpb} = 5.39% is an indication for the validity of the kinematical approximation applied for the sample. From the Rietveld refinement, the atomic position, occupation, and lattice parameters are obtained.

It should be mentioned that if the refinement is not required, the background can be simply processed using an algorithm described by Brückner [26], which is implemented in PULWIN1 [26] and Materials Studio Reflex module [27]. There are two parameters to simulate the background [27]:

1. Number of iterations $N_{iteration}$ (defined in the range of 1–100), which specifies the number of iterations to be performed during the background calculation. If this number is too low, the calculation may overestimate the contribution from the background; conversely, if the value used is too high, the calculation may underestimate the background contribution.
2. Averaging window size α_{win} (defined in the range of 0.02–30.0), which specifies the size of the angular region, in degrees, of the experimental powder pattern to be used to determine the background contribution.

Fig. 9.10(a) shows a background processing of the SAED pattern in Fig. 9.9(a) using Materials Studio Reflex default setting ($N_{iteration}$ = 30 and α_{win} = 0.03). It is found that the background is overestimated, as the background curves upward at the peak positions. By increasing $N_{iteration}$ = 300, the background becomes flat under each peak (Fig. 9.10c). However, if $N_{iteration}$ = 5, the background becomes severely overestimated (Fig. 9.10e). The intensity profiles after subtracting the backgrounds are shown on the right side of Fig. 9.10. The peak positions can provide useful information for the phase identifications.

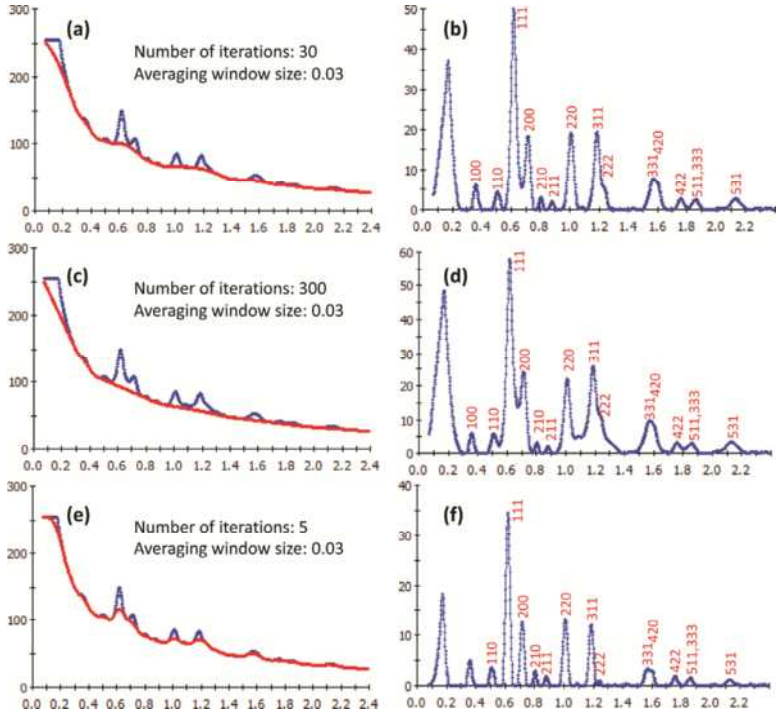

***Fig. 9.10** Background subtraction by Materials Studio Reflex using different parameters of (a) $N_{iteration}$ = 30 and α_{win} = 0.03; (c) $N_{iteration}$ = 300 and α_{win} = 0.03; and (e) $N_{iteration}$ = 5 and α_{win} = 0.03 (c). The intensity profiles after subtracting the background are shown in (b), (d), and (f), respectively.*

9.2 *In situ* Microscopy

In order to study material properties, the materials are subjected to heating, cooling, mechanical deformation, or various irradiations [28–32]. If the samples are processed outside the TEM, it is an *ex situ* experiment. However, some of the experiments can be done inside the TEM chamber as *in situ* experiments, such as heating, cooling, mechanical testing (tensile, compression and nanoindentation), chemical reactions, and electron beam or other source irradiations, with the electron beam illuminated on the specimen to monitor the process.

In this section, practical *in situ* heating, cooling, and irradiation experiments are described.

9.2.1 *In situ Heating*

In situ heating experiment is done using a TEM specimen heating holder. A photo of a holder is shown in Fig. 9.11. The sample is installed in a furnace, which can be heated at high temperatures (most holders can reach or even over 1,000 °C). The furnace is thermally insulated from the holder. There are two pairs of wires. One pair of wires provides power to heat the furnace, and another pair is thermocouple to measure the temperature. During the sample loading or unloading, be very careful for not touching these wires (the wires are easy to break, if they are accidentally hit by tweezers).

The following precautions should be made for the heating experiment:

1. The sample must be solid and does not melt or evaporate at the desired temperature. If glue is involved, the heating temperature cannot be higher than its melting point to avoid contamination on the TEM chamber. Cu grids coated with pure carbon support film can withstand up to 600 °C. If higher temperature is required, use special grids such as silicon nitride (Si_3N_4) support film on Si which can work up to 1,000 °C.

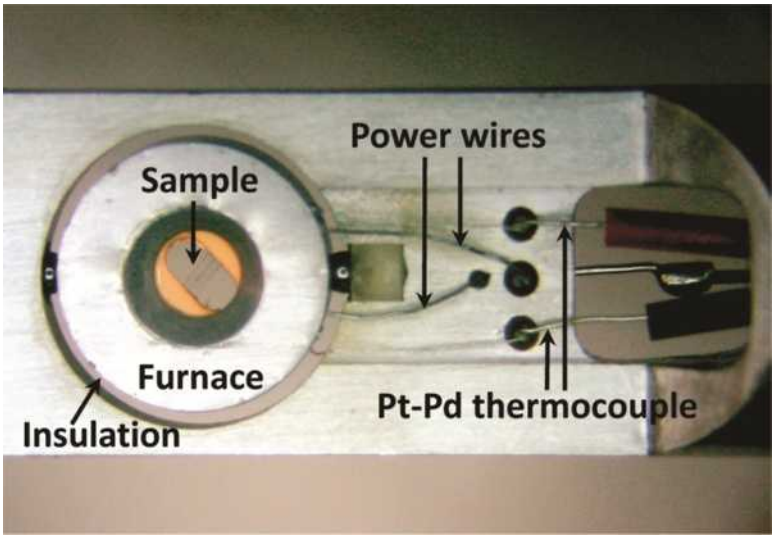

Fig. 9.11 TEM specimen heating holder.

2. Fully retract the X-ray energy-dispersive spectrometer (EDS) detector, if there is, to avoid any possible contaminations. Use high-contrast objective aperture instead of regular objective aperture, if available, to avoid possible evaporated contaminations on the objective aperture since it is very close to the specimen.
3. Design the heating rate and ensure sufficient period of dwell time (5 min or longer) to reach thermal equilibrium at each testing temperature.
4. If the sample drifts, wait for longer time and move the sample in opposite way to minimize the drifting.
5. When the experiment is completed, fully cool down the furnace until it reaches near the room temperature (RT; <30 C) and then remove it out from the column. Removing the holder out when it is hot may cause oxidation problem in the air.

Here, an example of functionalized carbon nanotubes (CNTs) is presented [33]. Fig. 9.12(a) is a TEM image of the original pure CNTs, which exhibit almost clean surfaces, although there are also few attachments on their outer surfaces. However, in Fig. 9.12(b) of functionalized CNT-COOH, processed by reactions with mixed sulfuric and nitric acids (1:1 ratio), evident reactants are found on the CNT surfaces. EDS analysis shows that the CNT-COOH sample contains N, O, and S.

In situ heating of the CNT-COOH sample on silicon nitride support film on Si grid is done using a heating stage, as shown in Fig. 9.13. In order to monitor the size changes during heating, 12 nanotubes are selected to monitor. During the heating experiment, it is found that even

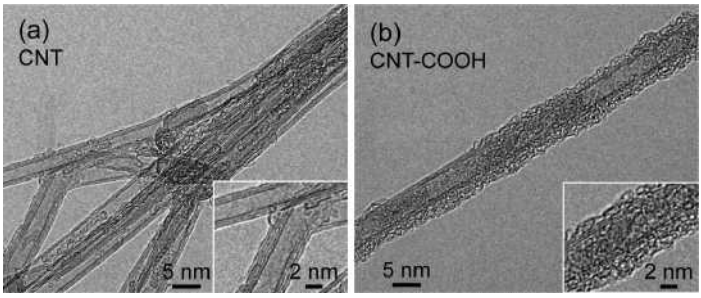

Fig. 9.12 Representative TEM images of the samples CNT (a) and CNT-COOH (b).

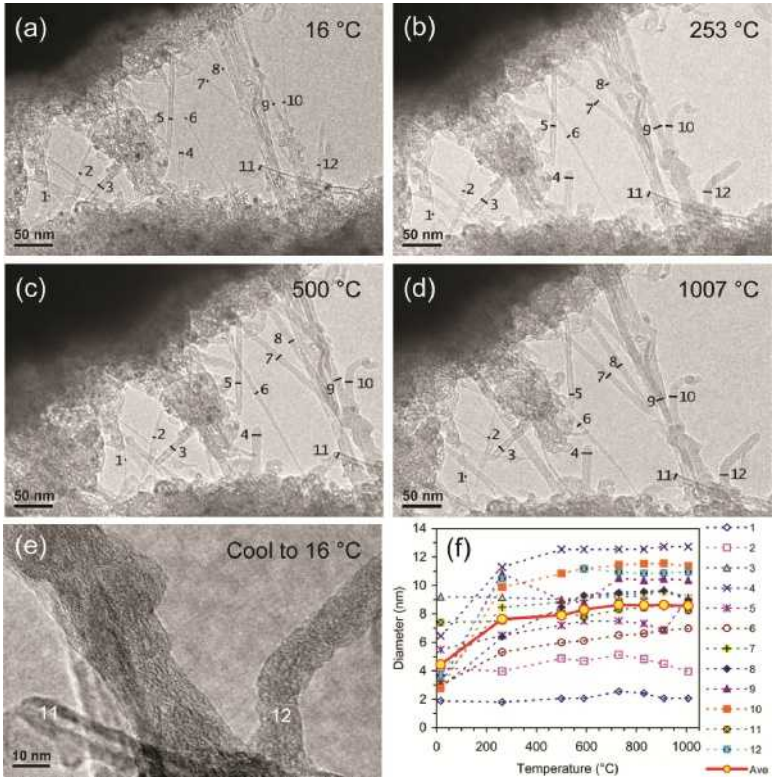

Fig. 9.13 TEM images of the functionalized CNT-COOH sample during in situ heating at RT (a), 253 °C (b), 500 °C (c), 1,007 °C (d), and then cooled down to RT (e). The measured diameters of selected CNTs at different temperatures are plotted in (f).

at a lower temperature (253 °C), most of the nanotubes are significantly expanded, such as 4, 6–10, and 12, indicating that the coalescence happens even at lower temperature. In the following heating process, their diameters continue to grow, while at about 500 °C their diameters keep almost the same size to 1,007 °C (Fig. 9.13c and d). An image after cooling down to RT is shown in Fig. 9.13(e), where it is seen that the nanotubes completely transform to an amorphous state. The measured size variations of selected nanotubes are shown in Fig. 9.13(f). It is seen that size expansion is inhomogeneous. For example, the nanotubes 1 and 2 have less variation compared with others. Their average diameter is increased from 4.5 nm at RT to 7.9 nm at 500 °C, and finally 8.6 nm at 1,007 °C, with the final expansion of about 91%.

Another example of *in situ* phase transformations in In–Tl nanowires (NWs) is shown in Fig. 9.14 [34]. These NWs, with diameters about 15 nm, were deposited on pure carbon support film with Cu grids and heated up and then cooled down in the TEM. The central dark-field (CDF) image at RT (Fig. 9.14a) records thin NWs with the presence of dense martensite twins, with polycrystalline rings in the SAED pattern. The first ring is from (111), followed by double rings of (002) and (200). The intensity profile of this pattern after background removal (refer to the method in Fig. 9.10) is shown in Fig. 9.14(d), which clearly shows the peak positions. At 50 °C and 82 °C, the martensite peaks are still visible, possibly due to the temperature gradient between the specimen holder and the carbon support film, as well as a possible temperature measurement error. However, at higher temperature of 140 °C, as shown in Fig. 9.14(b), the NWs exhibit almost uniform contrast without the contrast of twins, although some diffraction contrast is still visible due to the local orientation variations. From the inserted SAED pattern, the locations of the previous (002) and (200) double rings merge as single (200) ring, indicating the FCC structure. Because of the disappearance of twins in the NWs, the number of crystallites is much reduced and thus

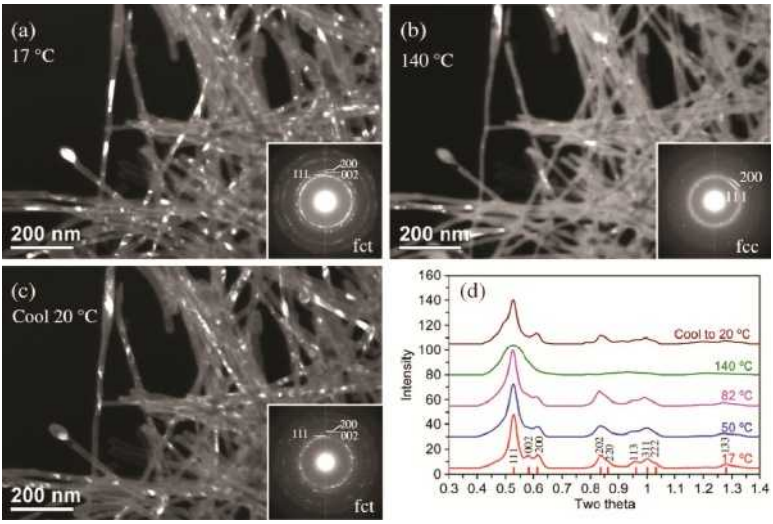

Fig. 9.14 In situ heating of In–Tl NWs from RT (a) to 140 °C (b), and then cooling down to RT (c). The intensity profiles at different temperatures are shown in (d).

fewer reflections appear in the pattern, and the contribution from the amorphous carbon support film becomes more apparent. After cooling down to RT, the twins appear back in the NWs as shown in Fig. 9.14(c). Its SAED pattern indicates the martensitic face-centered trigonal (FCT) structure, as shown in the inset. This suggests that the FCT–FCC transformation in the NWs is reversible. The intensity profiles of all SAED patterns are shown in Fig. 9.14(d) to elucidate the reversible transformations.

The Au_3Fe_{1-x} NPs, whose SAED pattern was previously processed in Fig. 9.9, were *in situ* heated from RT to 633 K using samples on pure carbon support films with Cu grids, as shown with the SAED patterns in Fig. 9.15(a) [23]. It is seen that during heating process the superlattice reflections remain visible up to 523 K, become very faint at 553 K, and then disappear at 593 K. The Rietveld refinements were made on each diffraction pattern, using the procedure described previously in Fig. 9.9. The refined intensity profiles after background subtraction

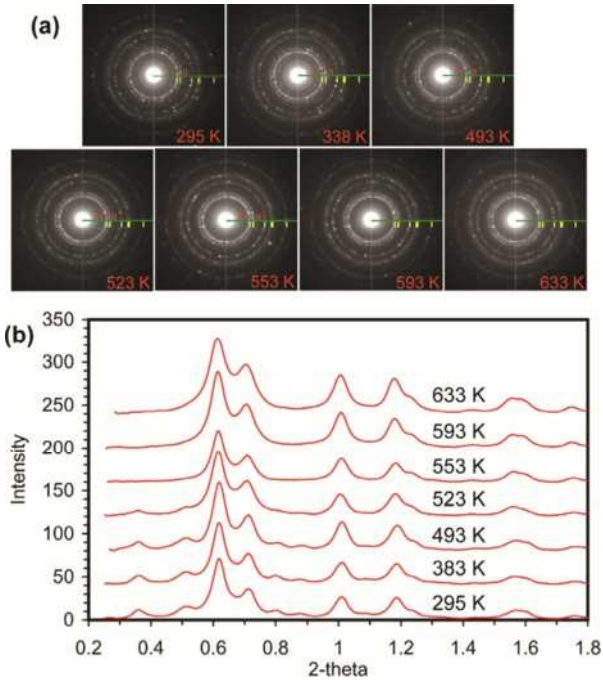

***Fig. 9.15** (a) SAED patterns during the in situ heating process and (b) intensity profiles after subtracting the refined background at each temperature.*

using Rietveld refinements are shown in Fig. 9.15(b). During the Rietveld refinements, the crystal lattice parameters, atomic positions, and occupations could be more accurately determined. Refined lattice parameter *a* is plotted in Fig. 9.16(a). It is seen that the parameter *a* essentially maintains a linear relation with temperature *T* although with the presence of measurement error. A sudden change occurs during the $L1_2$ to FCC order–disorder transition, followed by a linear relationship again. Such linear relationships are fitted with two straight lines, as indicated with arrows. After cooling down to RT, the SAED exhibits only the fundamental reflections without evidence of superlattice reflections, indicating that the order–disorder transition is irreversible. A second heating cycle is made in a similar manner using the disordered sample. The refined lattice parameter is plotted in Fig. 9.16(b). The refined lattice parameter of the disordered sample exhibits a nearly linear relationship with *T*, without a sudden increase as seen in the first cycle. From the atomic occupation of Au and Fe, the long-range order (LRO) parameter *S* is determined, as shown in Fig. 9.16(c). It shows that *S* decreases as a function of temperature *T* and at 593 K, *S* turns to zero to be FCC structure.

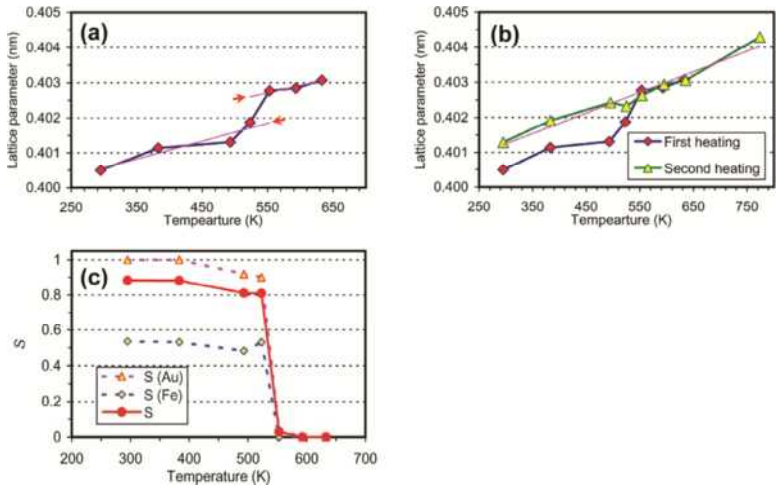

Fig. 9.16 ***(a) Lattice parameter a during the first heating process; (b) lattice parameter a during the second heating process, compared with (a) during the first heating process; (c) LRO S during the in situ heating process.***

9.2.2 *In situ Cooling*

Similar to heating, the samples can be cooled down to low temperatures in the TEM chamber using a cooling holder with liquid nitrogen or helium. The temperature of the TEM specimen, even with the fullest possible cooling settings, however, is indeed higher than the coolants' temperature of –196 °C (77 K) and –269 °C (4 K) for liquid nitrogen and helium, respectively.

The following are the precautions for the cooling experiment:

1. If the sample is dehydrated, it can be installed on the holder first and when it is fully inserted to the TEM chamber, cool the holder down. If it is hydrated sample, the experiment is done using cryo-EM method (Section 9.3). Sample glue can be used, but use thermal conducive glue to ensure the heat transfer.
2. Fully retract the EDS detector, if there is.
3. Design the cooling rate and ensure sufficient period of dwell time (5 min or longer) to reach thermal equilibrium at each testing temperature.
4. If the sample drifts, wait for longer time and move the sample in an opposite way to minimize the drifting.
5. Keep filling the coolant to maintain the required low temperature (controlled by a heating current to reach a certain equilibrium temperature).
6. When the experiment is completed, pour out the remaining coolant and warm up the holder to near the room temperature and then take it out. Removing the holder out when it is still cooled will result in condensed moisture on the holder surface causing contaminations.

In Chapter 4 in Volume 1, an example of *in situ* observation of charge ordering (CO) transformation in an $Nd_{0.5}Sr_{0.5}MnO_3$ CMR sample cooled by liquid nitrogen is given in Fig. 4.14 [35]. Such *in situ* observation was made on the same area during cooling down and warming up processes. *In situ* cooling of $La_{2-2x}Sr_{1+2x}Mn_2O_7$ (x = 0.6) was also conducted [36, 37], and the electron diffraction patterns and high-resolution TEM (HRTEM) images at the low temperatures were recorded to construct a CO model

[36]. As shown in Fig. 9.17(a), at room temperature only fundamental reflections appear. At intermediate temperatures, sharp superlattice spots appear, which then fade and disappear at low temperatures. The intensity profiles across the centerline of the diffraction pattern are shown in Fig. 9.17(b). The average intensities of these CO reflections are plotted as a function of temperature in Fig. 9.17(c), where they are compared with transport measurements of electrical resistance. The lowest temperature reached 23 K (−250 °C) using liquid helium cooling.

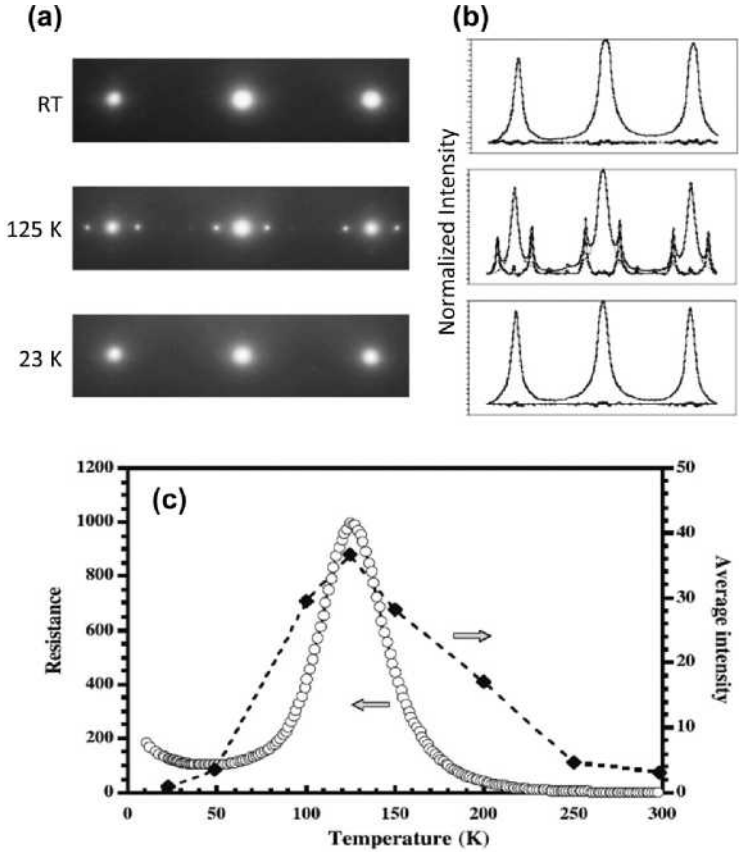

Fig. 9.17 Electron diffraction results for a $La_{2-2x}Sr_{1+2x}Mn_2O_7$ (x = 0.6) sample. (a) SAED patterns at RT, 125 K, and 23 K showing the appearance of long-range CO at intermediate temperatures; (b) normalized line scans through the centerline of the corresponding patterns in (a); (c) temperature dependence of the superlattice reflection intensity showing the correlation with electrical resistance.

9.2.3 *In situ Irradiation*

The TEM specimen can be subjected to various high-energy ions or electrons irradiations for *in situ* observations [38–45].

Fig. 9.18 demonstrates *in situ* electron beam irradiation of PbTe high-density amorphous (HDA) phase obtained from high-pressure deformation [45]. The *in situ* TEM observation was made upon a gradual increase of the irradiation dose of electron beam. The initial state is amorphous. Upon irradiation of the area using a very weak electron beam (we suppose that the electron dose of this pattern is close to 0 e/nm^2), an SAED pattern was immediately taken after the specimen was moved to the recording area (Fig. 9.18a). The pattern showed only a broad diffuse scattering ring, indicating an amorphous structure. Upon

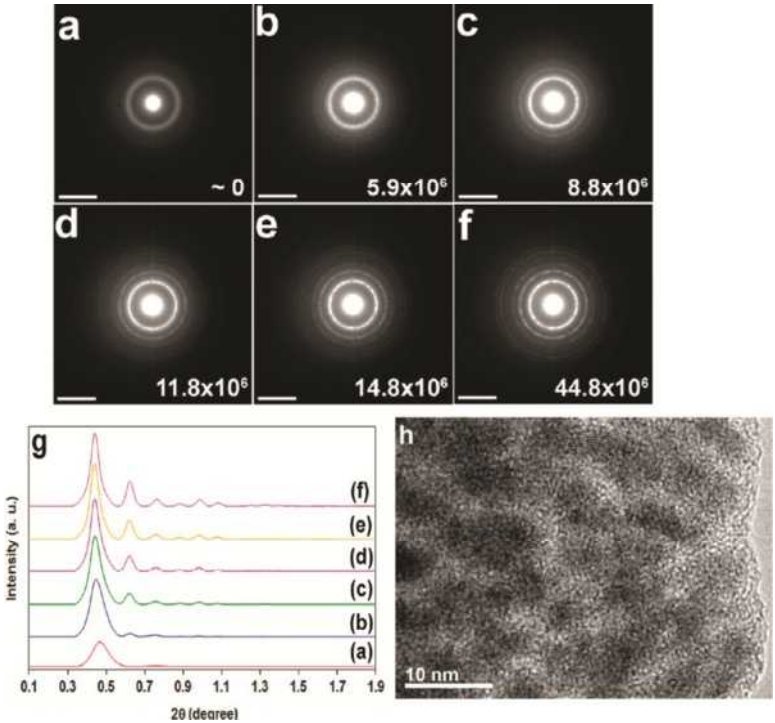

Fig. 9.18 (a–f) In situ SAED patterns of PbTe NPs with the increase of electron dose level; (g) intensity profiles of SAED patterns; (h) HRTEM image of PbTe NPs directly obtained after the electron irradiation dose of 27.2 × 10⁶ e/nm².

irradiation of an electron beam with increased dose, a series of SAED patterns were sequentially taken (Fig. 9.18b–f). At the 5.9×10^6 e/nm^2 level (Fig. 9.18b), PbTe NPs started to crystallize but still showed weak diffraction rings. These electron diffraction rings became gradually stronger (Fig. 9.18c–f). When a dose level of 8.8×10^6 e/nm^2 was achieved, the crystallization was complete (Fig. 9.18c). Note that this sample was very sensitive to electron irradiation. In order to monitor the process of crystal nucleation and growth, HRTEM images could not be taken as they required high dose levels of electron beams. Only in the final crystallization stage of the sample exposed at 27.2×10^6 e/nm^2, it was able to obtain an HRTEM image (Fig. 9.18h), which shows well-developed lattice fringes. One additional SAED was taken for the sample exposed at a higher dose of electron beam (Fig. 9.18f). To compare the intensity change, all of the SAEDs were processed with a background subtraction. The results are shown in Fig. 9.18(g), indicating that the crystallization developed gradually as a function of the electron beam dose.

9.3 Cryo-EM

Because of the high-vacuum level inside the TEM chamber, the liquid samples cannot be inserted to the TEM directly, but they can be frozen first. Cryo-EM is developed to work with the hydrated samples [46–50]. The major procedures of cryo-EM are described as follows.

(a) Sample Preparation

1. The sample concentration must be high enough (5–10 times of the regular TEM sample concentration). Examine samples at room temperature (directly dried on grids) first to ensure the correct concentration.
2. Prepare liquid ethane (C_2H_6), whose melting point is −182.3 °C and boiling temperature is −88.5 °C. If the temperature is controlled in the range of −182.3 to −88.5 °C, the ethane retains liquid. In the beginning, dry the cup setup completely using a hair dryer to eliminate moistures, and then place it into liquid nitrogen to cool down thoroughly. Open the main ethane tank valve and adjust the flow of ethane gas to a gentle stream. Start liquefying the ethane in

the central cup. Keep the tip of the ethane hose close to the walls of the cup to allow faster condensation. Continue filling the ethane cup until it is full (just below the spider). Once the liquid ethane is made, it should be used as soon as possible. If the ethane freezes, use the ethane gas to thaw it back into a liquid. The prepared liquid ethane should be clean and free of frost ice pellets (Fig. 9.19a). Close ethane valve when it is done. (Note: Ethane is flammable, so proper ventilation is required.) Place a cooled grid box to store the specimens to be prepared. The grid box should be thoroughly covered with the liquid nitrogen.

3. The preparation device by FEI Vitrobot is shown in Fig. 9.19(b). The humidity of the chamber is controlled to a desired level (typically 100%). Two pieces of new filter papers are installed. In the meantime, place several grids in a glow discharge chamber to glow discharge them, and then install a piece of grid on the arm. Install a glow-discharged grid in the chamber.

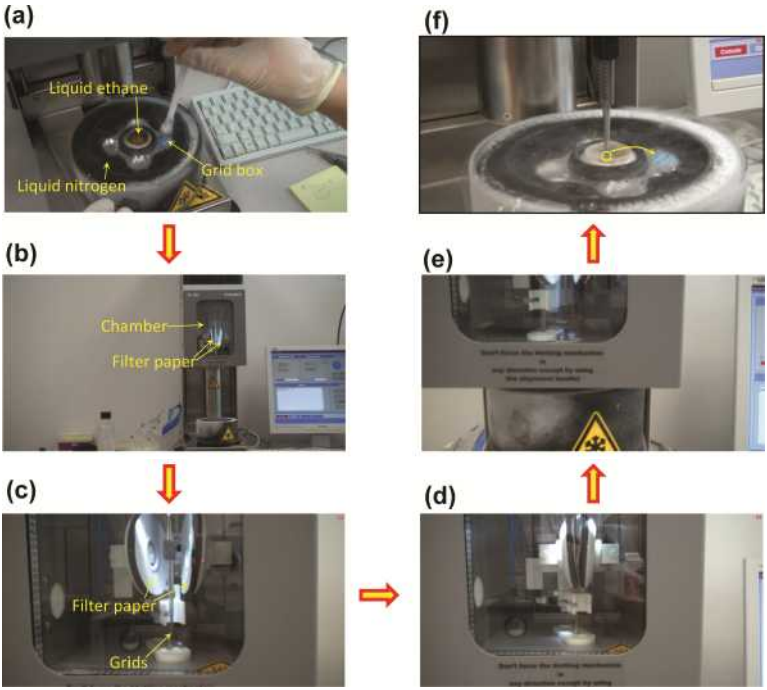

Fig. 9.19 Procedures to prepare cryo-EM samples using plunge freezing method (photos are taken from snapshots, in a sequence labeled as a–f, from a recorded video).

4. When the process starts, the cup moves up until it reaches the bottom of the chamber. Open the slider door and use a pipettor to dispense 2–5 μL of the liquid sample onto the grid. Close the slider door and wait for some time (30 s) if needed (Fig. 9.19c).
5. Follows is the blotting process (Fig. 9.19d). Once the process is completed, the Vitrobot arm will quickly move down, so the grid is dipped into the liquid ethane under the chamber (Fig. 9.19e). The cup and the arm with tweezers and grid then move down simultaneously.
6. When the cup and arm reach to the bottom base (Fig. 9.19f), free the tweezers from the arm and quickly move the grid from liquid ethane to the grid box in liquid nitrogen. Be careful for not losing or damaging the grid (sufficient practices are needed). Continue to freeze the next grid. When the grid box is full, store it in a liquid nitrogen dewar.
7. When all samples are done, follow the Vitrobot shutdown procedures.

Some details about the plunge freezing process are illustrated in Fig. 9.20. Start with a holey grid film (Fig. 9.20a), and a drop of liquid is deposited onto the film (Fig. 9.20b). During the blotting process, two pieces of filter papers touch on both sides of the grid, and thus extra liquid is absorbed while the liquid still remains in the holes (Fig. 9.20c). The grid is then quickly dipped into liquid ethane (Fig. 9.20d) to freeze the liquid on the grid. This grid with frozen sample is then quickly moved to the grid box for the next step.

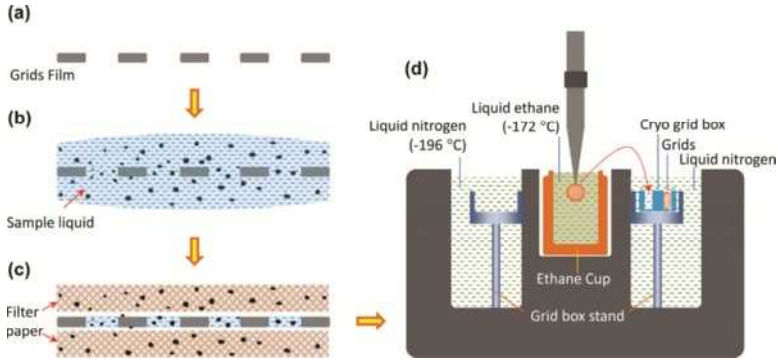

***Fig. 9.20** Schematic plunge freezing process. (a–c) Cross-sectional views of a grid; (d) transfer of the grid from liquid ethane to grid box in liquid nitrogen.*

(b) Transfer to the Specimen Holder

1. Place the cryo-holder in the cryo-transfer station.
2. Fill liquid nitrogen to the holder's dewar and transfer station. Wait for the temperature to reach the lowest level (~ −193 °C).
3. Cool down a pair of dried tweezers and the clip-ring tool.
4. Open the shutter of the holder, move the grid from the grid box to the holder, and ensure the sample is placed on the right location with the sample film side on the upside (in the TEM it also on the upside). Ensure it lies on a flat position and is centered. Secure the ring on the rod and close the shutter for the next step.

(c) Transfer to the Microscope

1. On the microscope, prepump the airlock and set the stage angle at –60°, so that the holder (with liquid nitrogen filled) can be inserted without tilting to a large angle to keep some amount of liquid nitrogen in the dewar.
2. Quickly remove the holder from the transfer station and insert into the pre-pumping position in the microscope.
3. When the pumping is completed, insert the specimen holder.
4. Fill liquid nitrogen to the dewar. Check the temperature that should fall to ~−172 °C. Check again every 2 h to ensure sample is at the correct temperature and fill liquid nitrogen as needed.
5. Wait for the column vacuum to stabilize (~10 min). Only when the column pressure reaches allowed level of the instrument, open the column valve. Open the shutter on the holder for observation.
6. During the observation, use relatively weaker beam and lower magnifications. At higher magnifications (80,000× or above), the electron beam heats the sample due to the increased electron dose, so the ice starts to melt and evaporate to form holes. In this case, use low-dose imaging method for imaging at high magnifications (refer to Section 9.4).

7. When the experiment is completed, close the microscope column valves, reset the holder positions, pull off remaining liquid nitrogen in the dewar, and warm up the holder to RT before taking it out of the TEM column.
8. After each use of the holder, bake it at 100 °C for a long time (~10 h) for the next use.

If the plunge cooling speed is high enough, the ice appear as vitreous (amorphous) ice, which exhibits as continuous background (Fig. 9.21a). However, if the sample is not prepared correctly, crystalline ice particles appear (Fig. 9.21a and b), which disturb the observation.

Fig. 9.22(a) shows hydrogel-forming peptide nanofibers prepared by the cryo-EM method [51]. In this hole, the ice appears as vitreous ice background, and the fibers are frozen in the ice. An enlarged image is shown in Fig. 9.22(b). After long-time observation, or if the electron beam is focused on a spot, it is possible to observe that the ice starts to melt and evaporate by appearing small holes. In fact, some small holes can be found in Fig. 9.22(b). Lipid vesicles can be studied by the cryo-EM [46, 49, 52]. Fig. 9.22(c) shows spherical lipid vesicles in vitreous ice, with few crystalline ice particles presented. The enlarged image is shown in Fig. 9.22(d). These particles are well preserved in their original status for the TEM observations.

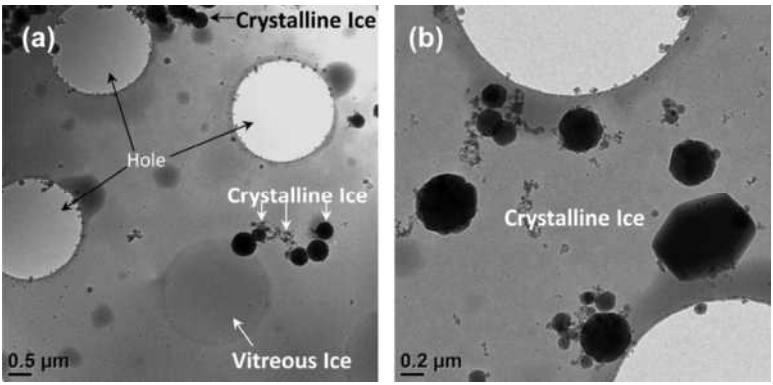

Fig. 9.21 (a, b) Two examples of vitreous ice and crystalline ice.

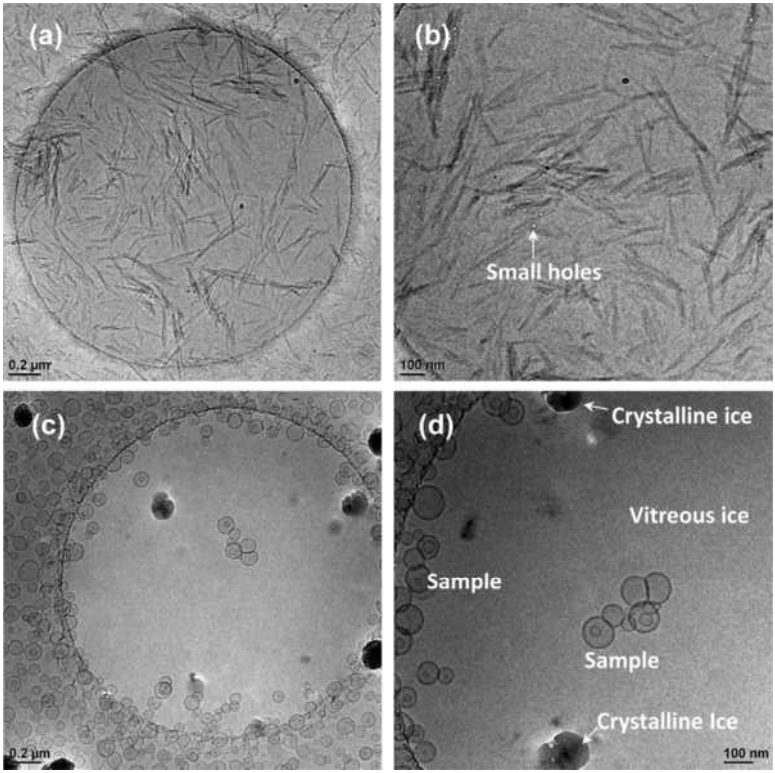

Fig. 9.22 Cryo-EM images of hydrogel-forming peptide nanofibers (a, b) and lipid vesicles (c, d).

9.4 Low-Dose Imaging

For electron beam-sensitive materials, it is difficult to record structural images without any beam damage on them. Even under very weak beam, once the area is found and immediately the photo button is pressed (or clicked in the computer screen), few seconds have passed by the recording starts. The low-dose imaging is developed to overcome this problem [53–56]. As shown in Fig. 9.23, it comprises three modes:

1 Search mode, which is at a low magnification for a large view. Select an interested area and move it to the center. Since the magnification is low and a large area is exposed, the interested area is exposed only to a very low dose level of electrons (typically <1 $e/\text{Å}^2/\text{s}$).

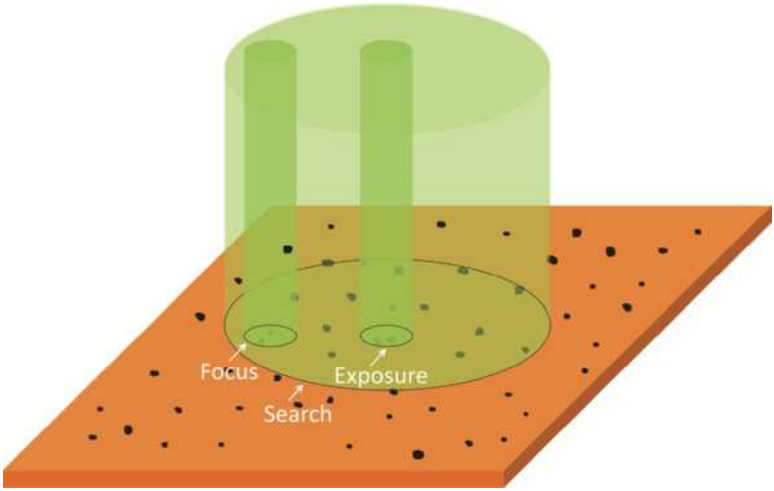

Fig. 9.23 Low-dose imaging principles.

2. Focus mode, which is at the high magnification but the beam is deflected away from the interested area, so that the user can take time to focus it well without any hurry. Normally two focus areas can be defined by the user, as they should not overlap with the specimen of the interested area to avoid damage on it.
3. Exposure mode, which is at a high magnification to expose the interested area using the focusing and brightness conditions defined in the previous Focus mode. The beam remains blank until the Exposure mode starts, it opens for a short period of time defined by the user (normally 0.5–2 s), and then it blanks again to protect the specimen.

In such an imaging mode, the interested area is exposed only to a short period of time defined by the user to minimize the beam damage. Note that image is still recorded with sufficient illumination intensities to get high-quality signals rather than very weak intensities, but any unnecessary time is cut off.

To measure the electron dose in the Exposure mode, retract the specimen (no specimen in the view) and take an image with 1 s exposure. Measure the mean counts of the exposure and the dose level of the current illumination.

Fig. 9.24 shows examples of virus particles prepared using cryo-EM. Since these particles are very sensitive to the electron beam, low-dose mode was used to record them. If the exposure time is 1 s, the electron dose is calculated as 20 $e/Å^2$, and the image is dark (Fig. 9.24a). If the exposure is increased to 1.5 s, the dose is at 30 $e/Å^2$, the particles exhibit higher brightness and contrast, as shown in Fig. 9.24(b). However, if the exposure time is increased to 3.5 s, the dose reaches 70 $e/Å^2$, and damages have occurred, as circled in Fig. 9.24(c). Correct dose level should be carefully selected for a specific sample.

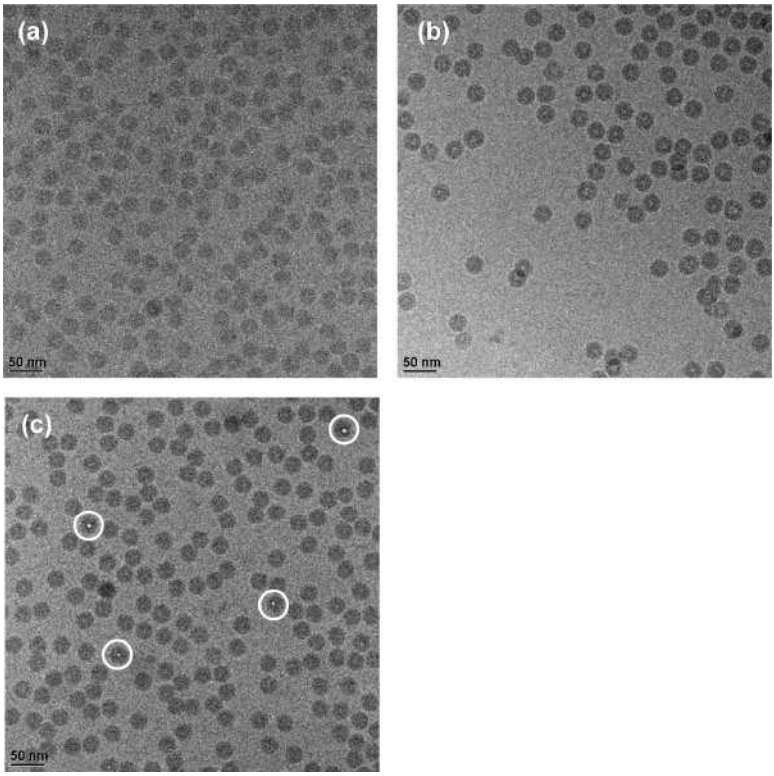

***Fig. 9.24** Cryo-EM images recorded in low-dose mode. (a) 20 e/Å² (exposure: 1 s); (b) 30 e/Å² (exposure: 1.5 s); 70 e/Å² (exposure: 3.5 s).*

9.5 Electron Tomography

9.5.1 *Experimental Procedures*

A single TEM image provides only 2D information on the project from a 3D sample. To overcome this 2D problem, ET is developed [57–65]. The ET procedures are illustrated in Fig. 9.25, including the following steps:

1. Data acquisition. The TEM sample is tilted to the highest possible degree until the view is blocked or limited by the instrument, normally from −70° to +70°, depending on the sample geometry, specimen holder, and microscope configuration. The number of images between +tilt and −tilt can be different while ensuring the tilting range is at the full possible range to record more images. The angle increment is normally set as 1° or 0.5°. The obstacle for the acquisition is the sample drift during tilting. Therefore, the sample holder should be previously well calibrated. The calibration is done using small NPs in high contrast, such as fiducial markers, so that any drift at each angle is recorded, which is thus compensated for the real sample at that angle.
2. Data alignment. Even for a set of data acquired from a well-calibrated holder, the images still shift at different angles. The alignment process is done to align these images. This step should be repeated, sometimes for many times, until satisfaction is reached. After the alignment, the images translate smoothly when they are displayed as a movie.
3. Data reconstruction. After the alignment, the data reconstruction is done using the aligned data. This is a mathematic process, which is straightforward using existing computing programs.
4. Object rendering. After the reconstruction, visualize and render the reconstructed volume, such as slice views or 3D isosurface.

A series of representative TEM images during tilting are shown in Fig. 9.26. The sample was tilted from 0° gradually to 50°, and then returned back to 0° and continued to tile to −50°. The sample drifted slightly during the tilting. Although it is evident that the NPs appear as

different projections after tilting, without reconstruction it is impossible to tell the 3D structure of these NPs. After the 3D reconstruction, 3D information is obtained, which will be given late (in Fig. 9.33).

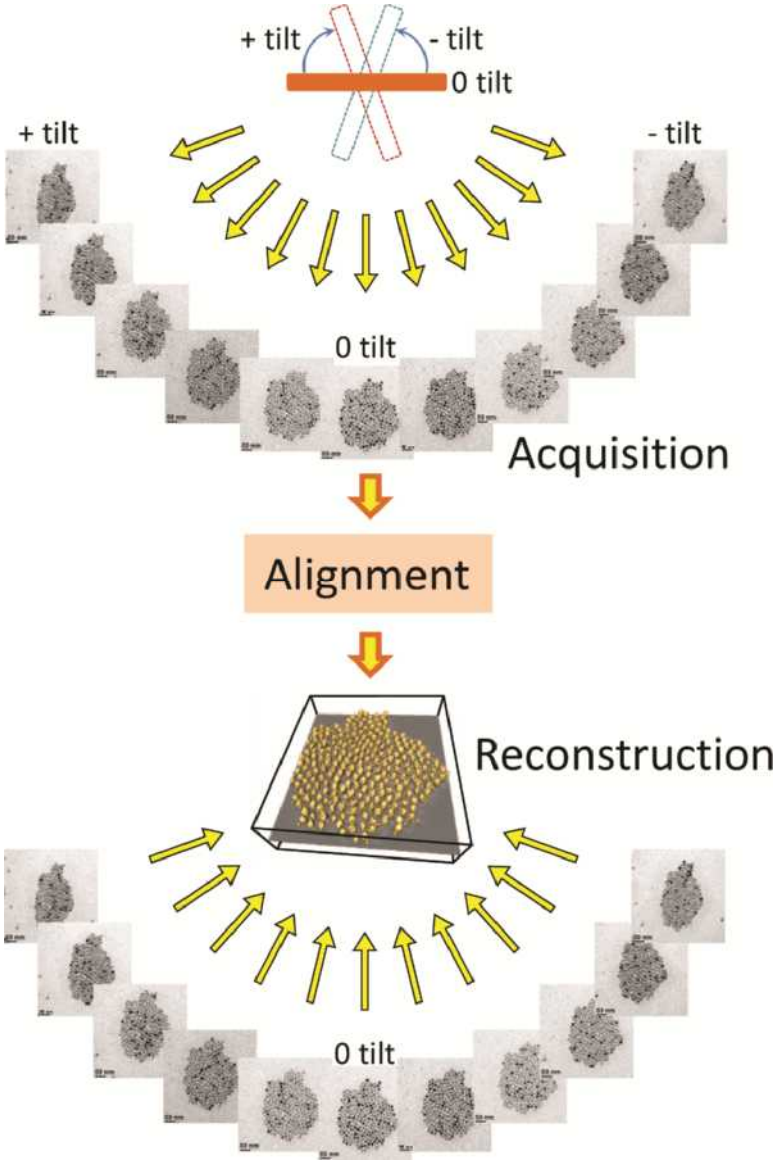

Fig. 9.25 Electron tomography procedures of data acquisition, alignment, and reconstruction.

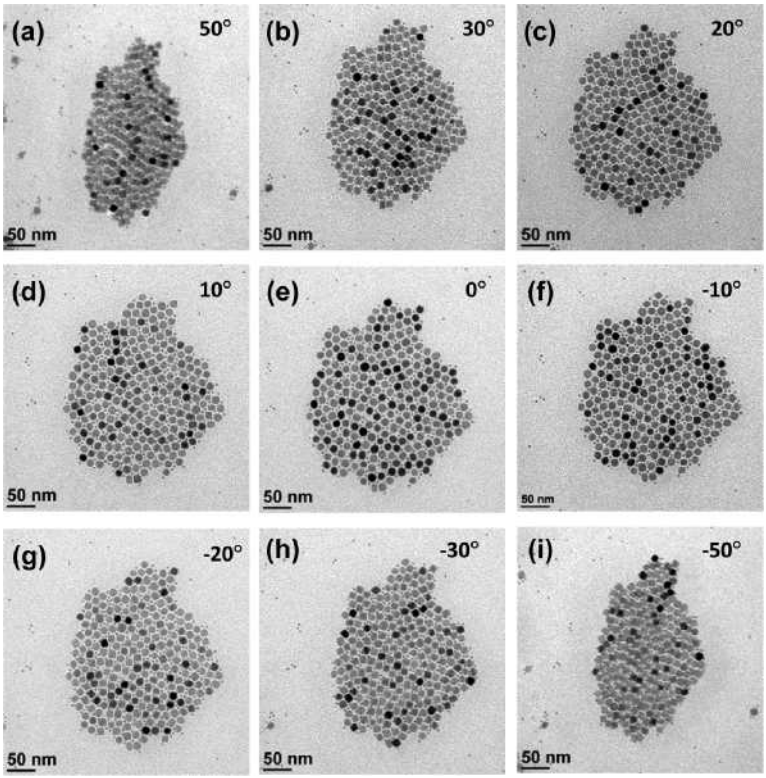

Fig. 9.26 A series of representative images obtained by tilting. (a–e) Images tilted to positive angles; (e–i) images tilted to negative angles.

The images for tomography can be taken in TEM mode, STEM mode, and even elemental maps although it would take very long time to get a large number of images.

9.5.2 Object Shapes

A major advantage of ET is its capability to investigate the object 3D shape. A single TEM image provides a projection only from the top view. However, once the reconstruction is completed, it is possible to view the object from any views by rotating the reconstructed volume, or by slicing it to get intersections [66–68].

As an example, two types of Ni_3S_4 NPs, rod shaped and triangle shaped, are shown in Fig. 9.27(a) and (b), respectively. From a single TEM image, it is impossible to tell what their 3D shapes are. Therefore, ET was used to study their shapes [66].

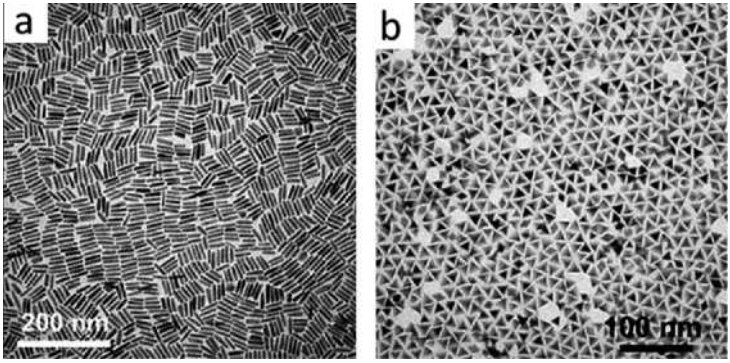

Fig. 9.27 Ni_3S_4 NPs with rod (a) and triangle (b) shapes.

An area containing several tens of Ni_3S_4 nanoprisms, as shown in Fig. 9.28(a), is selected for ET. Note that the areas in Fig. 9.27(a) or (b) are not suitable for ET, since the features are similar; so tracking may be lost during the tilting. The reconstructed volume is shown in Fig. 9.28(b), displaying two perpendicular sections. It is found that these nanorods are indeed nanoprisms. As a comparison, a model with two simulated prisms exhibiting cross sections is inserted with each Ni_3S_4 nanorod ending with a triangular cross section. Interestingly, two triangles for most adjacent "rods" are standing oppositely on the TEM film (marked rectangle in Fig. 9.28b), likely due to strong face-to-face interactions. Three typical cross sections parallel to the imaging plane through the 3D reconstruction are shown in Fig. 9.28(c–e). A cartoon demonstrating the corresponding cross planes of prisms is given below each figure. Fig. 9.28(c) shows the cross-sectional view near the top of the reconstructed volume. The width of the bright "rod" (marked area with a square on Fig. 9.28c) is ~4 nm. The width of the "rod" increased to about 8.2 nm at the middle cross section plane (Fig. 9.28d) and about 11.5 nm near the bottom cross-sectional plane (Fig. 9.28e). Based on these results, it can be deduced that the edge length of the nanoprism is of ~12 nm. Moreover, it is noted that for the adjacent nanoprism, in both marked areas, an opposite trend is observed, where the width of the "rod" decreases as the numerical cross-sectional plane increases. These results show that the Ni_3S_4 "rods" are actually triangular nanoprisms, and two adjacent nanoprisms are lying reversely on the TEM grid in an energetically favored way due to the maximized van der Waals interactions arising from the face-to-face orientation.

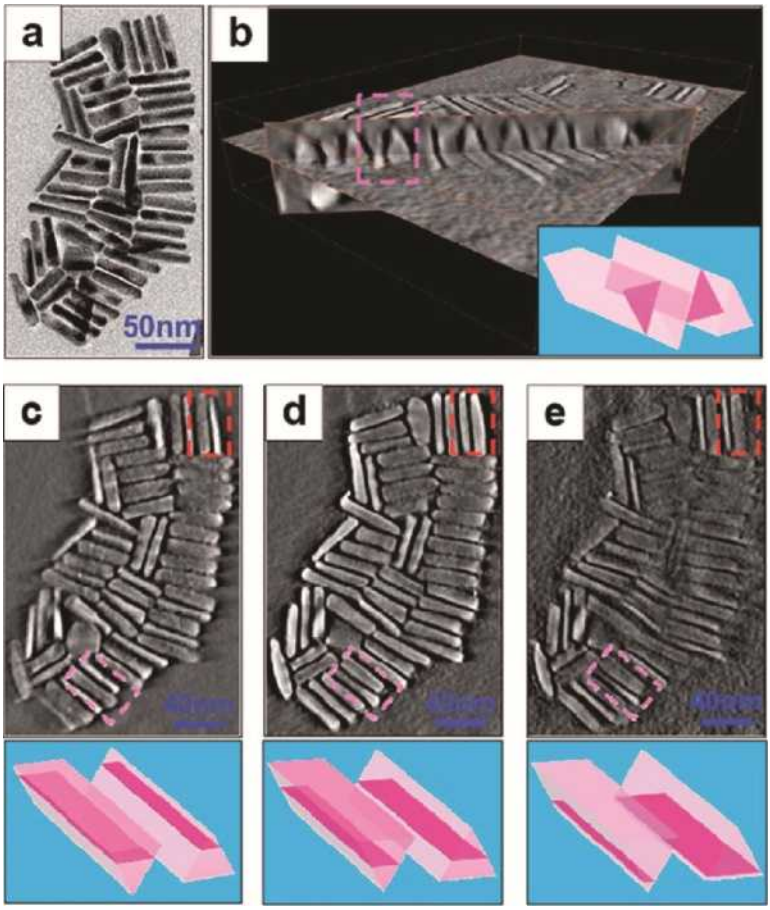

Fig. 9.28 ***Ni_3S_4 nanoprisms. (a) TEM image; (b) reconstructed 3D tomographic cross section; (c–e) cross-sectional planes at different heights of the reconstructed volume. Insets: schematic representation showing variable cross sections at different heights.***

The triangular shaped Ni_3S_4 NPs were also examined with ET. The area as shown in Fig. 9.29(a) is selected for ET. Three typical cross-sectional planes through the 3D reconstruction parallel to the imaging plane are shown in Fig. 9.29(b)–(d), along with cartoons demonstrating the corresponding cross planes of a pyramid viewed at different positions. The triangles, as indicated by a circle, show different sizes on the intersecting plane. In Fig. 9.29(b), the triangles show an average side length of 16 nm. At a cross-sectional plane at the middle height of the reconstructed volume, as shown in Fig. 9.29(c), equilateral triangular

shapes are at the same location (pointed by an arrow) but with smaller side length, about 10.5 nm. As the viewing plane further moves down, the equilateral triangle shown at the same location is even smaller with the side length of ~6 nm. This is also a representative shape at this plane. The proportional variations of equilateral triangle in size at different cross-sectional planes confirmed that the Ni_3S_4 particles synthesized have a tetrahedral pyramid shape. Interestingly, the decrease in size for most of the nanopyramids as the cross-sectional planes come closer to the TEM grid indicates that the Ni_3S_4 pyramids are standing on the tip over the grid. Fig. 9.29(e) shows the 3D isosurface top view where the bottoms of the nanopyramids are observed in most of the cases, and Fig. 9.29(f) is the side view of the assembly showing assembled NPs standing on the carbon film on their tips, while few isolated NPs on the backside of the carbon film attaching on their faces. This phenomenon (tip down standing) is energetically unfavorable, probably due to the strong interactions between NP tips.

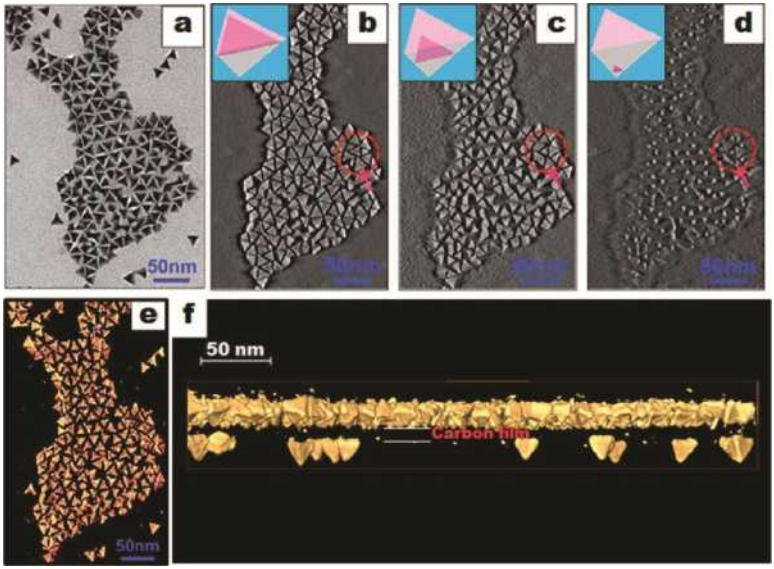

Fig. 9.29 ***Ni_3S_4 nanopyramids. (a) TEM image; (b–d) slices of the reconstructed volume at top (b), middle (c), and bottom (d) positions; (e) top view; (f) side view. Insets: schematic representation of the nanopyramids.***

Fig. 9.30(a) is a TEM image of $CuInSe_2$ NWs with saw-tooth shapes [67]. An HRTEM image is shown in Fig. 9.30(b), with two different indicated regions of the NW magnified in Fig. 9.30(c) and (d), respectively. These two regions exhibit a twinning relationship around the growth axis with ~60° rotation about the common (112) plane. Many NWs show a saw-tooth-like surface along the growth axis.

In order to examine the morphology of the NWs in more detail, STEM images and a 3D ET were obtained. Fig. 9.31(a) shows a STEM *Z*-contrast image of a NW with saw-toothed surface, which clearly shows the triangular shapes stacked along the NWs. ET is conducted using the TEM mode. Cross-sectional views at two selected positions of

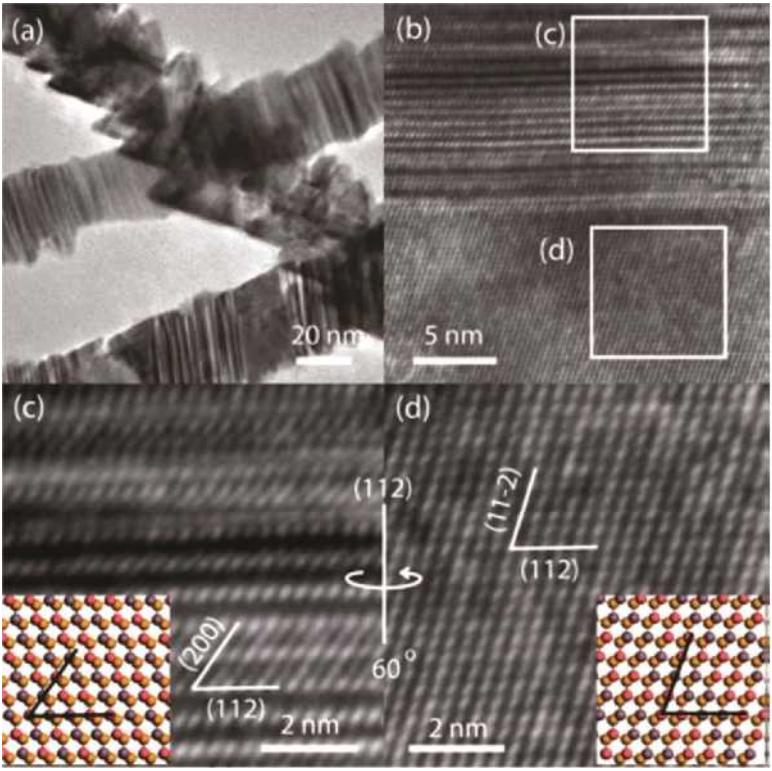

Fig. 9.30 (a) Representative TEM image of NWs; (b) HRTEM image; (c, d) magnified HRTEM images from the areas indicated in (b). Insets of (c–d) are structural models.

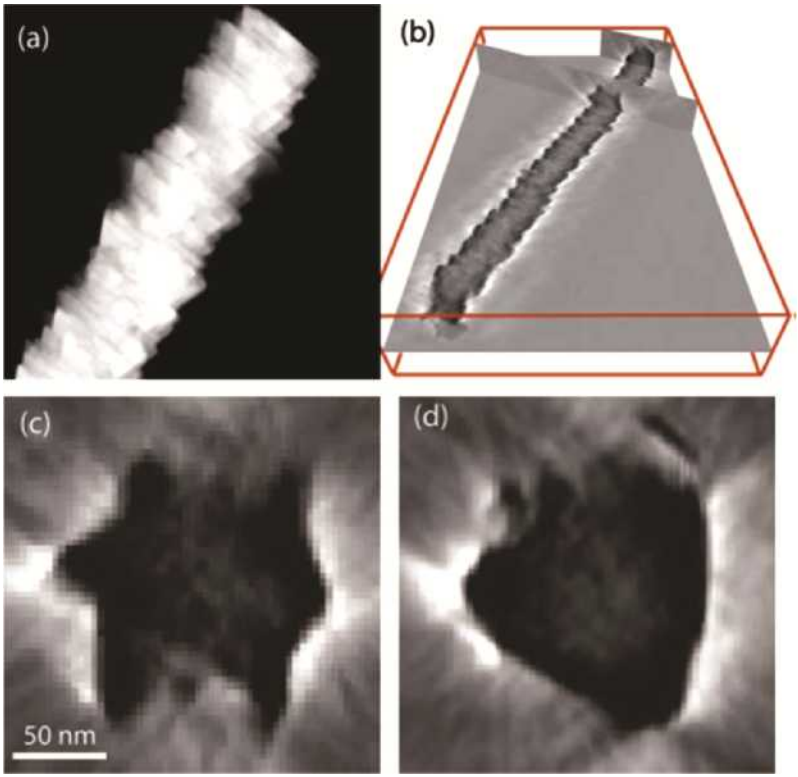

Fig. 9.31 (a) STEM image of a NW; (b) two locations of on a NW where cross-sectional views are obtained; (c, d) cross-sectional views of the NW in (b).

the reconstructed volume, as indicated in Fig. 9.31(b), are shown in Fig. 9.31(c) and (d). Two superposed triangles and a single triangle are clearly identified, as shown in Fig. 9.31(c) and (d), respectively. The orientation relationship between the cross sections shown in Fig. 9.31(c) and (d) clearly indicates the twinning with a ~60° rotation, consistent with the twinning of the lattice observed in HRTEM images of the NWs in Fig. 9.30. While moving along the growth axis of the NW, all the identifiable triangular cross sections were oriented in the same or ~60°-rotated directions. These observations indicate that the morphology of the NW can be viewed as a stack of truncated tetrahedra with occasional rotations of a tetrahedron unit by ~60° around the growth axis.

9.5.3 *Nanoparticle Assemblies*

Since the ET can reveal the 3D structure of NPs, it can be used to study the NP assemblies. As shown in TEM projection images (Fig. 9.32a and b), the sample contains large In_2O_3 octahedral NPs and small spherical Pt NPs [69]. Two types of individual In_2O_3 and Pd structures were observed. In Fig. 9.32(a), the In_2O_3 nanoctahedra are <001>-projected and orientated by sitting on their vertices. The Pd NPs are inserted at positions that close to four vertices from the four nearest-neighbor In_2O_3 nanoctahedra. Interestingly, Fig. 9.32(b) reveals the second type of packing arrays. The In_2O_3 nanoctahedra, projected in <110> orientation, sit on their edges, that is, slightly truncated (110) facets.

Fig. 9.33(a) presents a 2D binary NP superlattices (BNSL) area selected for the ET. A series of images at different angles are taken and they are then reconstructed by the back-projection method using FEI Xplore3D program. Fig. 9.33(b) shows a reconstructed volume that was rendered using isosurface, indicating NPs that are consistent with those observed in the real TEM image in Fig. 9.33(a). Using this reconstructed volume, it is possible to visualize the pattern at any angles. In order to determine the relative positions of Pd NPs to In_2O_3 nanoctahedra, it is necessary to tilt this volume to the edge-on angle (perpendicular to the electron beam). Fig. 9.33(c) and (d) are two representative side views, near and at the edge-on positions, respectively. It is clear that most of the Pd NPs locate on the middle plane of the In_2O_3 nanoctahedra, apparently well above the substrate surface (support film) rather than sitting on it. Note that in this area, few Pd NPs are found on another side of the support film, and thus two planes are shown in Fig. 9.33(c) and (d), depicting the top and the bottom surfaces of the support film. Supposing the bottom few Pd NPs attach the support film due to the absence of charge on this side, the support film thickness is estimated as 17 nm.

Based on experimental observations, the BNSL assembly models are proposed in Fig. 9.34(a) and (b), corresponding to the observations in Fig. 9.32(a) and (b), respectively. The coordination number of Pd NPs around a In_2O_3 nanoctahedron is ultimately dependent on the packing orientation of the In_2O_3 nanoctahedron.

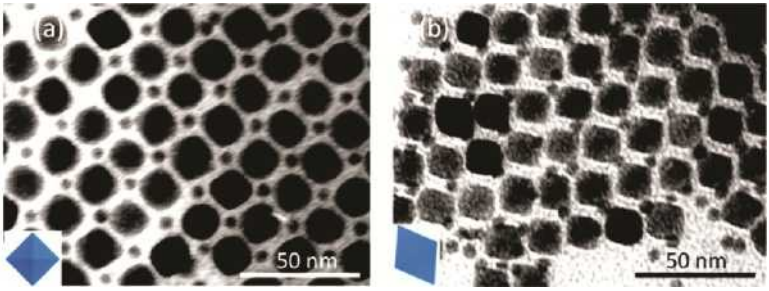

Fig. 9.32 TEM images of binary assembly structures formed between In_2O_3 nanoctahedra and Pd NPs. (a) Type-I assembly, the nanoctahedra oriented along <001>, as indicated by the inserted model; (b) Type-II assembly, the nanoctahedra oriented along <110>, as indicated by the model.

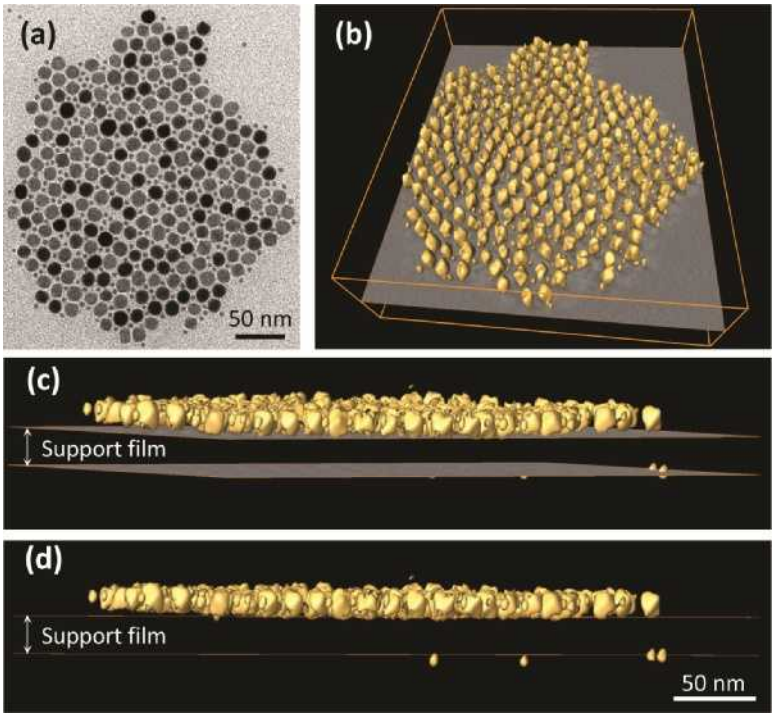

Fig. 9.33 3D reconstruction. (a) TEM image; (b) reconstructed volume rendering; (c) close to edge-on side view of the volume; (d) edge-on side view of the volume. Data bars represent a scale of 50 nm.

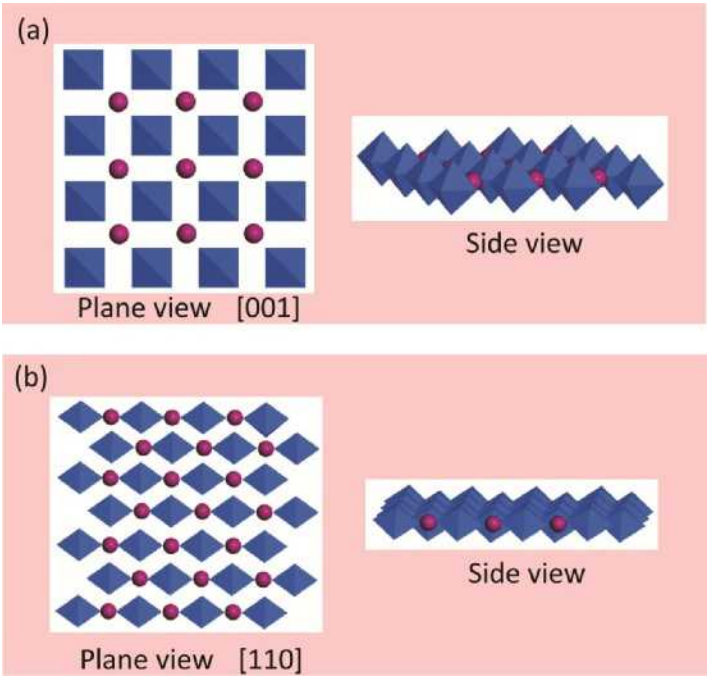

Fig. 9.34 Structure models of (a) Type I ([100] oriented) and (b) Type II ([110] oriented) 2D BNSL assemblies along plane and side views, respectively.

9.5.4 *Nanoparticle Superlattices*

Similar to atoms to form crystals, NPs can assemble into NP superlattices (NPSLs). To determine the crystal structures, diffraction and HRTEM imaging methods are used. Although it is possible to reach atomic resolution using ET [63], it is still difficult to reveal unknown crystalline structures using ET. Since the NPs in NPSLs are much larger than single atoms, it is possible to directly visualize the individual NPs within NPSLs to clarify the superlattice structures.

The NPSLs of Pt_3Ni octahedral NPs were studied by ET [70]. Fig. 9.35(a) displays a TEM image, where nanoctahedra marked with solid dots were lying on the bottom support film, and with open dots were in the top layer according to the ET analysis. A planar unit cell is outlined, with a = 15.7 nm along the vertical direction (projection direction), and the other direction is about $\sqrt{2}\,a$. Fig. 9.35(b) is a stacking model of the

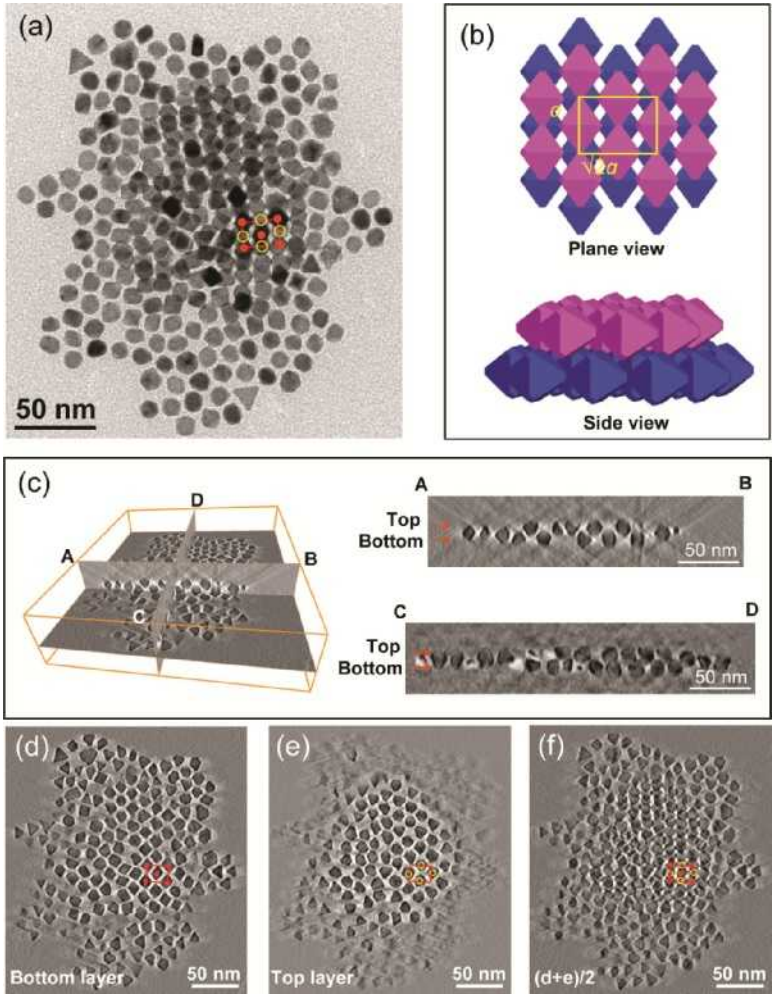

***Fig. 9.35** Double-layer stacking structure in a drop-cast superlattice studied using a tomography technique. (a) TEM image; (b) stacking model of double layers, along the plane and side views; (c) reconstructed volume, with two cross-sectional views, with top edges marked as AB and CD, respectively, shown on the right side. (d, e) Slice views of bottom and top layers, respectively, at the heights as marked in (c). Nanoctahedra marked with solid and open dots correspond to those in (a); (f) superimposition of (d) and (e), but the intensity is divided by 2.*

double-layer assembly, along the plane and side views. Fig. 9.35(c) illustrates the 3D reconstructed volume with three cross-sectional views, and two of them, with top edges marked as AB and CD, respectively, are

displayed on the right panel. It is evident that this is a double-layered structure, and the nanoctahedra of the top layer are located in the gap between nanoctahedra of the bottom layer that are the more stable positions to reduce the surface energy. Fig. 9.35(d) and (e) are the slices of bottom and top layers, respectively, at the heights as marked in Fig. 9.35(c). Nanoctahedra marked with solid and open dots correspond to those in Fig. 9.35(a). Fig. 9.35(f) is a superposition of Fig. 9.35(d) and (e), but the intensity was divided by 2. The superposition produces two lines of paired bright spots within a unit cell, confirming the bright image spots appearing in the TEM image in Fig. 9.35(a) are indeed the empty channels along the viewing direction. This can also be seen in the plane view model in Fig. 9.35(b).

In the stacking structure of a triple-layer pattern, Fig. 9.36(a) shows a TEM image with an inset of its SAED along [110]. Fig. 9.36(b) illustrates a structure model of the *bcc* packing unit cell, as well as plane and side views. The reconstructed volume is shown in Fig. 9.36(c), with two cross-sectional views AB and CD showing on the right side. From this analysis, three stacked layers are recognizable. Similar to the double-layer structure, the nanoctahedra of two neighboring layers are shifted by half of the repeat spacing. The nanoctahedra thus form a *bcc* packing superlattice (refer to Fig. 9.36b). Fig. 9.36(d), (e), and (f) show slices of the bottom, middle, and top layers, respectively, at the heights as indicated in Fig. 9.36(c). With the outlined planar unit cells, the nanoctahedra of the top and bottom layers have the same planar positions, whereas nanoctahedra in the middle layer are located in the maximum space between them. Fig. 9.36(g) is a superimposition of Fig. 9.36(d), (e), and (f), but the intensity was divided by 3. The resulting bright image dot lines are consistent with the observed TEM image in Fig. 9.36(a).

ET of a Pt_3Cu_2 NPSL with five layers was conducted [71]. Fig. 9.37(a) presents a TEM image of an area selected for tomography. Circled particles are identified to be located underneath the carbon support film according to this ET study. Fig. 9.37(b) presents a structural model of a *bcc* superlattice. The 3D reconstructed volume from large tilting angle series (from −62° to 64° at 1° interval) is shown in Fig. 9.37(c), and two orthogonal views AB and CD are shown in the right side. From the cross-sectional views, it is apparent that the assembly contained five stacked

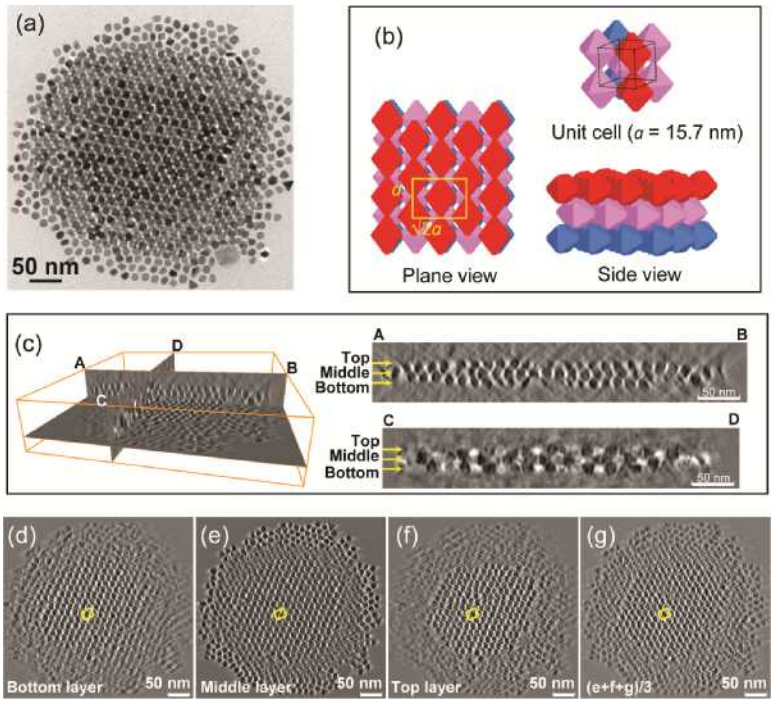

***Fig. 9.36** Triple-layer stacking structure in a drop-cast superlattice studied using a tomography technique. (a) TEM image; (b) structure models of the bcc packing unit cell, as well as plane and side views; (c) reconstructed volume, with two cross-sectional views, with top edges marked as AB and EF, respectively, shown on the right side. (d–f) Slice view of bottom, middle and top layers, respectively, at the heights as marked in (c). (g) Superimposition of (d), (e), and (f), but the intensity is divided by 3.*

layers, while without the reconstruction, it is almost impossible to identify the layers from the 2D image in Fig. 9.37(a), even when viewed at different tilting angles.

It is noticed that the bottom of this agglomerate is not flat but formed a downward depression of the support film, as marked by the broken lines, indicating an effect of gravity, or more likely the surface tension of the agglomerate that tends to favor a spherical shape. The support film is visible in the cross-sectional views, with a measured thickness of 16 nm. The particle indicated by an arrow under the film is the same one indicated by an arrow in the plane view in Fig. 9.37(a).

Note that along the z direction, particles are slightly stretched due to a tomography artifact.

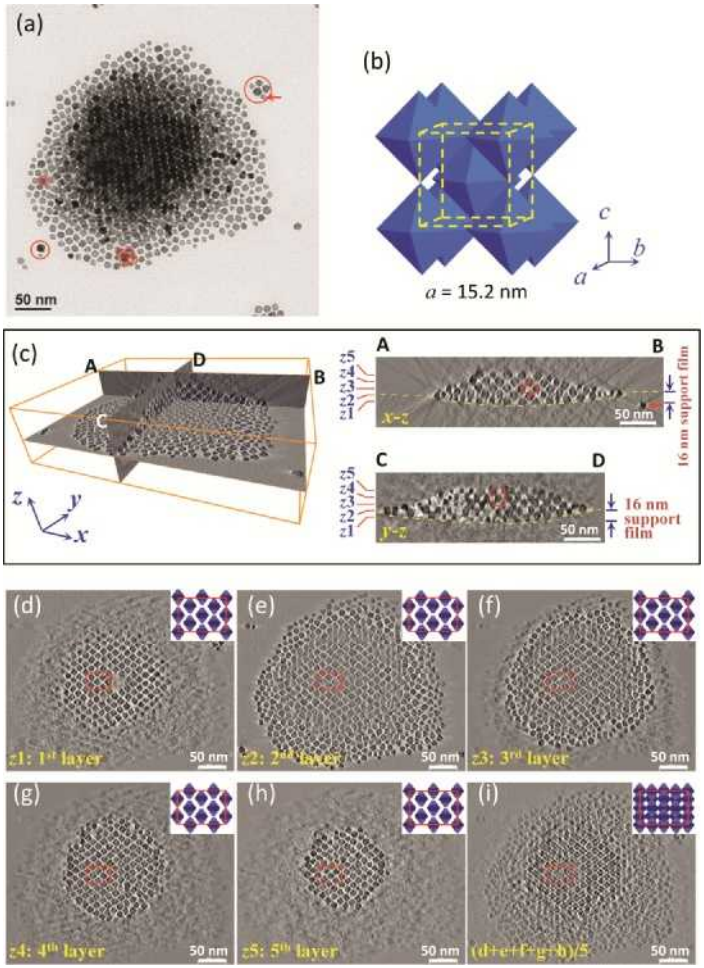

Fig. 9.37 Electron tomographic analysis of superlattice structure. (a) TEM image (circled particles are located underneath of the carbon support film); (b) superlattice model with bcc structure; (c) 3D reconstructed volume, with two orthogonal views labeled as AB and CD shown on the right side; (d–h) slice plane views at the heights of z1–z5 as indicated in (c); (i) averaged intensities of the images (d) through (h). Planar 2 × 2 unit cells are outlined in (d–h), with schematic structural models showing on the top-right corner of each image.

Slice plane views at the height of $z1$, $z2$, …, $z5$ as marked in Fig. 9.37(c) are shown in Fig. 9.37(d)–(h), indicating the nanoctahedra on the 1st to 5th layers, respectively. As summarized by a schematic model projection presented in the inset of each corresponding slice-view pattern, the NPs on the same layer formed a near regular, centered rectangular pattern, with 2×2 unit cell outlined, and two adjacent layers just offset by half the periodicity, suggesting a stacking sequence of ABAB .... By summation of Fig. 9.37(d) through Fig. 9.37(h) then followed a division by 5, an image with white dotted lines is obtained (Fig. 9.37i), which has the same image features as observed in the TEM image (Fig. 9.37a). Superimposing two adjacent model projections produced these observed image features with white dotted lines, which are the empty channels along the viewing direction. The averaged lattice parameter was measured as a = 15.2 nm.

Fig. 9.38 shows ET results of Pt nanocube (NCb) superlattices assembled from aromatic toluene [72]. The coexistence of monolayer and bilayer NCb assemblies in the selected area (Fig. 9.38a) demonstrates that NCbs in both regions prefer to contact each other via their (100) faces and to have square face-to-face conformation. In the magnified bilayer zone, the NCbs on the top layer take the same orientation as the bottom ones and have a face-to-face contact between both layers (Fig. 9.38b). The structure model of simple cubic (SC) structure is presented in Fig. 9.38(c). Fig. 9.38(d) illustrates the 3D reconstructed volume (left), and two orthogonal cross-sectional views AB and CD on the right. It is clear that within this double-layer assembly, the NCbs in the top layer ($z1$) from both slices are directly located on the top surface of bottom layer ($z2$). The corresponding slice views of the top and bottom layers, as marked with height labels ($z1$ and $z2$) in Fig. 9.38(d), are shown in Fig. 9.38(e) and (f), respectively. Their averaged intensity is shown in Fig. 9.38(g). From the lateral views of AB and CD shown in Fig. 9.38(d), the horizontal length is measured to be 12.2 nm, while the vertical height is 11.5 nm with an uncertainty of 5.7%. Considering the systematic error along the vertical direction produced in TEM tomography, it is reasonable to assume that this is a cubic structure. The measured lattice constant a = 12.2 nm and an average interparticle spacing is 2.23 nm.

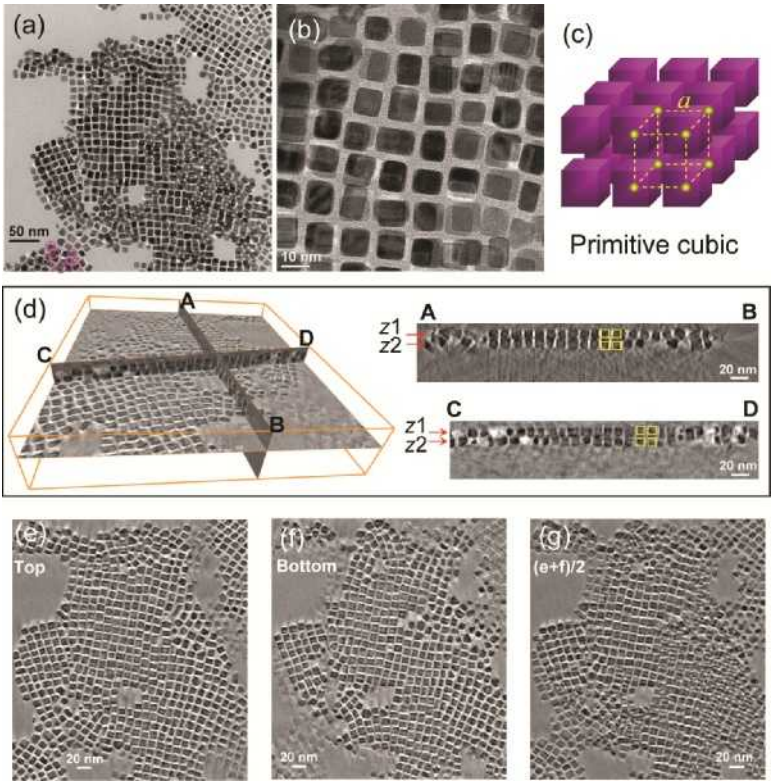

***Fig. 9.38** Self-assembly patterns of Pt NCbs generated from a toluene solvent. (a) TEM image; (b) magnified image from (a); (c) structural model; (d) 3D reconstruction (left) with two orthogonal views AB and CD (right); (e, f) slice views of the top and bottom layers at the heights of z1 and z2, respectively, as indicated in (d); (g) calculated image obtained by averaging (e) and (f).*

When the aromatic toluene solvent was replaced by aliphatic hexane while other conditions were kept the same, the TEM image of NCb assemblies is shown in Fig. 9.39(a), exhibiting a significant change in the packed superstructure. To clearly probe the assembly structure in the multilayer regions, the part marked with a square in Fig. 9.39(a) was magnified in Fig. 9.39(b), showing the projection of NCbs from several layers. The stacking model is illustrated in Fig. 9.39(c). The 3D reconstructed volume, together with two delicately chosen cross sections, is shown in Fig. 9.39(d). From these images, three different layers are easily recognized. The top and bottom layers locate vertically equivalent positions and

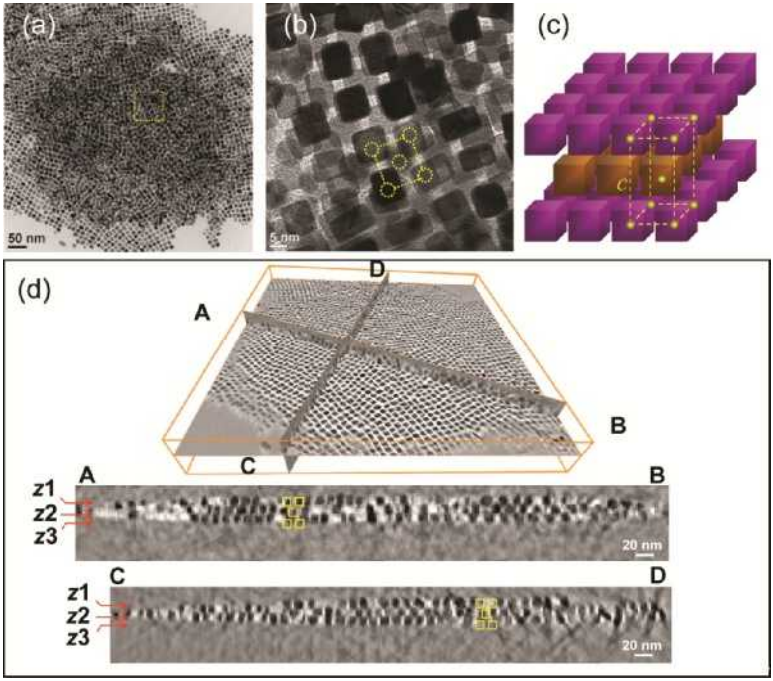

Fig. 9.39 TEM and tomographic results of Pt NCb self-assembly generated from hexane as the solvent. (a) TEM image; (b) magnified image; (c) structural model; (d) 3D reconstruction (left) with two orthogonal views AB and CD (right).

the middle one is horizontally shifted along a certain distance relative to them. It can be clearly seen that the average distance between the top and bottom layers is much larger than the interparticle distance within the same layer. Fig. 9.40(a)–(c) displays their reconstructed slice views at different heights labeled as $z1$, $z2$, and $z3$, respectively, as well as their relative in-plane coordinates (image insets). As is shown, the NCbs in the middle layer have different coordinates from those in the other two layers, which may be explained as a result of simultaneous in-plane movements along two horizontal directions with a half interparticle distance. The superimposed averaged image is shown in Fig. 9.40(e). The superlattice has a body-centered tetragonal (BCT) structure, with a = 12.5 nm and c = 20.0 nm. Although there is a systematic error associated with the vertical height measurement in TEM tomography, if we assume that the error along the vertical direction is the same as that indicated in Fig. 9.38 (within ±5.7%), the lattice parameter c will be in the range of 18.9–21.1 nm.

Based on a = 12.5 nm and c = 20.0 nm, the interparticle spacing within the horizontal layer is determined to be 2.59 nm, which is 16% larger than that for the SC superlattice (2.23 nm) in Fig. 9.38. ET directly revealed the superlattice structure type, lattice parameters, component NP shape, size, and their spacing.

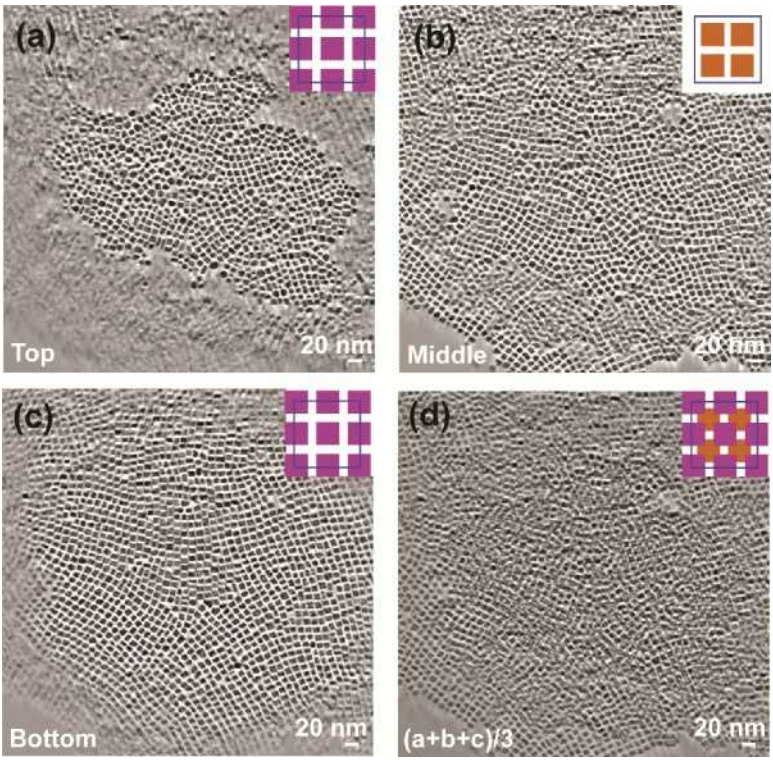

Fig. 9.40 (a–c) Slice views of the top, middle, and bottom layers at the heights of z1, z2, and z3, respectively, as indicated in Fig. 39(d); (d) image by averaging (a–c). Unit cells are outlined.

References

[1] F.H. Li. Crystallographic image processing approach to crystal structure determination. *J. Microsc.* **190**, 249–261 (1998).

[2] C.L. Jia, M. Lentzen, K. Urban. Atomic-resolution imaging of oxygen in perovskite ceramics. *Science* **299**, 870–873 (2003).

[3] X.D. Zou, S. Hovmöller. Structure determination from HREM by crystallographic image processing. In: *Electron Crystallography: Novel Approaches for Structure Determination of Nanosized Materials*, edited by T.E. Weirich, J.L. Lábár, X.D. Zou. Springer, Dordrecht, Netherlands, pp. 275–300 (2004).

[4] L. Houben, C.L. Jia, K. Tillmann, K. Urban. Quantitative aberration-corrected transmission electron microscopy. *Microsc. Microanal.* **10** (Suppl. 03), 38–40 (2004).

[5] J.M. LeBeau, S.D. Findlay, L.J. Allen, S. Stemmer. Quantitative atomic resolution scanning transmission electron microscopy. *Phys. Rev. Lett.* **100**, 206101 (2008).

[6] S.A. Nepijko, G. Schönhense. Quantitative Lorentz transmission electron microscopy of structured tin permalloy films. *Appl. Phys.* **A96**, 671–677 (2009).

[7] S. Shokri, M. Hemadi, R.J. Aitken. Transmission electron microscopy for the quantitative analysis of testis ultrastructure. In: *The Transmission Electron Microscope*, edited by K. Maaz, InTech, Rijeka, Croatia, pp. 113–126 (2012).

[8] J. Hwang, J.Y. Zhang, S. Stemmer. Progress in applications of quantitative STEM. *Microsc. Microanal.* **20** (Suppl 3), 58–59 (2014).

[9] Z.P. Luo. Statistical quantification of the microstructural homogeneity of size and orientation distributions. *J. Mater. Sci.* **45**, 3228–3241 (2010).

[10] M.D. Abramoff, P.J. Magelhaes, S.J. Ram. Image processing with ImageJ. *Biophoton. Int.* **11**, 36–42 (2004).

[11] Z.P. Luo, J.H. Koo. Quantitative study of the dispersion degree in carbon nanofiber/polymer and carbon nanotube/polymer nanocomposites. *Mater. Lett.* **62**, 3493–3496 (2008).

[12] Z.P. Luo, J.H. Koo. Quantification of the layer dispersion degree in polymer layered silicate nanocomposites by transmission electron microscopy. *Polymer* **49**, 1841–1852 (2008).

[13] Z.P. Luo, J.H. Koo. Quantifying the dispersion of mixture microstructures. *J. Microsc.* **225**, 118–125 (2007).

[14] X.D. Zou, Y. Sukharev, S. Hovmoller. ELD–a computer program system for extracting intensities from electron diffraction patterns. *Ultramicroscopy* **49**, 147–158 (1993).

[15] T.E. Weirich, M. Winterer, S. Seifried, H. Hahn, H. Fuess. Rietveld analysis of electron powder diffraction data from nanocrystalline anatase, TiO_2. *Ultramicroscopy* **81**, 263–270 (2000).

[16] J.L. Lábár. Electron diffraction based analysis of phase fractions and texture in nanocrystalline thin films, Part I: Principles. *Microsc. Microanal.* **14**, 287–295 (2008).

[17] J.L. Lábár. Electron diffraction based analysis of phase fractions and texture in nanocrystalline thin films, Part II: Implementation. *Microsc. Microanal.* **15**, 20–29 (2009).

[18] J.L. Lábár, M. Adamik, B.P. Barna, Zs. Czigány, Zs. Fogarassy, Z.E. Horváth, O. Geszti, F. Misják, J. Morgiel, G. Radnóczi, G. Sáfrán, L. Székely, T. Szüts. Electron diffraction based analysis of phase fractions and texture in nanocrystalline thin films, Part III: Application Examples. *Microsc. Microanal.* **18**, 406–420 (2012).

[19] X.Z. Li. PCED2.0—A computer program for the simulation of polycrystalline electron diffraction pattern. *Ultramicrosc.* **110**, 297–304 (2010).

[20] J.-G. Kim, J.-W. Seo, J. Cheon, Y.-J. Kim. Rietveld analysis of nano-crystalline $MnFe_2O_4$ with electron powder diffraction. *Bull. Korean Chem. Soc.* **30**, 183–187(2009).

[21] M. Gemmi, M. Voltolini, A.M. Ferretti, A. Ponti. Quantitative texture analysis from powder-like electron diffraction data. *J. Appl. Cryst.* **44**, 454–461 (2011).

[22] X.-Z. Li. QPCED2.0: A computer program for the processing and quantification of polycrystalline electron diffraction patterns. *J. Appl. Cryst.* **45**, 862–868 (2012).

[23] Z. Luo, Y. Vasquez, J.F. Bondi, R.E. Schaak. Pawley and Rietveld refinements using electron diffraction from $L1_2$-type intermetallic Au_3Fe_{1-x}nanocrystals during their *in-situ* order-disorder transition. *Ultramicroscopy* **111**, 1295-1304 (2011).

[24] G.S. Pawley. Unit-cell refinement from powder diffraction scans. *J. Appl. Crystallogr.* **14**, 357–361 (1981).

[25] H. M. Rietveld. A profile refinement method for nuclear and magnetic structures. *J. Appl. Crystallogr.* **2**, 65–71 (1969).

[26] S. Brückner. Estimation of the background in powder diffraction patterns through a robust smoothing procedure. *J. Appl. Crystallogr.* **33**, 977–979 (2000).

[27] Materials Studio Program Online Help, Version 6.0. Biovia, San Diego, CA.

[28] F. Banhart (Ed.). *In-situ Electron Microscopy at High Resolution*. World Scientific Publishing Co., Singapore, 2008.

[29] F.M. Ross. *In-situ* TEM studies of vapor- and liquid-phase crystal growth. In: *In-situ Electron Microscopy: Applications in Physics, Chemistry and Materials Science,* edited by G. Dehm, J.M. Howe, J. Zweck. Wiley-VCH, Weinheim, pp. 171–190 (2012).

[30] G. Zhou, J.C. Yang. *In-situ* TEM studies of oxidation. In: *In-situ Electron Microscopy: Applications in Physics, Chemistry and Materials Science*, edited by G. Dehm, J.M. Howe, J. Zweck. Wiley-VCH, Weinheim, pp. 191–208 (2012).

[31] T. Sumigawa, T. Kitamura. *In-situ* mechanical testing of nanocomponent in TEM. In: *The Transmission Electron Microscope*, edited by K. Maaz, InTech, Rijeka, Croatia, pp. 354–380 (2012).

[32] X.F. Zhang. In-situ transmission electron microscopy. In: *In-situ Materials Characterization: Across Spatial and Temporal Scales*, edited by A. Ziegler, H. Graafsma, X.F. Zhang, J.W.M. Frenken. Springer, Heidelberg, pp. 59–110 (2014).

[33] Z. Luo, A. Oki, L. Carson, L. Adams, G. Neelgund, N. Soboyejo, G. Regisford, M. Stewart, K. Hibbert, G. Beharie, C. Kelly-Brown, P. Traisawatwong. Thermal stability of functionalized carbon nanotubes studied by *in situ* transmission electron microscopy. *Chem. Phys. Lett.* **513**, 88–93 (2011).

[34] H. Zheng, Z. Luo, D. Fang, Francis R. Phillips, D.C. Lagoudas. Reversible phase transformations in a shape memory alloy In-Tl nanowires observed by *in situ* transmission electron microscopy. *Mater. Lett.* **70**, 109–112 (2012).

[35] Z.P. Luo, D.J. Miller, J.F. Mitchell. Structure and charge ordering behavior of the colossal magnetoresistive manganite $Nd_{0.5}Sr_{0.5}MnO_3$. *J. Appl. Phys.* **105**, 07D528 (2009).

[36] Z.P. Luo, D.J. Miller, J.F. Mitchell. Electron microscopic evidence of charge-ordered bi-strip structures in the bilayered colossal magnetoresistive manganite $La_{2-2x}Sr_{1+2x}Mn_2O_7$. *Phys. Rev.* **B71**, 014418 (2005).

[37] J.F. Mitchell, D.D. Ling, J.E. Millburn, D.N. Argyriou, A. Gerger, M. Medarde, D. Miller, Z.P. Luo. Heavily doped bilayer manganites: links among structure, charge and spin. *Appl. Phys. A: Mater. Sci. Process*. **74**, S1776–S1778 (2002).

[38] C.W. Allen, E.A. Ryan. In situ transmission electron microscopy employed for studies of effects of ion and electron irradiation on materials. *Microsc. Res. Tech.* **42**, 255–259 (1998).

[39] R.C. Birtcher, M.A. Kirk, K. Furuya, G.R. Lumpkin, M.-O. Ruault. In situ transmission electron microscopy investigation of radiation effects. *J. Mater. Res.* **20**, 1654–1683 (2005).

[40] J. Lian, L.M. Wang, K. Sun, R.C. Ewing. In situ TEM of radiation effects in complex ceramics. *Microsc. Res. Tech.* **72**, 165–181 (2009).

[41] M.A. Kirk, P.M. Baldo, A.C.Y. Liu, E.A. Ryan, R.C. Birtcher, Z. Yao, S. Xu, M.L. Jenkins, M. Hernandez-Mayoral, D. Kaoumi, A.T. Motta. In situ transmission electron microscopy and ion irradiation of ferritic materials. *Microsc. Res. Tech.* 72,182–186 (2009).

[42] K. Hattar, D.C. Bufford, D.L. Buller. Concurrent in situ ion irradiation transmission electron microscope. *Nucl. Instrum. Meth. Phys. Res.* **B338**, 56–65 (2014).

[43] El-Atwani, J. A. Hinks, G. Greaves, S. Gonderman, T. Qiu, M. Efe, J.P. Allain. In-situ TEM observation of the response of ultrafine- and nanocrystalline-grained tungsten to extreme irradiation environments. *Sci. Reports* **4**, 4716 (2014).

[44] Y. Chen, K.Y. Yu, Y. Liu, S. Shao, H. Wang, M.A. Kirk, J. Wang, X. Zhang. Damage-tolerant nanotwinned metals with nanovoids under radiation environments. *Nature Commun.* **6**, 7036 (2015).

[45] Z. Quan, Z. Luo, Y. Wang, H. Xu, C. Wang, Z. Wang, J. Fang. Pressure-induced switching between amorphization and crystallization in PbTe nanoparticles. *Nano Lett.* **13**, 3729–3735 (2013).

[46] M. Almgren, K. Edwards, Göran Karlsson. Cryo transmission electron microscopy of liposomes and related structures. *Colloids Surfaces* **A174**, 3–21 (2000).

[47] J.E. Evans, C. Hetherington, A. Kirkland, L.-Y. Chang, H. Stahlberg, N. Browning. Low-dose aberration corrected cryo-electron microscopy of organic specimens. *Ultramicroscopy* **108**, 1636–1644 (2008).

[48] R.A Grassucci, D. Taylor, and J. Frank. Visualization of macromolecular complexes using cryo-electron microscopy with FEI Tecnai transmission electron microscopes. *Nature Protoc.* **3**, 330–339 (2008).

[49] J. Kuntsche, J.C. Horst, H. Bunjes. Cryogenic transmission electron microscopy (cryo-TEM) for studying the morphology of colloidal drug delivery systems. *Inter. J. Pharm.* **417**, 120–137 (2011).

[50] J.L.S. Milne, M.J. Borgnia, A. Bartesaghi, E.E.H. Tran, L.A. Earl, D.M. Schauder, J. Lengyel, J. Pierson, A. Patwardhan, S. Subramaniam. Cryo-electron microscopy – a primer for the non-microscopist. *FEBS J.* **280**, 28–45 (2013).

[51] H. Huang, A.I. Herrera, Z. Luo, O. Prakash, X.S. Sun. Structural transformation and physical properties of a hydrogel-forming peptide studied by NMR, transmission electron microscopy, and dynamic rheometer. *Biophys. J.* **103**, 979–988 (2012).

[52] K.A. Morales, M. Lasagna, A.V. Gribenko, Y. Yoon, G.D. Reinhart, J.C. Lee, W. Cho, P. Li, T.I. Igumenova. Pb^{2+} as modulator of protein–membrane interactions. *J. Am. Chem. Soc.* **133**, 10599–10611 (2011).

[53] Y. Fujiyoshi, T. Kobayashi, K. Ishizuka, N. Uyeda, Y. Ishida, Y. Harada. A new method for optimal-resolution electron microscopy of radiation-sensitive specimens. *Ultramicroscopy* **5**, 459–468 (1980).

[54] G.Rh. Owen, D.L. Stokes. An introduction to low dose electron tomography- from specimen preparation to data collection. In: *Modern Research and Educational Topics in Microscopy*, edited by A. Méndez-Vilas, J. Díaz, Formatex, Badajoz, Spain, pp. 939–950 (2007).

[55] D.B. Carlson, J.E. Evans. Low-dose imaging techniques for transmission electron microscopy. In: *The Transmission Electron Microscope*, edited by K. Maaz, InTech, Rijeka, Croatia, pp. 354–380 (2012).

[56] M. Gao, Y.-K. Kim, C. Zhang, V. Borshch, S. Zhou, H.-S. Park, A. Jákli, O.D. Lavrentovich, M.-G. Tamba, A. Kohlmeier, G.H. Mehl, W. Weissflog, D. Studer, B. Zuber, H. Gnägi, F. Lin. Direct observation of liquid crystals using Cryo-TEM: Specimen preparation and low-dose imaging. *Microsc. Res. Tech.* **77**, 754–772 (2014).

[57] M. Weyland, P.A. Midgley. Electron tomography. *Mater. Today* **7**, 32–40 (2004).

[58] J. Frank (Ed.). *Electron Tomography: Methods for Three-Dimensional Visualization of Structures in the Cell*. Second Edition. Springer, New York, 2006.

[59] G. Möbus, B.J. Inkson. Nanoscale tomography in materials science. *Mater. Today* **10**, 18–25 (2007).

[60] P.A. Midgley and R.E. Dunin-Borkowski. Electron tomography and holography in materials science. *Nature Mater.* **8**, 271–280 (2009).

[61] R. Leary, P.A. Midgley, J.M. Thomas. Recent advances in the application of electron tomography to materials chemistry. *Acc. Chem. Res.* **45**, 1782–1791 (2012).

[62] P.A. Midgley, S. Bals. Electron tomography. In: *Handbook of Nanoscopy*, Vol. 1, edited by G. Van Tendeloo, D. Van Dyck, S.J. Pennycook. Wiley-VCH, Weinheim, Germany. pp. 253–279 (2012).

[63] M.C. Scott, C.-C. Chen, M. Mecklenburg, C. Zhu, R. Xu, P. Ercius, U. Dahmen, B.C. Regan, J. Miao. Electron tomography at 2.4-ångström resolution. *Nature* **483**, 444–448 (2012).

[64] M.H. Li, Y.Q. Yang, B. Huang, X. Luo, W. Zhang, M. Han, J.G. Ru. Development of advanced electron tomography in materials science based on TEM and STEM. *Trans. Nonferrous Met. Soc. China* **24**, 3031–3050 (2014).

[65] P. Ercius, O. Alaidi, M.J. Rames, G. Ren. Electron tomography: A three-dimensional analytic tool for hard and soft materials research. *Adv. Mater.* **27**, 5638–5663 (2015).

[66] Q. Liu, A. Diaz, A.V. Prosvirin, Z. Luo and J.D. Batteas. Shape-controlled synthesis of nanopyramids and nano-prisms of nickel sulfide (Ni_3S_4). *Nanoscale* **6**, 8935–8942 (2014).

[67] S.E. Wark, C.-H. Hsia, Z. Luo, D.H. Son. Surfactant effect on the formation of $CuInSe_2$ nanowires in solution phase synthesis. *J. Mater. Chem.* **21**, 11618–11625 (2011).

[68] Chen, Z. Luo, M. Akbulut. Ionic liquid mediated auto-templating assembly of $CaCO_3$-chitosan hybrid nanoboxes and nanoframes. *Chem. Commun.* **47**, 2312–2314 (2011).

[69] Z. Sun, Z. Luo, J. Fang. Assembling nonspherical 2D binary nanoparticle superlattices by opposite electrical charges: The role of Coulomb forces. *ACS Nano* **4**, 1821–1828 (2010).

[70] J. Zhang, Z. Luo, Z. Quan, Y. Wang, A. Kumbhar, D.-M. Smilgies, J. Fang. Low packing density self-assembled superstructure of octahedral Pt_3Ni nanocrystals. *Nano Lett.* **11** (7), 2912–2918 (2011).

[71] J. Zhang, Z. Luo, B. Martens, Z. Quan, A. Kumbhar, N. Porter, Y. Wang, D.-M. Smilgies, J. Fang. Reversible Kirkwood–Alder transition observed in Pt_3Cu_2 nanoctahedron assemblies under controlled solvent annealing/drying conditions. *J. Am. Chem. Soc.* **134**, 14043–14049 (2012).

[72] Z. Quan, H. Xu, C. Wang, X. Wen, Y. Wang, J. Zhu, R. Li, C.J. Sheehan, Z. Wang, D.-M. Smilgies, Z. Luo, and J. Fang. Solvent-mediated self-assembly of nanocube superlattices. *J. Am. Chem. Soc.* **136**, 1352–1359 (2014).

Illustration Credits

All the illustrations of this book have been prepared by the author with the following exceptions or reprints from the previously publications:

Figs. 6.13–6.16, Fig. 8.12, Fig. 8.24, Fig. 8.25, Fig. 9.18, Fig. 9.25, Fig. 9.26, Figs. 9.32–9.40—American Chemical Society

Fig. 7.18, Fig. 8.11, Fig. 8.14, Fig. 8.21, Figs. 9.6–9.10, Figs. 9.12–9.16, Fig. 9.22(a) and (b)—Elsevier

Fig. 6.7—JEOL Ltd

Fig. 7.4, Fig. 7.5, Fig. 9.1(a) and (b), Fig. 9.5—John Wiley and Sons

Fig. 8.3(d)—Oxford Instruments

Fig. 8.22, Fig. 8.23, Figs. 9.27–9.31—Royal Society of Chemistry

Fig. 8.13, Fig. 9.1(c), Figs. 9.2–9.4, Fig. 9.17—Springer

Fig. 7.14—Taylor & Francis

Index

OTHER TITLES IN OUR MATERIALS CHARACTERIZATION AND ANALYSIS COLLECTION

C. Richard Brundle, *Editor*

- *Secondary Ion Mass Spectrometry: Applications for Depth Profiling and Surface Characterization* by Fred Stevie
- *Auger Electron Spectroscopy: Practical Application to Materials Analysis and Characterization of Surfaces, Interfaces, and Thin Films* by John Wolstenholme
- *Spectroscopic Ellipsometry: Practical Application to Thin Film Characterization* by Harland G. Tompkins and James N. Hilfiker
- *A Practical Guide to Transmission Electron Microscopy, Volume I: Fundamentals* by Zhiping Luo

Momentum Press is one of the leading book publishers in the field of engineering, mathematics, health, and applied sciences. Momentum Press offers over 30 collections, including Aerospace, Biomedical, Civil, Environmental, Nanomaterials, Geotechnical, and many others.

Momentum Press is actively seeking collection editors as well as authors. For more information about becoming an MP author or collection editor, please visit http://www.momentumpress.net/contact

A Practical Guide to Transmission Electron Microscopy, Volume II

Advanced Microscopy

Zhiping Luo

Transmission electron microscope (TEM) is a very powerful tool for characterizing various types of materials. Using a light microscope, the imaging resolution is at several hundred nanometers, and for a scanning electron microscope at several nanometers. The imaging resolution of the TEM, however, can routinely reach several angstroms on a modem instrument. In addition, the TEM can also provide material structural information, since the electrons penetrate through the thin specimens, and chemical compositional information due to the strong electron specimen atom interactions.

This book provides a concise practical guide to the TEM user, starting from the beginner level, including upper-division undergraduates, graduates, researchers, and engineers, on how to learn TEM efficiently in a short period of time. Volume I covers the instrumentation, sample preparation, fundamental diffraction and imaging; and this volume covers advanced diffraction, imaging, analytical microscopy, and some newly developed microscopy techniques. This book may serve as a textbook for a TEM course or workshop, or a reference book for the TEM user to improve their TEM skills.

Dr. Zhiping Luo is an associate professor in the department of chemistry and physics at Fayetteville State University, North Carolina. He started electron microscopy in early 1990s. While he was conducting his PhD thesis work on rare earths-containing magnesium alloys, he encountered with fine complex intermetallic phases, so he used TEM as a major research method. From 1996 to 1997 he was at Okayama University of Science, Japan as a postdoctoral researcher to study electron microscopy with Professor H. Hashimoto. In 1998, he moved to materials science division, Argonne National Laboratory, as a visiting scholar and became the assistant scientist in 2001. Between 2001 and 2012, he worked as a TEM instrumental scientist at the Microscopy and Imaging Center at Texas A&M University, where he taught TEM courses and trained many TEM users. Dr. Luo has authored over 200 articles in peer-reviewed journals, and most of them involved TEM investigations.

MOMENTUM PRESS
ENGINEERING

ISBN 978-1-60650-917-3
90000
9 781606 509173